Study of JLC Hadron Calorimeter

Takashi SUZUKI

University of Tsukuba

Submited in Partial Fulfillment of the Requirements for the Degree of Master of Science in Program in Physics the University of Tsukuba

January, 1998

Abstract

Japan Linear Collider (JLC) is one of the major future accelerators proposed by high energy physicists. The main purpose for JLC are to search for the Higgs boson and the phenomena beyond the Standard Model. The calorimeter for the JLC detector is lead/plastic scintillator sampling calorimeter. It is required to a good energy resolution not only for EM particles, that is electrons and photons, ($\sigma/\mathrm{E} = 15\%\sqrt{\mathrm{E}} \oplus 1\%$) but also for hadrons ($\sigma/\mathrm{E} = 40\%\sqrt{\mathrm{E}} \oplus 2\%$).

To improve the energy resolution for hadrons, compensated calorimeter which has an equal response to EM particles and hadrons is needed. Compensation ratio e/h and e/π are calculated as a function of the volume ratio between the absorber and active volume. These were measured in some experiments at a fixed volume ratio, but have never been measured as a function of the volume ratio.

In order to measure the compensation ratio as a function of the volume ratio in the lead/plastic scintillator sampling calorimeter, we constructed the calorimeter prototype where the lead absorber thickness is changeable by employing a "hanging-file" configuration with a fixed scintillator thickness is 2 mm, and performed the beam tests of the calorimeter prototype at the $\pi 2$ beam line of KEK-PS.

To achieve the required energy resolution for the JLC calorimeter, Pb thickness should be less than 4 mm for the EM calorimeter and 8 mm for hadron calorimeter.

The e/π ratio decreases with the absorber thickness d and is one around $d = 8\sim10$ mm. The compensation was found to be achieved with the ratio of the scintillator thickness to the Pb thickness of $4\sim5$ as expected.

Acknowledgments

I would like to thank Prof. S. Kim, Prof. K. Kondo, and Prof. K. Takikawa for their many helpful advices, suggestions, and encouragement. I wish to thank Drs. K. Hara, Drs. Y. Seiya, Drs. R. Oishi, and Drs. T. Asakawa for their comments and advices. I wish to thank all the members of high energy physics laboratry of Univ. of Tsukuba, too.

I would like to thank all the members of the JLC calorimeter Group. I am especially grateful to the beam test members for performing our experiment together, and construction and measurement of the tile/fiber systems. Among them, I am especially grateful to Y. Fujii, N. Kanaya, and T. Toeda for their fruitful comments, advices, and discussion on the results of the beam tests.

Contents

List of Tables

List of Figures

collaborators

I. Daigo[a], Y. Fujii[b], K. Hara[a], T. Ishizaki[a], F. Kajino[d],

N. Kanaya[c], J. Kanzaki[b], K. Kawagoe[c], S. Kim[a], T. Matsui[b],

A. Miyajima[e], A. Nakagawa[a], S. Nakazawa[c], T. Ota[a], K. Sendai[b],

K. Sugimoto[c], Y. Sugimoto[b], T. Suzuki[a], H. Takayama[a], T. Takeshita[e],

S. Tanaka[c], A. Tanaka[d], T. Toeda[e], Y. Yamada[d]

a : Univ. of Tsukuba

b : KEK

c : Kobe Univ.

d : Konan Univ.

e : Shinshu Univ.

Chapter 1

Introduction

1.1 The plan of JLC

Particle physicists have established the Standard Model and have been searching a new theory including the Standard Model. Linear-Collider (LC) projects are recommended as future experiment plans by high energy physicists around the world in order to study the nature deeply and precisely. Japan-Linear-Collider (JLC) [1] is one of the LC projects in Japan, aiming at observation of the Higgs boson and the phenomena beyond the Standard Model.

The JLC project consists of the construction of an e^+e^- linear collider, and the experiments therewith, at an initial center of mass energy around 500 GeV which will eventually reach 1.5 TeV. The JLC project will proceed along the plan of phase-I machine (JLC-I) that it cover a center of mass energy range of up to 500 GeV with a peak luminosity of 5×10^{33} cm^{-2}sec^{-1}. A schematic view of the JLC accelerator is shown in Fig. 1.1. Linear collider is about 28 km long. It consists of 5 parts, electron and positron sources, a dumping ring, a main linac, a final focus system and a collision hall.

1.2 JLC detector

Total cross sections in $e^+e^- \to$ X collisions as a function of the center of mass energy are shown in Fig. 1.2. For capability of operating under new background environments and of the unambiguous identification of new physics that we shall encounter, the detector of JLC has to be a general purpose detector with precise tracking in a solenoidal magnetic field, hermetic calorimetry, and high resolution vertex detection. We have to design our detector so as to exclusively reconstruct all final-state particles except for neutrinos.

Reconstruction of the W and Z bosons via jets is very important because of using their large decay branching fractions into quarks. To improve the mass resolution of the W and Z bosons, we not only rely on the tracking information for charged particles, but also use the calorimeter information for neutral particles, which are only detectable by a calorimeter. In this scheme, a good track-energy cluster matching is essential to determine event topologies correctly. It is also very important to tag b-quarks by detecting decaying points in order to identify the top quark and Higgs production.

One of the most important physics targets of JLC, especpecally in phase-I, is to study the Higgs boson. For this purpose, the detector should be capable of confirming the narrow decay width of the new particle. In searches of SUSY particles, detection of missing P_t is also important, and requires a good angular coverage. Taking these requirements into account, we set criteria for the JLC detector :

- hermetic calorimetry in polar angle region $|\cos\theta| < 0.98$ (the rest is occupied by the final focus system),
- jet invariant mass resolution comparable with the natural width of W and Z,
- lepton pair recoil mass resolution for $e^+e^- \to ZH_{SM}$ comparable with the beam energy spread (200 MeV).

The parameters and the performance of each detector component are summarized in Tables 1.1, 1.2, 1.3, and 1.4. All the tracking devices and the calorimeter are placed inside the 2-Tesla superconducting solenoid to achieve a good hermeticity. Shown in Fig. 1.3 is the JLC detector.

1.2.1 Vertex detector (VTX)

The parameters and performance of the vertex detector are listed in Table 1.1. The vertex detector consists of at least 3 layers of Si-CCD arrays that can accommodate background tracks and γ's via e^+e^- pairs created by beamstrahlung photons. The layers are placed at $r = 2.5$, 5.0, 7.5 cm, respectively. The expected impact parameter resolution of a track is 30 μm (at $\theta = 90^o$, $p = 1$ GeV/c).

Detector	Vertex detector (VTX)
Type	Silicon CCD
configuration	pixel size : 25 μm # of layers : at least 3 layers layer position : r = 2.5, 5.0, 7.5 cm Thickness : 500 μm/layer coverage : $\lvert\cos\theta\rvert < 0.95$
performance	position resolution : $\sigma = 7.2$ μm Impact Parameter Resolution : $\delta = \sqrt{11.4^2 + (28.8/p)^2/\sin^3\theta}$ μm

Table 1.1: Parameters and performance of vertex detector (VTX)

1.2.2 Central Drift Chamber (CDC)

The parameters and performance of the central drift chamber are listed in Table 1.2. The central tracking detector is a small-cell jet chamber. The inner and outer radii are 30 cm and 230 cm, respectively. The spatial resolution is 100 μm. we require two-track separation capability of 1 mm to use maximally the charged track information. The resolution in the z-coordinate is designed to be less than 2 mm to achieve a good track-cluster matching in front of the calorimeter.

1.2.3 Calorimeter (CAL)

The parameters and performance of the calorimeter are listed in Table 1.3. It is a lead-scintillator sandwich type calorimeter that has an equal response to electromagnetic and hadronic showers. The calorimeter is longitudinally segmented into three sections: the fine sampling electromagnetic shower section of 29 X_0 thickness (ECAL), Si-pads to

Detector	Central Drift Chamber (CDC)
Type	Small-cell Jet Chamber
configuration	Radius : r= 0.3 - 2.3 m Length : l = 4.6 m # of sampling : 100 coverage : $\lvert\cos\theta\rvert < 0.70$ (full sampling) $\lvert\cos\theta\rvert < 0.95$ (20 samplings)
performance	position resolution : $\sigma_X = 100\ \mu$m (/ axial wire) $\sigma_Z = 2$ mm (/ stereo wire) momentum resolution : $\sigma_{P_t} = 1.1 \times 10^{-4} P_t \oplus 0.1\%$ $\sigma_{P_t} = 5 \times 10^{-5} P_t \oplus 0.1\%$ (with vertex constraint)

Table 1.2: Parameters and performance of Central Drift Chamber (CDC)

detect electromagnetic pre-showers located after the first 4.3 X_0 of ECAL, and a hadron section of 5.6 interaction lengths (HCAL). The barrel and the endcap calorimeters consist of 2500 and 1250 tower modules, each pointing to the interaction region. These are discussed in next section and Chapter 2.

1.2.4 Muon detector (Muon)

The parameters and performance of the muon detector are listed in Table 1.4. The muon detector consists of six super-layers of single drift chambers. Since it only provides muon identification, a modest spatial resolution of 500 μm is required. The threshold momentum for muon identification is 3.5 GeV/c due to the large energy loss in the calorimeter.

Detector	Calorimeter (CAL)
Type	Lead + plastic scintillator sandwich
configuration	EM part : thickness 29 X_0 cell size 10 cm $\times$ 10 cm Hadron part : thickness 5.6 λ_I cell size 20 cm $\times$ 20 cm Si-Pad cell size : 1 cm $\times$ 1 cm coverage : $\lvert\cos\theta\rvert < 0.99$
performance	energy resolution : $\sigma_E/E = 15\% /\sqrt{E} \oplus 1\%$ (for e & γ) $\sigma_E/E = 40\% /\sqrt{E} \oplus 2\%$ (for hadron) Si-Pad position resolution : $\sigma = 3$ mm Si-Pad e-π rejection: 1/50

Table 1.3: Parameters and performance of calorimeter (CAL)

Detector	Muon detector (Muon)
Type	Single cell Drift chamber
configuration	# of superlayers : 6 coverage : $\lvert\cos\theta\rvert < 0.99$
performance	position resolution : $\sigma = 500\ \mu$m $P_t > 3.5$ GeV/c (barrel)

Table 1.4: Parameters and performance of muon detector (Muon)

1.3 JLC hadron calorimeter

1.3.1 Design Criteria

Precise study of the mass and the width of the Higgs boson, if it exists, is one of the most important physics targets of JLC. Such a Higgs boson should be produced by Z^0 associated processes at JLC energies (Feynman diagram of this process is shown in Fig. 1.4), so identification of Z^0 boson is important. Identifications through its decay into electrons or muons are clear, because of the accurate measurements of its mass using the informations with CDC, CAL, and MUON. A sum of the branching fractions of these decay modes is only 7%. Other decay modes of the Z^0 boson have lager branching fractions: quark pair decay modes have about 70% and neutorino pair decay modes have about 20%. If we can use these modes, we can collect the Higgs boson events of 10 times higher statistics.

Identification of $e^+e^- \rightarrow$ HZ events through Z^0 hadronic decay channels requires the capability of the identification of the Z^0 boson using a reconstructed 2-jet invariant mass. The most significant background for the hadronic detection of the intermideate mass of Higgs boson comes from the Z^0Z^0 production process, resulting in four hadronic jet or two hadronic jet final states. Especially a good jet-invariant mass resolution is required in order to separete reconstructed higgs bosons from background Z^0 bosons in the mass region of the Higgs. The study of couplings of W, Z^0, and γ requires the capability of the identification of the W and Z^0 boson using a reconstructed 2-jet invariant mass. In order to achieve these, the JLC detector is required to have a good 2-jet invariant mass resolution to separate W's and Z^0's through 2-jet invariant masses for the JLC calorimeter [1]. To achieve such a good 2-jet invariant mass resolution requires that a calorimeter must have a good energy resolution for hadrons.

1.3.2 Performance and Detector Configuration

The following resolution of the calorimeter is required to achieve the separation between the W and Z^0 bosons [1], [16]:

- Energy resolution : (stochastic and constant terms)

  $(\leq 15\%)\ /\ \sqrt{E} \oplus (\leq 1\%)$ for EM particles

  $(\leq 40\%)\ /\ \sqrt{E} \oplus (\leq 2\%)$ for hadrons

The results of some experiments [4], [6] and calculation [2] indicate that a calorimeter which consists of lead (absorber) and plastic scintillator (active volume) with optimized sampling fraction (about 4:1) can have a good resolution for hadrons (see next section and Chapter 2).

To observe the Higgs boson through the Z^0 decay into neutorinos channels, a good hermeticity is needed for accurate measurement of the missing momentum. For a good hermeticity, the calorimeter is placed inside the solenoidal coil.

The following configuration of the JLC calorimeter is proposed [1], [16], [17], [18], [19]:

- EM : (Pb 4 mm + scintillating tile 1 mm) $\times$ 40 layers, corresponding to 29 radiation lengths (X_0)

- HADRON : (Pb 8 mm + scintillating tile 2 mm) $\times$ 120 layers, corresponding to 5.6 interaction lengths (λ_I).

The parameters and performance of the calorimeter is also summarized in Table 1.3.

1.4 Beam test of hadron calorimeter

To acheive a good hadron energy resolution, we consider a compensated calorimeter (it is discussed in next chapter). In general, the pulse height of the calorimeter is usually different between electromagnetic (EM) shower and hadron shower. Compensation ratio (e/h ratio) is defined by

$$\mathrm{e/h} \equiv \frac{\text{pulse height for EM shower}}{\text{pulse height for hadron shower}}. \tag{1.1}$$

To compensated calorimeter

$$\mathrm{e/h} \simeq 1.$$

The e/h ratio is a function of volume ratio of the absorber and the active material [2]. Some experiments [4], [6], [7], [5] measured the e/h ratio at a fixed volume ratio, but it has never been measured as a function of the volume ratio. We performed the beam test to measure the dependence of e/h ratio, resolution, and the other characteristics of lead plastic scintillator calorimeter on the volume ratio.

We made the calorimeter prototype for the beam test. In Chapter 3, we discribe the characteristics of plastic scintillator tile/fiber system for the calorimeter prototype studied in our test bench.

In Chapter 4, we evaluate the performance of the calorimeter prototype consisting of the tile/fiber system measured in out test bench using a GEANT shower simulation.

Finally, we show the characteristics of lead plastic scintillator calorimeter measured with the beam test at KEK $\pi 2$ beam line in Chapter 5.

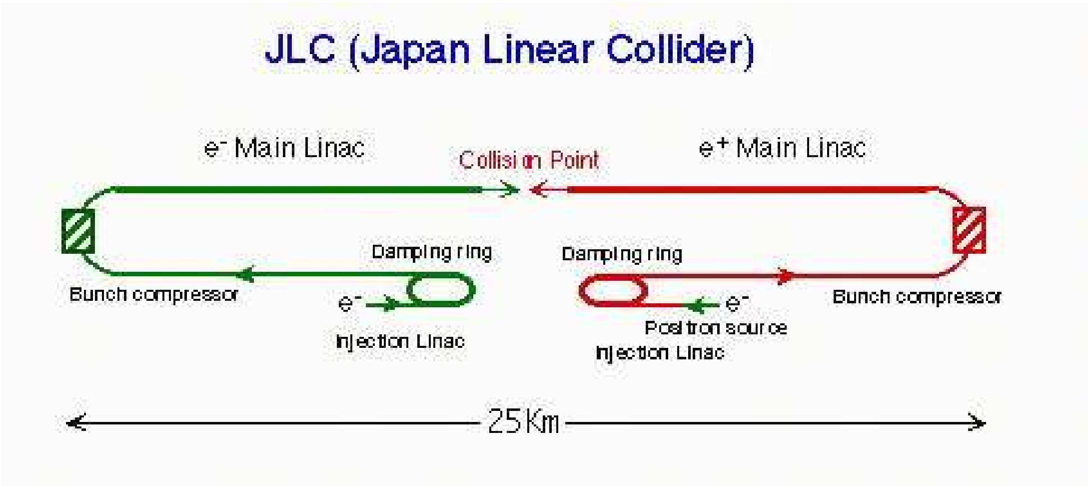

Figure 1.1: A schemetic view of the JLC accelerator

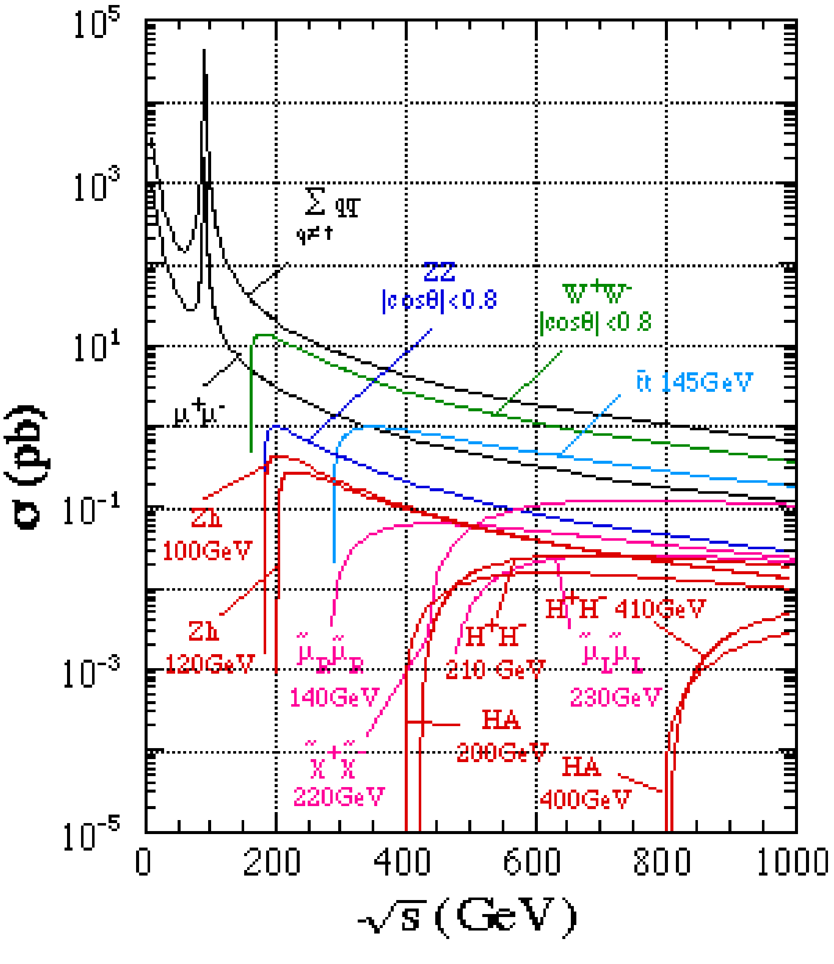

Figure 1.2: The total cross sections for reactions, $e^+e^- \to$ X, as a function of the center of mass energy.

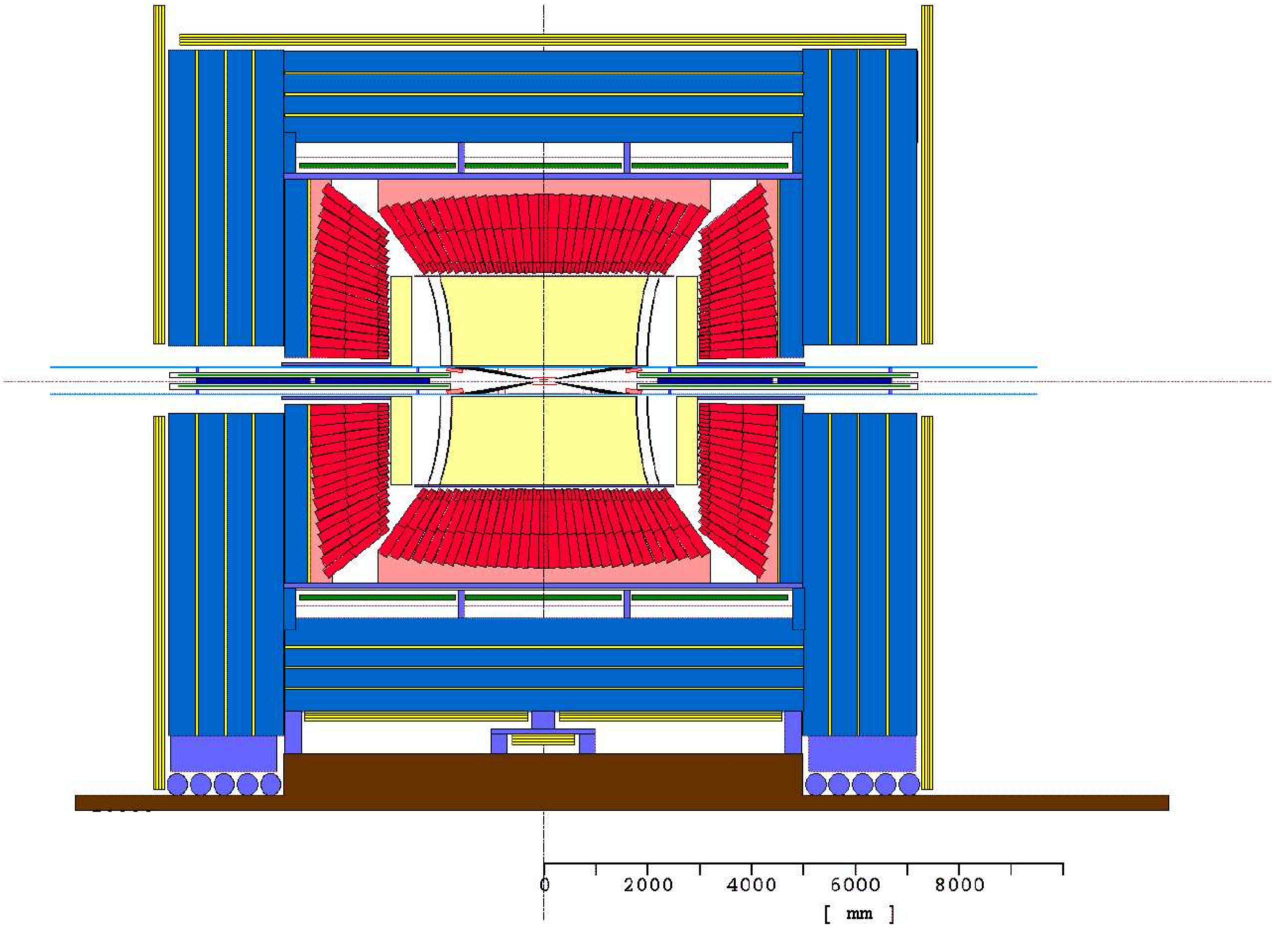

Figure 1.3: The JLC detector.

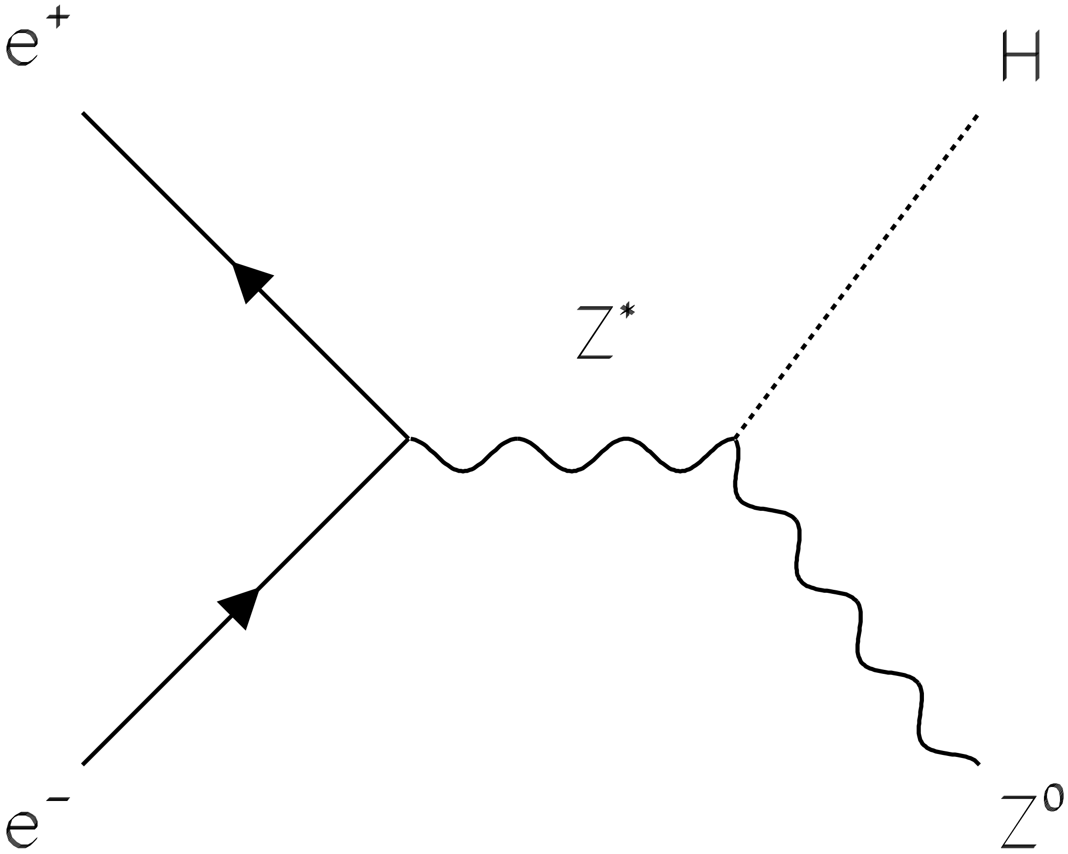

Figure 1.4: Feynman diagram of $e^+e^- \rightarrow HZ$.

Chapter 2

Calorimeter and Compensation

2.1 Calorimeter

2.1.1 Cascade shower and Calorimeter

Calorimeter is a detector which measure the energy of the particles using a cascade shower. Particles incident a material at high energy, create particles secondly by electromagnetic or strong interaction. Secondary particles can also create particles in a material. Cascade shower is created by this process over and over. Secondary particles in the cascade shower are called shower particles. Some of shower particles which are charged, deposit their energy in the materials by the ionization process. The creation of the shower particles continues until the shower particles can not create the next generation shower particles because they do not have an enough energy. This energy is called a critical energy. The number of shower particles is proportional to the energy of the incident particle. Charged path length of shower particles and deposition energy is also proportional to the energy of the incident particle. We can measure the energy of the incident particle by measuring the deposition energy in the materials or counting the number of shower particles.

Energy resolution of the calorimeter is well discribed by the followring equation.

$$\frac{\sigma}{E} = \frac{\sigma_{stocastic}}{\sqrt{E}} \oplus \sigma_{constant} \oplus \frac{\sigma_{noise}}{E} , \tag{2.1}$$

where $A \oplus B \oplus C \equiv \sqrt{A^2 + b^2 + C^2}$, E is the energy of the incident particle. $\sigma_{stocastic}$ comes from the stocastic fluctuation of the number of the shower particles. $\sigma_{constant}$ comes from the systematics which depends on the calorimeter. In general, the sources of this term are calibration uncertainty, shower leakage and non-uniformity of the calorimeter. σ_{noise} comes from a noise on read out electronics. $\sigma_{stocastic}$ depends on the calorimeter configuration and type of the interaction. $\sigma_{stocastic}$ for a scintillator sandwich type calorimeter is given by

$$\sigma_{stocastic} = \sigma_{intrinsic} \oplus \sigma_{sample} \times \sqrt{d} \oplus \sigma_{photostat} , \tag{2.2}$$

where d is a thickness of an absorber layer. $\sigma_{intrinsic}$ depends on the interaction of the secondary particles. σ_{sample} is called the sampling fluctuation that only appeared in a sampling calorimeter. This term depends on both the chemical material of the absorber and the detection scheme. $\sigma_{photostat}$ comes from a photo-electron fluctuation in the photo-device and only appeared in the calorimeter where the photo-device is employed for the measurement of the light yield.

Cascade shower is classified into electromagnetic shower and hadron shower by the interaction of the secondary particles creation. They are discribed in detail in the following sections.

2.1.2 Electromagnetic (EM) shower

Electrons and photons interact in a material by the electromagnetic interaction. Electrons in the material emit photon by the bremsstrahlung process. A photon in the material creates an electron-positron pair. An electron loses energy by bremsstrahlung at a rate nearly proportional to its energy, while the ionization loss rate varies only logarithmically with the electron energy. Electromagnetic cascade grows by these processes, until the critical energy E_c. The critical energy E_c is sometimes defined at which the two loss rates are equal. The approximation of the E_c is given by

$$E_c = \frac{(800MeV)}{(Z + 1.2)}, \tag{2.3}$$

where Z is an atomic number of the material.

In dealing with electrons and photons at high energies, it is convenient to measure the thickness of the material in units of the radiation length X_0. X_0 is the mean distance over which a high-energy electron loses all but $1/e$ of its energy by bremsstrahlung.

The radiation length X_0 is a function of the atomic and mass numbers of the material. It is given by

$$X_0 = \frac{716.4 \text{ g/cm}^{-2}\text{A}}{Z(Z+1)\ln(287/\sqrt{Z})}, \tag{2.4}$$

where A is a mass number of the material. For Pb, the critical energy E_c and the radiation length X_0 are 9.62 MeV and 6.37 g/cm^2 (0.56 cm) from Eqs. (2.3) and (2.4), respectively.

The mean of longitudinal profile of the energy deposition in an electromagnetic cascade is well described by a gamma distribution.

$$\frac{dE}{dt} = E_0\, b\, \frac{(bt)^{a-1}e^{-bt}}{\Gamma(a)}, \tag{2.5}$$

where t is a calorimeter depth measured in units of radiation length. b is called a thickness scale factor. From Eq. (2.5), the maximum t_{max} is at the depth given in the following equations:

$$t_{max} = (a-1)/b \tag{2.6}$$

and

$$t_{max} = \ln y + C_j \tag{2.7}$$

where $y = E_0/E_c$, $j = \mathrm{e}$ or γ, $C_{\mathrm{e}} = -0.5$, $C_\gamma = +0.5$ for electron and photon induced cascades.

The scale factor b has a dependence on energy and material, however it is approximately $b \approx 0.5\ \mathrm{X}_0$ very roughly.

2.1.3 Hadron shower

Hadrons interact with a nucleus in the material by strong force process. Then secondary particles are produced, baryons, mesons, and exited-nucleus. They can also interact with a nucleus and produce particles. Baryons and mesons in this process can decay into hadrons, leptons, neutrinos, and photons. Exited-nucleus can emit photons, electrons, and neutrinos by nuclear level de-excitation or β-decay.

Each of electrons and photons grows up as an EM shower. The other charged particles deposit their own energy by the ionization process. Neutrinos escape without energy deposit in the calorimeter. Neutrons also escape if they never interact to produce any charged particles. Muons penetrate through the calorimeter with the ionization energy deposit if they do not stop and decay in the calorimeter.

The length scale appropriate for hadronic cascades is the nuclear interaction length. The nuclear interaction length is the mean free path for the inelastic scattering, and given very roughly by

$$\lambda_I \approx 35\,\mathrm{g\ cm^{-2}\ A^{-3}}\,, \tag{2.8}$$

where A is a mass number of the material. For Pb, the nuclear interaction length λ_I is 194 g/cm^2 (17.09 cm).

2.1.4 Homogenous calorimeter and Sampling calorimeter

In order to measure the incident energy, we have to detect the energy deposition by the shower particles. We have two ways to detect it.

- Homogenous calorimeter: It is a calorimeter which measures all energy deposition or the number of charged particles. In general, it has a better energy resolution for EM shower than a sampling calorimeter. However, it has never been employed for hadron calorimeters, because it is too difficult technically and in cost to create large crystal enough to stop the hadron shower. In order to detect the energy deposition, a crystal scintillator is used which have a high density to stop all the shower particles, for example BGO and CsI. Lead glass is also used with measuring the number of charged particles by a Cherenkov light. These calorimeter measure the energy by the yield of scintillation or Cherenkov light.

- Sampling calorimeter : It consists of absorbers and active volumes. For absorbers, materials are chosen which has a large atomic number in order to make the grow of cascade shower faster, for example lead. For active volumes, we choose what can detect the energy deposit by charged particles in the cascade shower, such as a proportional gas chamber and a plastic scintillator. In this scheme, sampled energy deposit of all shower particles are measured. For both EM and hadron calorimeters, the sampling calorimeter is used because it is cheaper than the homogenous calorimeter.

2.2 Compensated Calorimeter

2.2.1 Hadron Shower

In general, the signal pulse height from the calorimeter for hadron shower is different from that for EM shower and lower than that for EM shower. The mean energy of secondary particles in EM shower is lower than that in hadron shower. Hadron shower has both invisible and visible components. Hadron energy is lost its in the process of breaking up the nuclei by the binding energy of the nuclei and it is invisible. Hadron shower includes the other invisible components, neutrons which are produced in the hadron-nuclei scattering, neutrinos and μ which are produced in the decay of mesons such as π and K. The ratio between invisible and visible components fluctuates shower by shower. It degrades the energy resolution for hadrons.

Hadron shower also includes an EM compornent and a pure hadron one. The EM compornent in the hadron shower comes from electrons and photons produced in the decay of hadrons, such as π^0 or the nuclear level de-excitation. THe hadron shower compornent except for the EM compornent is called the pure hadron compornent. Hadron shower also has a fluctuation of the ratio between EM compornent and pure hadron one. If the calorimeter has the difference between the pulse heights for EM shower and hadron one, this fluctuation degrades the energy resolution for hadrons. A jet includes baryons, mesons, leptons, and neutrinos. The ratio of them fluctuates event by event. This fluctuation also degrades the energy resolution for jets as discussed before.

2.2.2 Compensation Scheme

To equalize the pulse heights for the EM shower and the hadron one, we must convert the invisible component in hadron shower to the visible component and suppress the EM shower pulse height. In the invisible component, neutrons play an important role because they only can be converted to the visible compornent. We can convert neutrons to the visible component using a nuclear fission or a neutron-proton scattering.

To use the nuclear fission scheme, we have to choose the material which can interact with neutron and cause nuclear fission such as uranium 238 for absorber. Products by the nuclear fission can contribute to the calorimeter signal. We can equalize the pulse heights for EM shower and hadronic one to take an optimized ratio between the passive and active volumes. The calorimeter using uranium 238 for absorber was employed in the ZEUS detector. It has the energy resolution of about $35\%/\sqrt{\mathrm{E}}$ for hadrons [5], [8].

To use the neutron-proton scattering scheme is another way to convert neutrons to the visible component. It is based on that we can control the ratio of the invisible neutron to the visible proton, by taking an optimized ratio of passive and active volume. For this scheme, it is important for the calorimeter active volume to include many protons. We can construct a calorimeter with plastic which includes a lot of hydrogen for active volume.

To suppress the EM shower pulse height, a low volume ratio is needed. However, the low volume ratio degrades of the energy resolution for EM shower. We can keep a good energy resolution for EM shower to use higher sampling frequency.

2.2.3 Compensation ratio e/h, e/π

Taking into account these effects, if we choose materials and set a volume ratio suitably, we can equalize the calorimeter pulse heights for the EM and hadronshowers. The e/h (Eq.(1.1)) is a function of the materials and the volume ratio of absorber and active material, independent of the sampling frequency. The calculated e/h ratios [2] are shown in Fig. 2.1 as a function of the volume ratio for Pb absorber. The e/π is sometimes measured instead of the e/h for the evaluation of the compensation. The e/π is defined as follows:

$$\mathrm{e}/\pi \equiv \frac{\text{pulse height for EM shower}}{\text{pulse height for charged } \pi} \quad . \tag{2.9}$$

The relation between e/h and e/π(E) is given by

$$\mathrm{e}/\pi = \frac{\mathrm{e/h}}{1 + (\mathrm{e/h} - 1)0.11 \ln \mathrm{E}} \, , \tag{2.10}$$

where E is in GeV. The e/h and e/π were measured in some experiments [4], [6], [7], [4] at a fixed volume ratio, however it has not been measured as a function of the volume ratio between the absorber and the active material in the Pb-plastic scintillator calorimeter.

2.3 Beam test of compensating hadron calorimeter

We performed the beam test of a lead-tile/fiber sampling hadron calorimeter from February to March and from May to July 1997 at the KEK-PS π2 area. The goal of the beam test is to measure the volume ratio dependence of e/π, resolution, and the other characteristics of lead plastic scintillator calorimeter (in Chapter5). We are able to optimize the compensation ratio where the energy resolution for hadrons is minimized using our data.

2.3.1 Calorimeter prototype module

For the beam test, we made a calorimeter prototype where the lead absorber thickness is changeable by employing a "hanging-file" configuration where the absorber plates and scintillator sheets are "hanged" over a pair of parallel beams as Shown in Fig. 2.2. Thickness of the Pb plates are changeable by 2 mm. We can configure the different volume ratio by changing the thickness of the Pb plates.

Tile/fiber techniques are employed for our calorimeter prototypr read out in order to configure the calorimeter easily, even though the absorber thickness is changed. The tile/fiber system for this calorimeter prototype is shown in Fig. 2.3. The tile is 1 m $\times$ 1 m, and 2mm thick. Each tile has six straight grooves with a key hole shape (see Fig. 2.3). The tile edges are painted white with 'Odecoat'. The tile/fiber system is wrapped in PET films.

The fiber is made up of a 1 m long wave-length-shifter fiber (WLS fiber) and two clear fibers. The clear fibers are spliced by a heat fusing method at both ends of the WLS fiber [15]. The diameter of the fibers is 1 mm. We used Kuraray SCSN38 and 88 scintillator and Y11 multiclad WLS fibers [9], [12], [13], [14].

The five layers of the scintillator sheets compose a superlayer. Each side of the clear fibers in the single superlayer are connected to a phototube.

2.3.2 Tile/fiber system

Tile/fiber techniques are employed in many of the next generation calorimeters, CDF [9] endplug upgrade calorimeter (EM+hadron), ATLAS [10], and CMS [11] hadron calorimeters. Advantages of scintillating tile/fiber calorimeters are summarized as follows:

- fast response
- small dead space
- good uniformity
- fibers are flexible, which eases us to design the location of photo-devices
- easy to segment longitudinally

Typical shape of tile/fiber system is shown in Fig. 2.4. The tile/fiber system consists of a scintillation tile with groove(s), a fiber made up of a wave-length-shifter (WLS) fiber spliced to a clear fiber by heat fusing method. The end of the WLS fiber in the tile is mirrored by Al spattering. method.

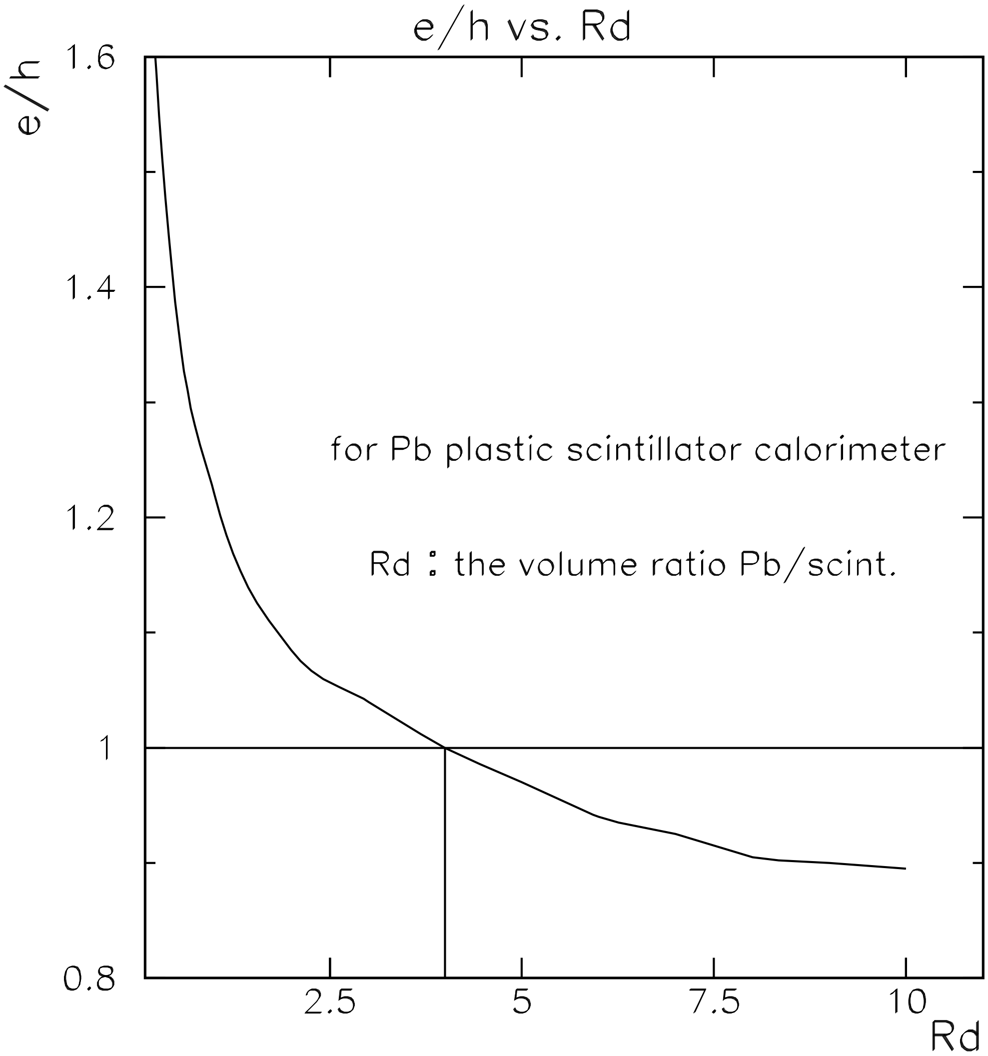

Figure 2.1: The e/h ratio vs. the volume ratio for Pb/plastic scintillator calorimeter.

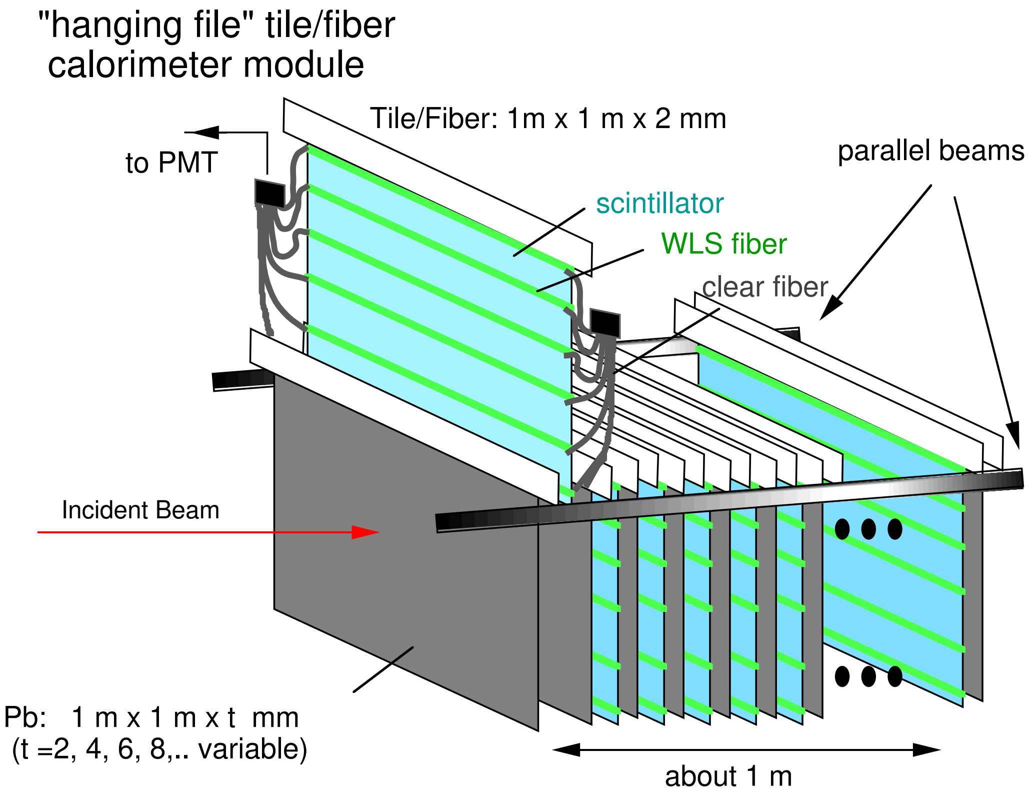

Figure 2.2: Schemetic view of the beam test module ("hanging file").

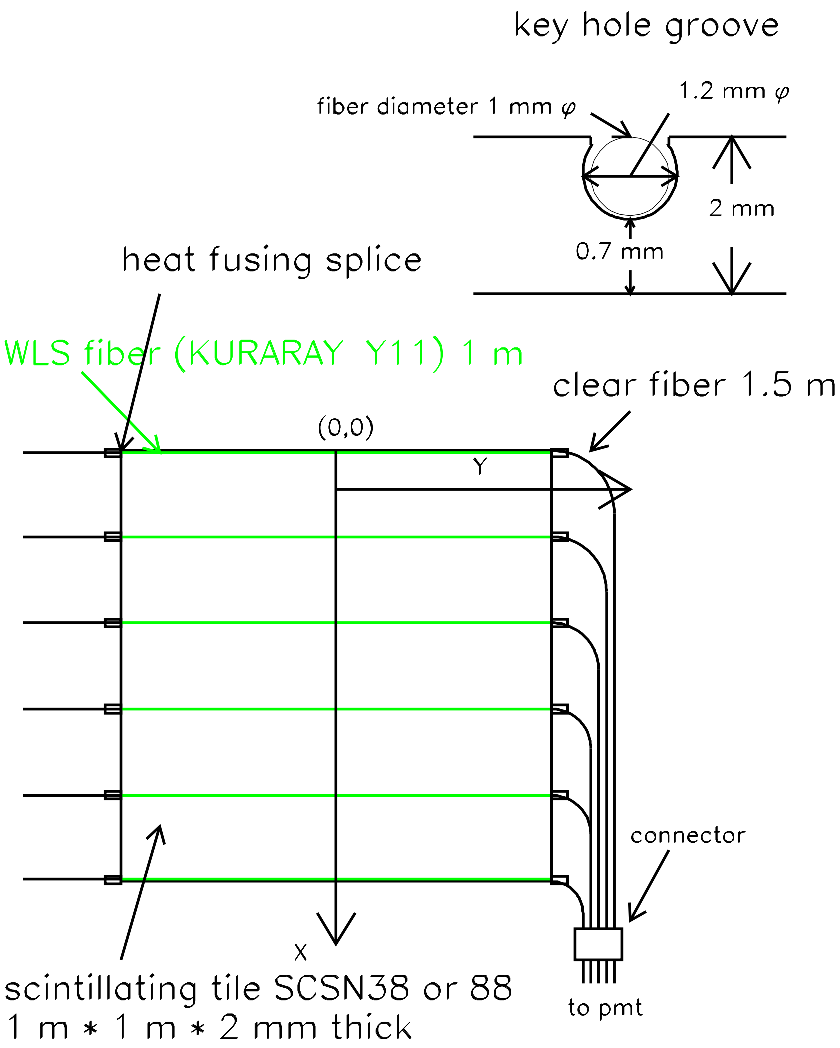

Figure 2.3: The tile/fiber system for the beam test module.

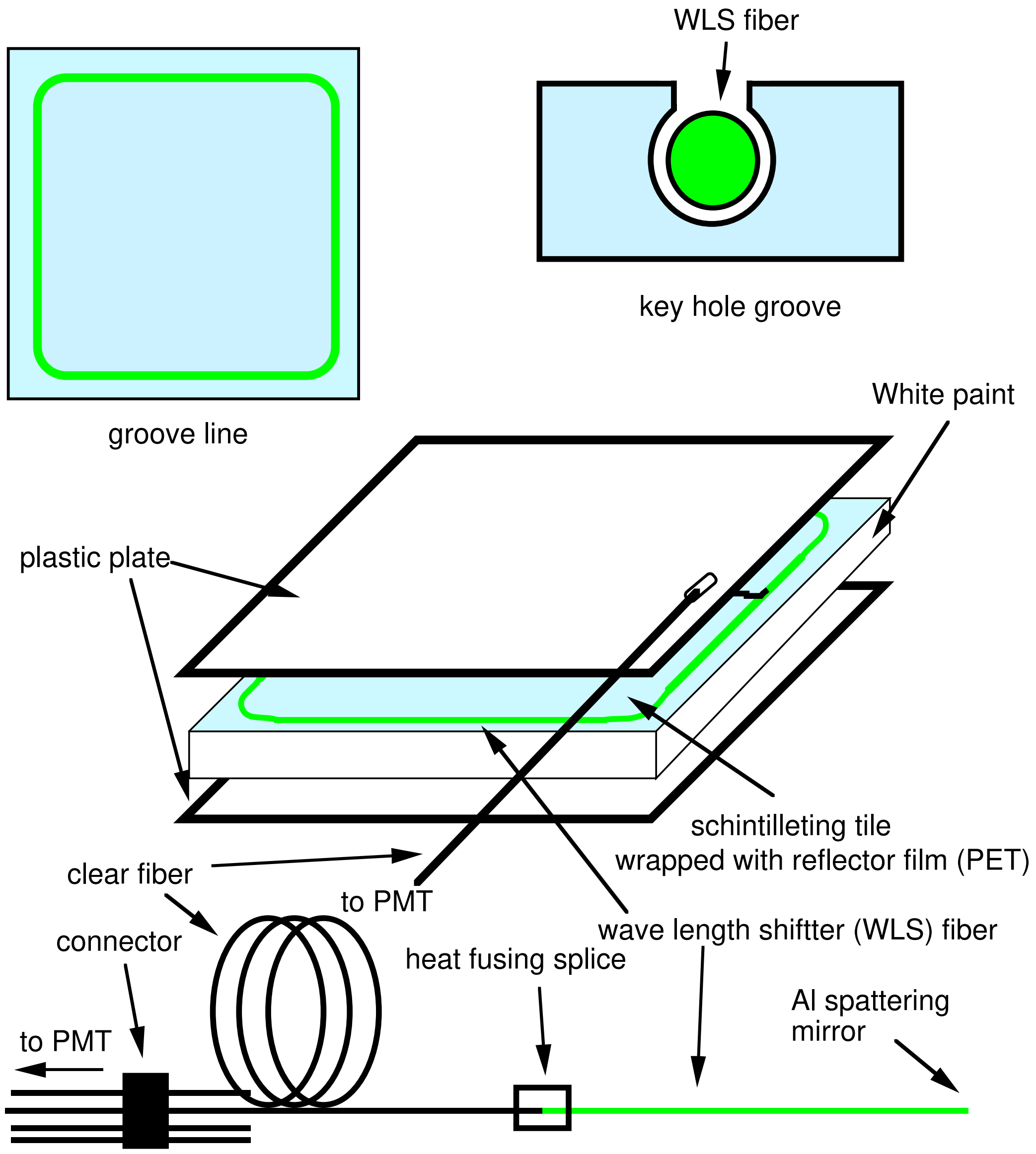

Figure 2.4: Typical shape of tile/fiber system.

Chapter 3

The light yield measurement of the tile/fiber systems

3.1 Measurment system and evaluation of the light yield

A scheamatic view of our measurement system is shown in Fig. 3.1. The arm with a ^{90}Sr source and a trigger counter is drived by a computer controled stepping motor. Position resolution in the scanning is less than 200 μm. The radius of the collimeter is 5mm and the size of trigger counter is 1 mmϕ. We had collected the event where β-ray penetrated through the scintillator tile to the trigger.

We evaluate the light yield as the number of photoelectrons emerging from a set of standard phototubes (HAMAMATSU H1161GS). The light yield is given by

$$Ly(NPE) = \frac{\text{mean of the pulse height distribution}}{SPP}\,, \tag{3.1}$$

where SPP is the Single Photo-electron Peak measured with an ADC. The single photoelectron peak is measured with a dedicated tile/fiber system which yields the light yield of about 0.1 photoelectrons so that we detect 0 (pedestal) and 1 photoelectron (SPP) events in most of the cases. Typical signal and SPP pulse height distributions are shown in Fig. 3.2.

3.2 Results

The typical light yield vs. position is shown in Figs. 3.3 and 3.4. In the direction across the fibers, the light yield peaks at the points near the fibers. In the direction parallel to fibers, the light yield is flat except in the regions near the tile edges.

The average light yield and its rms variation in a tile in the direction across the fibers (except the points near the fibers) are 1.67 ± 0.24 photoelectrons/mip (minimam ionizing particle) and $5.0 \pm 2.7\%$, as shown in Fig. 3.5, respectively. The rms variation in the direction parallel to the fibers (Fig. 3.4) is 3%.

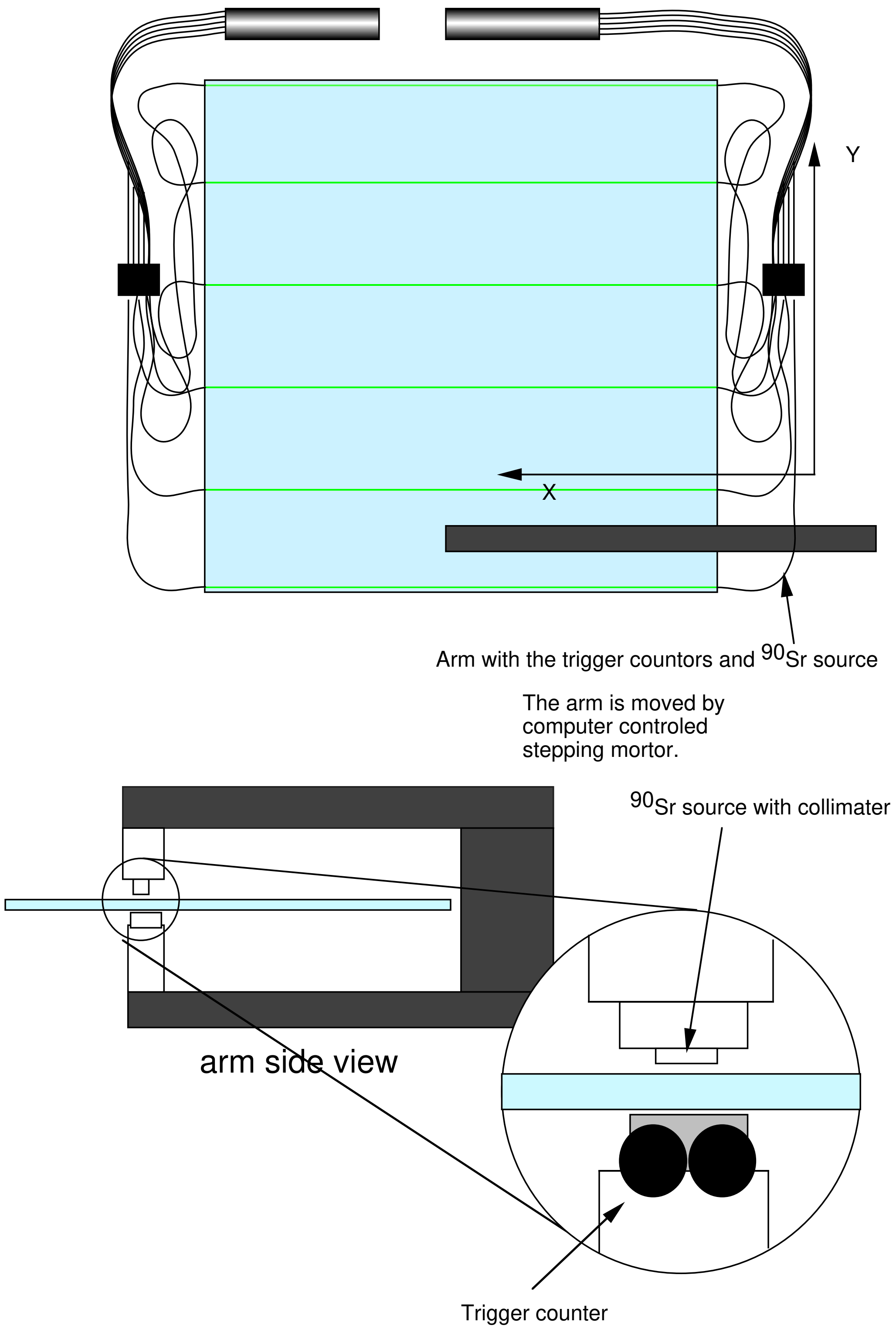

Figure 3.1: Schematic view of the source scanning system.

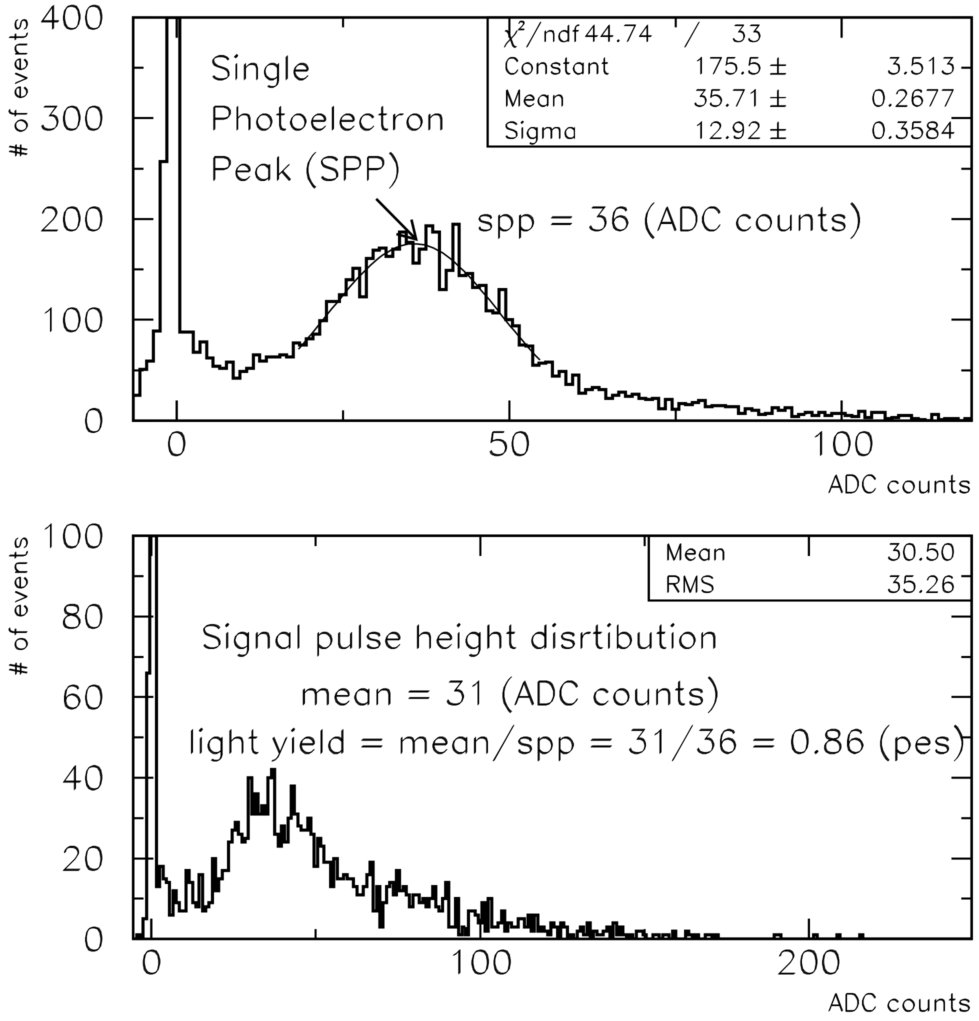

Figure 3.2: Typical pulse height distributions of single photoelectron events (top) and signal (above).

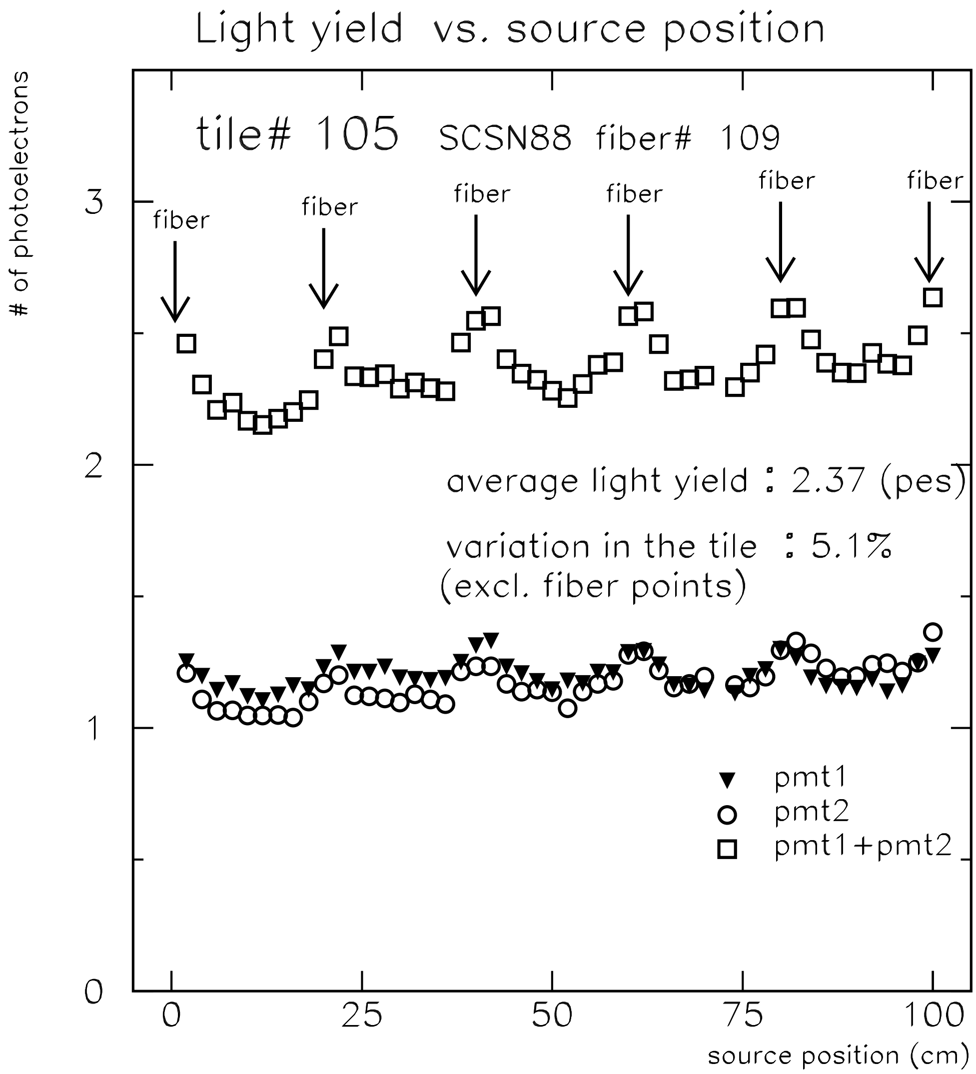

Figure 3.3: Light yield vs. position scanned along the arrowed line (X) shown in Fig. 2.3.

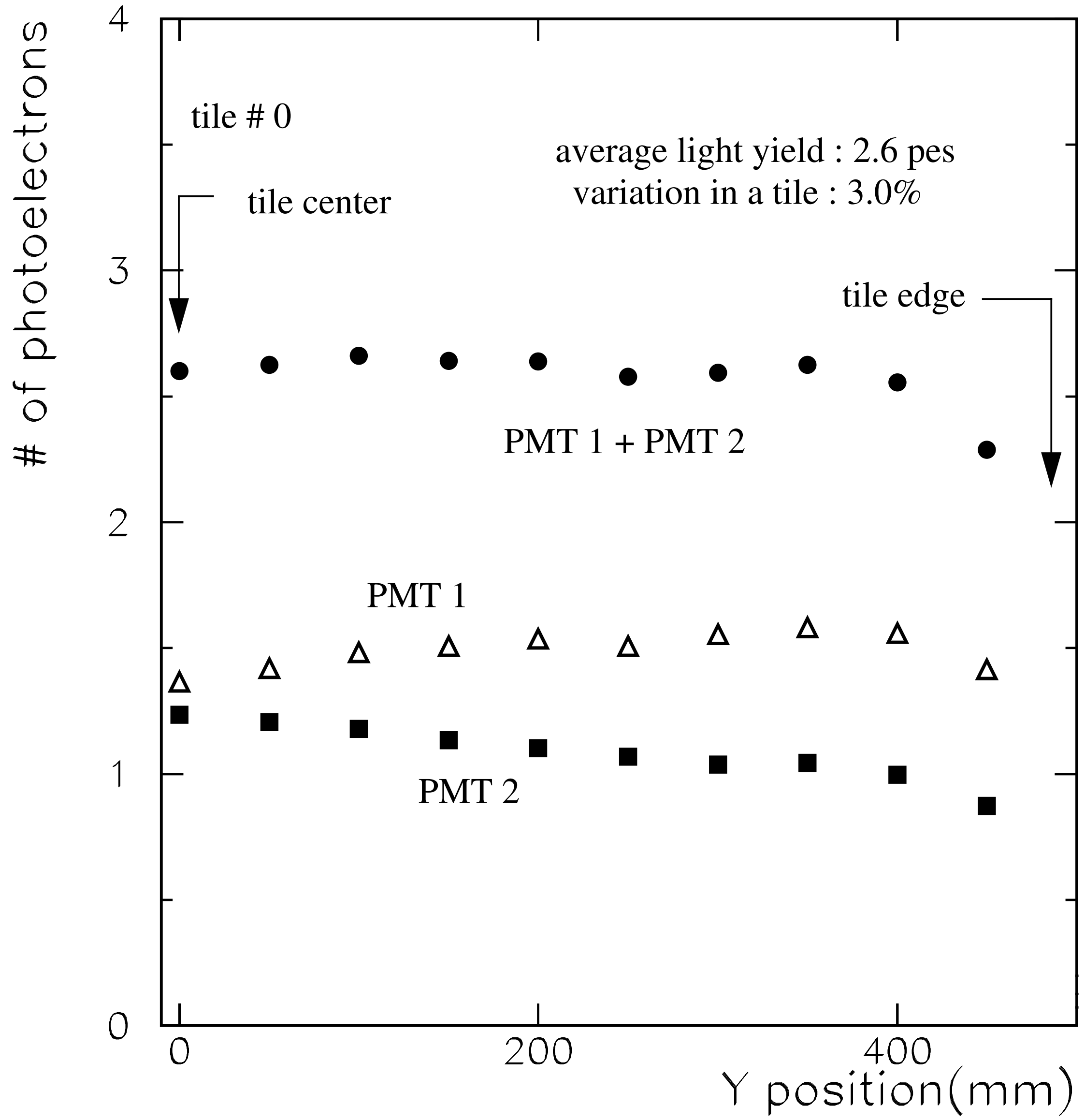

Figure 3.4: Light yield vs. position scanned along the arrowed line (Y) shown in Fig. 2.3.

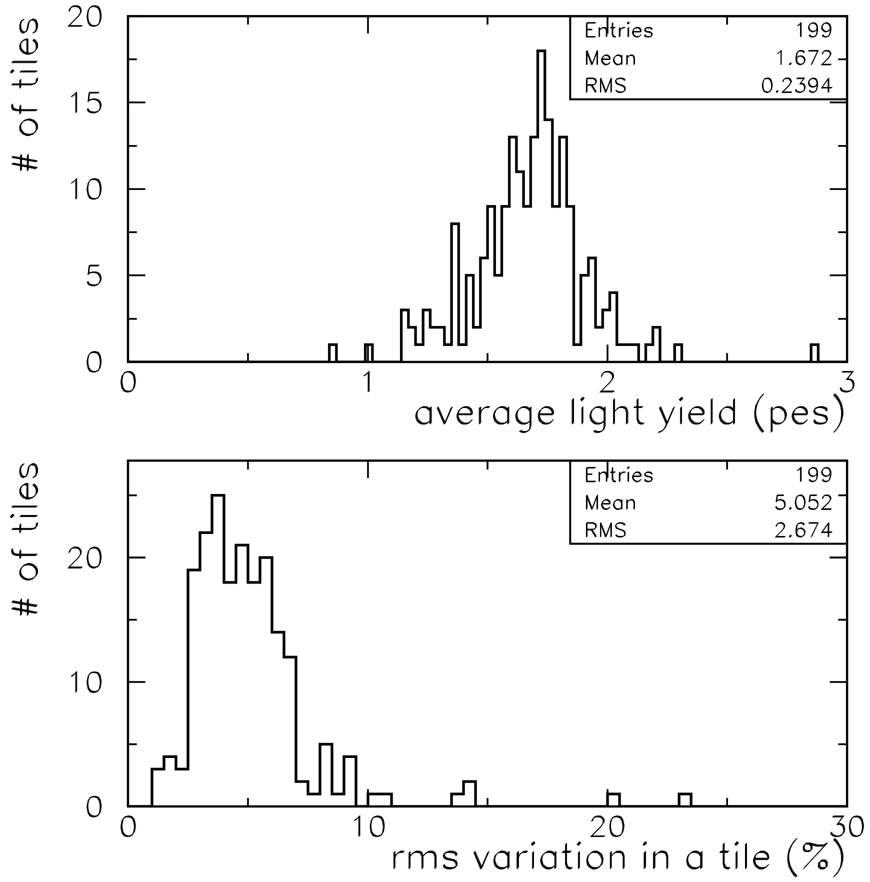

Figure 3.5: The average light yield (top) and its rms variation (above) in a tile in the direction across the fibers (except the points near the fibers).

Chapter 4

GEANT simulation

4.1 GEANT setting

Using a GEANT[23] shower simulation, we evaluated the performance of the calorimeter prototype consisting of such tile/fiber systems as measured in our test bench. To include the non-uniformity of the tile/fiber systems, the energy deposit were recorded in strips of 10 mm wide. The calorimeter module had 120 layers of the 2mm thick tiles and 8 mm thicvk Pb plate. The cut off energies in the simulation were set to 10 keV for electrons and γ's and 100 keV for hadronic particles. We turn on all the interaction processes available in GEANT.

4.2 Calculation of the calorimeter response

We calculate the response of the calorimeter in unit of the number of photo-electrons (pes):

$$Ly[NPE] = \sum_{l=1}^{120}\sum_{x=0}^{100}\frac{Edep(x,l)}{Edep(mip)} \times ly(x) \tag{4.1}$$

where Ly is the light yield sum of all tiles, $Edep(x,l)$ is the energy deposit in layer l at lateral position x, $Edep(mip)$ is the energy deposit in a tile per mip (0.482 MeV), and $ly(x)$ is the light yield in the number of photo-electrons par mip at position x in a tile. The effect of photo-statistics is included.

4.3 Results

4.3.1 Energy resolution dgradation

The energy resolution degradations are summarized in Table 4.1. The energy resolution degradations for electrons due to photo-statistics(1.67 pes/mip/tile), lateral non-uniformity and longitudinal(layer-by-layer : 15%) non-uniformity are $(11 \pm 3\%)/\sqrt{E}$, $0.0 \pm 0.2\%$ and $2.4 \pm 0.3\%$,respectively. The total energy resolution degradation is 6 $\pm$ 3% for 4 GeV electrons. The energy resolution degradations for π's due to photo-statistics(1.67 pes/mip/tile), lateral non-uniformity and longitudinal(layer-by-layer : 15%) non-uniformity are $(11 \pm 3\%)/\sqrt{E}$, $0.1 \pm 0.1\%$ and $5.8 \pm 5.0\%$. The total energy resolution degradation is $6 \pm 5\%$ for 4 GeV pions.

degradation source	energy resolution degradation	
	for e^-	for π^-
photo-statistics	$(11 \pm 3\%)/\sqrt{E}$	$(11 \pm 3\%)/\sqrt{E}$
lateral non-uniformity	$0.0 \pm 0.2\%$	$0.1 \pm 0.1\%$
longitudinal non-uniformity	$2.4 \pm 0.3\%$	$5.8 \pm 5.0\%$
total for 4GeV	$6 \pm 3\%$	$6 \pm 5\%$

Table 4.1: Summary of energy resolution degradation.

4.3.2 Systematic uncertainty on the e/π ratio

The systematic uncertainties on e/π due to lateral non-uniformity and longitudinal(layer-by-layer : 15%) non-uniformity are $0.4 \pm 0.1\%$ and $5 \pm 2\%$ as summarized in Table 4.2. The total systematic uncertainties on the e/π ratio is $5 \pm 2\%$

source	Systematic uncertainty for e/π
lateral non-uniformity	$0.4 \pm 0.1\%$
longitudinal non-uniformity	$5 \pm 2\%$
total	$5 \pm 2\%$

Table 4.2: Summary of systematic uncertaintues on e/π.

Chapter 5

Beam test of hadron calorimeter

5.1 Experimental setup of the beam test

We performed the beam tests at the $\pi 2$ beam line KEK-PS from February to March (we called this term T405) and from May to June (we called this term T411) in 1997. Experimental setups of the beam test are shown in Fig. 5.1.

The beam was defined by scintillation trigger counters: S1, S2, and S3 for T405 and S1, S2, S3, and S4 for T411. Additional counters M1 and M2 were located behind the backup calorimeter(s) and were used to tag muons. Particle identification was provided by two Cherenkov counters, C1 and C2, filled with CO_2 gas. Their pressures were set to a certain value where we can recognize electrons and 4 GeV muons.

The Cherenkov counters and the scintillation trigger counters were used to define three different trigger conditions. The beam signal is a coincidence between S1, S2,

configuration Pb:Scint. (in mm)	6:2	8:2	10:2	12:2	14:2	16:2
# of layers	105	105	100	70	70	55
# of superlayers	21	21	20	14	14	11
# of PMTs	42	42	40	28	28	22
total absorber length (λ_I)	3.69	4.92	5.85	4.92	5.73	5.15

Table 5.1: Tested calorimeter configurations in the term T405

configuration Pb:Scint. (in mm)	4:2	6:2	8:2	10:2	16:2
# of layers	210	160	120	100	55
# of superlayers	42	32	24	20	11
# of PMTs	84	64	48	40	22
total absorber length (λ_I)	4.92	5.62	5.62	5.85	5.15

Table 5.2: Tested calorimeter configurations in the term T411

and S3 (for T405), S1, S2, S3, and S4 (for T411). The electron trigger requires a coincidence between the beam signal and the signals in the Cherenkov counters C1 and C2. The muon trigger requires a coincidence between the beam signal and the signals in M1 and M2. The pion trigger is just the beam signal.

All the measurements were performed with negatively charged particles. Beam momentum was set to 1, 2, 3 and 4 GeV. The momentam spread is 1%. Beam includes π, μ, and electron. Fraction of the μ and electron in the beam is about 1/1000. Shown in Tables 5.1 and 5.2 are the calorimeter prototype configurations which we performed at the beam test.

5.2 Calibration

The muon trigger events with a beam momentum of 4 GeV are used to calibrate the signals phototube by phototube. We define the pulse height per mip per phototube, by a mean of the pulse height distribution for 4 GeV muon trigger events. The calorimeter signals are calculated in units of this pulse height. The pion contamination in the muon sample is about several percents. This contamination brings a shift of the pulse height mean for muon trigger events, especially for the forward superlayers.

In order to remove this effect, we perform the calibration along the following sequence.

1 - Obtain primary calibration constants using 4 GeV muon events without muon identification(see next section).

2 - Calibrate using 4 GeV muon events with muon identification with the above calibration constant.

3 - Calibrate using 4 GeV muon events with muon identification with the above calibration constant, again.

We check no difference in the calibration constants between ones at sequence-2 and ones at sequence-3. Typical calibrated pulse hight distributions for 4 GeV electrons, μ's, and π's of the configuration of 8 mm Pb and 2 mm Scint. in T411 is shown in Fig. 5.2.

5.3 Event selection

The criteria used to isolate samples of electrons, muons, and pions in the offline analysis were based on the signals delivered by the single wire drift chambers (SWDC) and the calorimeter itself. At first, we require the reasonable timings of SWDC signals and that there are not the calorimeter ADC signals below the pedestal in order to select the events without a trigger error and unreasonable response of the DAQ system.

The selection of the electron, muon, and pion events was based on the longitudinal shower profile measured with the calorimeter. We define the quantity named VAR by the rms variation from the signals of all phototubes, normalized by the average of all phototubes in the event. Shown in Fig. 5.3 is the typical distribution of the quantity VAR for the electron, muon, and pion trigger events. For muon events, the VAR is small because the signals from all the phototubes are similar to each other within a fluctuation of dE/dx and photostatistics. For electron events, signals in forward superlayers are large, and these in backward are none or very small. The quantity VAR is large for electron events. The VAR for pions distributes between these for muons and electrons.

5.4 Longitudinal shower profile for electrons

Longitudinal shower development for electrons is well represented by equations (2.3), (2.4), and (2.5). In figure 5.4 shown is the longitudinal shower profile for electrons as a function of calorimeter depth measured in units of X_0.

Including the normalization factor the longitudinal shower development for electrons (Eq. (2.5)) is given by

$$\frac{dE}{dt} = f \times E_0 \; b \, \frac{(bt)^{a-1} e^{-bt}}{\Gamma(a)}, \tag{5.1}$$

where E is the energy measured with the calorimeter, f is the normalization factor, and E_0 is the beam energy. Solid curves shown in Fig. 5.4 are the fitted result with Eq. (5.1). The data, from the north-side, the south-side, and total of readouts are fitted very well to the curve given by Eq. (5.1). Fitted parameters are listed in Table 5.3 and shown in Figs. 5.5, 5.6, 5.7, 5.8, 5.9, and 5.10.

In general, thickness scale b depends weeekly upon energies and is independent of the calorimeter configurations. We can see that it depends slightly on energies and the calorimeter configurations as shown in Figs. 5.5 and 5.6.

Shown in Figs. 5.7 and 5.8 are t_{max} calculated with Eq. (2.6) using the fitted a and b. t_{max} should be independent of the configuretions and depends on the beam energy as shown in Fig. 5.8. t_{max} has a dependence on the energy as shown in Figs. 5.8 and 5.7. Solid curves in Figs. 5.8 and 5.7 are obtained with Eq. (2.7). The data agree with the calculation except for d of 4 mm. It is because our measurement is performed by a superlayer and readout, that is too rough to measure the shower curve around the shower maximam especially for small d. If we have finer segmentation in the longitudinal direction, we can measure more accurate shower maximam for electrons.

configuration (Pb:scint. in mm) and energy	$b\,(X_0^{-1})$	a	f (mip/Layer/GeV)
4:2 in T411 1 GeV	0.41 ± 0.01	2.38 ± 0.09	390 ± 10
4:2 in T411 2 GeV	0.43 ± 0.01	2.84 ± 0.07	403 ± 10
4:2 in T411 3 GeV	0.41 ± 0.01	2.85 ± 0.07	403 ± 8
4:2 in T411 4 GeV	0.39 ± 0.01	2.86 ± 0.07	395 ± 10
6:2 in T405 1 GeV	0.38 ± 0.02	2.27 ± 0.17	375 ± 13
6:2 in T405 2 GeV	0.41 ± 0.02	2.71 ± 0.13	385 ± 10
6:2 in T405 3 GeV	0.38 ± 0.01	2.66 ± 0.12	390 ± 10
6:2 in T405 4 GeV	0.37 ± 0.01	2.68 ± 0.17	380 ± 10
6:2 in T411 1 GeV	0.41 ± 0.02	2.51 ± 0.16	390 ± 13
6:2 in T411 2 GeV	0.43 ± 0.02	2.91 ± 0.13	398 ± 10
6:2 in T411 3 GeV	0.42 ± 0.01	3.13 ± 0.12	403 ± 10
6:2 in T411 4 GeV	0.42 ± 0.01	3.15 ± 0.11	403 ± 10
8:2 in T405 1 GeV	0.35 ± 0.03	2.17 ± 0.25	400 ± 20
8:2 in T405 2 GeV	0.40 ± 0.02	2.85 ± 0.21	380 ± 13
8:2 in T405 3 GeV	0.39 ± 0.02	2.93 ± 0.20	378 ± 13
8:2 in T405 4 GeV	0.37 ± 0.02	2.90 ± 0.18	360 ± 10
8:2 in T411 1 GeV	0.45 ± 0.03	2.97 ± 0.26	374 ± 13
8:2 in T411 2 GeV	0.45 ± 0.02	3.22 ± 0.20	395 ± 13
8:2 in T411 3 GeV	0.44 ± 0.02	3.31 ± 0.18	408 ± 13
8:2 in T411 4 GeV	0.44 ± 0.02	3.43 ± 0.17	403 ± 13

Table 5.3: Summary of the results of longitudinal shower profile for electrons fit to Eq (5.1).

The normalization factors f is shown in Figs. 5.9, and 5.10. If f has a dependence on energy, the responce of the calorimeter to electrons is not a linear function of the energy. However, we do not find any energy dependences on energy of f as shown in Figs. 5.9. This results indecate that the calorimeter has a good linearity for electrons. Non-linearity from f is defined by the rms variation of the fitted f for each configuration. The non-linearity estimated from the fitted f is shown in Fig. 5.11 and listed in Table 5.5. The non-linearity for electrons from f is less than 4%.

configuration	t_{max} (X_0)			
Pb:scint. (in mm)	1 GeV	2 GeV	3 GeV	4 GeV
4:2 in T411	3.40 ± 0.25	4.24 ± 0.20	4.55 ± 0.19	4.74 ± 0.19
6:2 in T405	3.32 ± 0.48	4.18 ± 0.33	4.40 ± 0.39	4.54 ± 0.41
6:2 in T411	3.70 ± 0.43	4.48 ± 0.34	4.90 ± 0.32	5.07 ± 0.31
8:2 in T405	3.33 ± 0.78	4.66 ± 0.59	4.97 ± 0.57	5.19 ± 0.56
8:2 in T411	4.36 ± 0.66	5.00 ± 0.52	5.29 ± 0.48	5.54 ± 0.43
10:2 in T405	2.96 ± 1.38	4.82 ± 0.78	4.98 ± 0.72	5.01 ± 0.80
10:2 in T411	no data	can not fit	6.54 ± 0.66	5.71 ± 0.57
12:2 in T405	can not fit	can not fit	4.58 ± 1.01	4.60 ± 1.32

Table 5.4: t_{max} calculated from Eq. (2.6) for electrons.

5.5 Longitudinal shower profile for π's

Longitudinal shower development for π's is not so well known as one for electrons. Figure 5.12 shows the longitudinal shower profile for π's as a function of calorimeter depth measured in units of λ_I.

We assume that the function of longitudinal shower development for π's is the same as for electrons, Eq. (5.1), with the depth unit of λ_I. Solid curves shown in Fig. 5.12 is the fitted result with Eq. (5.1). The data are fit with that very well. The fitted parameters of the result are also listed in Tables 5.6, 5.7 and shown in Figs. 5.13, 5.14, 5.15, 5.16, 5.17, and 5.18.

Thickness scale b has a weak dependence upon energy, similarly to that for electrons. It depends slightly dependence on energies and configurations as shown in Figs. 5.5 and 5.6.

Shown in Figs. 5.15 and 5.16 are t_{max} calculated with Eq. (2.6) using the fitted a

calorimeter configuration	for electrons	for π's
Pb:scint. = 4 mm:2 mm in T411	$1.2 \pm 0.4\%$	$0.8 \pm 0.3\%$
Pb:scint. = 6 mm:2 mm in T405	$1.2 \pm 0.4\%$	$2.1 \pm 0.7\%$
Pb:scint. = 6 mm:2 mm in T411	$1.1 \pm 0.4\%$	$2.4 \pm 0.8\%$
Pb:scint. = 8 mm:2 mm in T405	$3.6 \pm 1.3\%$	$3.4 \pm 1.2\%$
Pb:scint. = 8 mm:2 mm in T411	$3.0 \pm 1.1\%$	$1.2 \pm 0.4\%$
Pb:scint. = 10 mm:2 mm in T405	$3.5 \pm 1.2\%$	$0.5 \pm 0.2\%$
Pb:scint. = 10 mm:2 mm in T411	-	$1.2 \pm 0.4\%$
Pb:scint. = 12 mm:2 mm in T405	-	$1.6 \pm 0.5\%$
Pb:scint. = 14 mm:2 mm in T405	-	$1.0 \pm 0.3\%$
Pb:scint. = 16 mm:2 mm in T405	-	$3.0 \pm 1.0\%$
Pb:scint. = 16 mm:2 mm in T405	-	$0.5 \pm 0.7\%$

Table 5.5: The non-linearity estimated by f.

and b. t_{max} should be independent of configuretions and be a function as a energy. t_{max} in Fig. 5.16 is independent of the configurations as expected. t_{max} in Fig. 5.15 has a dependence on the energy as expected, respectively.

The normalization factors f is shown in Figs. 5.17, and 5.18. If f has a dependence on energy, the responce of the calorimeter to pions are not a linear function of the energy. We do not find any energy dependence of f as shown in Figs. 5.17. The f dose not depende on the calorimeter configurations in Fig. 5.18. This results indecates that the calorimeters have a good linearity for pion. The non-linearity estimated from the fitted f is shown in Table 5.5 and Fig. 5.11

configuration (Pb:scint. in mm) and energy	$b\,(\lambda_I^{-1})$	a	f (mip/Layer/GeV)
4:2 in T411 1 GeV	1.28 ± 0.03	1.11 ± 0.02	12.2 ± 0.2
4:2 in T411 2 GeV	1.34 ± 0.02	1.37 ± 0.02	12.1 ± 0.1
4:2 in T411 3 GeV	1.16 ± 0.02	1.39 ± 0.02	12.3 ± 0.1
4:2 in T411 4 GeV	1.08 ± 0.02	1.41 ± 0.02	12.2 ± 0.1
6:2 in T405 1 GeV	1.81 ± 0.07	1.31 ± 0.04	13.2 ± 0.2
6:2 in T405 2 GeV	1.49 ± 0.04	1.50 ± 0.03	12.6 ± 0.2
6:2 in T405 3 GeV	1.31 ± 0.03	1.51 ± 0.03	12.5 ± 0.2
6:2 in T405 4 GeV	1.05 ± 0.03	1.43 ± 0.03	12.5 ± 0.2
6:2 in T411 1 GeV	1.28 ± 0.04	1.15 ± 0.03	13.2 ± 0.2
6:2 in T411 2 GeV	1.31 ± 0.03	1.34 ± 0.03	12.6 ± 0.2
6:2 in T411 3 GeV	1.18 ± 0.02	1.39 ± 0.03	12.5 ± 0.2
6:2 in T411 4 GeV	1.12 ± 0.02	1.43 ± 0.03	12.5 ± 0.2
8:2 in T405 1 GeV	1.16 ± 0.06	1.12 ± 0.05	14.5 ± 0.3
8:2 in T405 2 GeV	1.03 ± 0.04	1.29 ± 0.04	15.1 ± 0.2
8:2 in T405 3 GeV	1.02 ± 0.03	1.36 ± 0.03	14.1 ± 0.2
8:2 in T405 4 GeV	1.10 ± 0.03	1.48 ± 0.03	13.8 ± 0.2
8:2 in T411 1 GeV	1.28 ± 0.05	1.15 ± 0.04	13.7 ± 0.3
8:2 in T411 2 GeV	1.34 ± 0.04	1.42 ± 0.04	13.5 ± 0.2
8:2 in T411 3 GeV	1.16 ± 0.03	1.42 ± 0.03	13.9 ± 0.2
8:2 in T411 4 GeV	1.10 ± 0.02	1.46 ± 0.03	13.7 ± 0.2

Table 5.6: Summary of the results of longitudinal shower profile for π's fit to Eq (5.1), part-I.

configuration (Pb:scint. in mm) and energy	$b\,(\lambda_I^{-1})$	a	f (mip/layer/GeV)
10:2 in T405 1 GeV	1.09 ± 0.05	1.13 ± 0.05	14.6 ± 0.3
10:2 in T405 2 GeV	0.90 ± 0.03	1.20 ± 0.04	14.5 ± 0.2
10:2 in T405 3 GeV	0.93 ± 0.02	1.32 ± 0.04	14.6 ± 0.2
10:2 in T405 4 GeV	0.91 ± 0.02	1.37 ± 0.03	14.4 ± 0.2
10:2 in T411 2 GeV	1.18 ± 0.04	1.35 ± 0.04	13.7 ± 0.2
10:2 in T411 3 GeV	1.05 ± 0.03	1.37 ± 0.04	13.6 ± 0.2
10:2 in T411 4 GeV	0.99 ± 0.02	1.40 ± 0.03	13.9 ± 0.2
12:2 in T405 1 GeV	1.52 ± 0.09	1.27 ± 0.07	14.5 ± 0.3
12:2 in T405 2 GeV	1.47 ± 0.05	1.57 ± 0.05	14.2 ± 0.3
12:2 in T405 3 GeV	1.34 ± 0.04	1.62 ± 0.05	14.3 ± 0.2
12:2 in T405 4 GeV	1.00 ± 0.03	1.43 ± 0.04	14.5 ± 0.2
14:2 in T405 1 GeV	1.32 ± 0.06	1.28 ± 0.06	13.6 ± 0.3
14:2 in T405 1 GeV	1.24 ± 0.04	1.47 ± 0.05	14.1 ± 0.3
14:2 in T405 1 GeV	1.10 ± 0.03	1.44 ± 0.05	14.8 ± 0.3
14:2 in T405 1 GeV	0.91 ± 0.03	1.36 ± 0.04	14.1 ± 0.2
16:2 in T405 1 GeV	1.35 ± 0.10	1.24 ± 0.08	13.6 ± 0.4
16:2 in T405 1 GeV	1.09 ± 0.06	1.30 ± 0.06	14.1 ± 0.3
16:2 in T405 1 GeV	0.86 ± 0.04	1.23 ± 0.05	14.8 ± 0.3
16:2 in T405 1 GeV	1.25 ± 0.04	1.64 ± 0.05	14.1 ± 0.3
16:2 in T411 1 GeV	1.66 ± 0.11	1.35 ± 0.09	13.4 ± 0.4
16:2 in T411 1 GeV	1.27 ± 0.06	1.43 ± 0.06	14.0 ± 0.3
16:2 in T411 1 GeV	1.17 ± 0.04	1.48 ± 0.05	13.8 ± 0.3
16:2 in T411 1 GeV	1.15 ± 0.03	1.55 ± 0.04	14.2 ± 0.3

Table 5.7: Summary of the results of longitudinal shower profile for π's fit to Eq (5.1), part-II.

configuration	t_{max} (λ_I)			
Pb:scint. (in mm)	1 GeV	2 GeV	3 GeV	4 GeV
4:2 in T411	0.08 ± 0.02	0.27 ± 0.02	0.34 ± 0.02	0.38 ± 0.02
6:2 in T405	0.17 ± 0.03	0.33 ± 0.03	0.38 ± 0.03	0.41 ± 0.03
6:2 in T411	0.11 ± 0.03	0.26 ± 0.02	0.33 ± 0.02	0.39 ± 0.03
8:2 in T405	0.10 ± 0.04	0.28 ± 0.04	0.36 ± 0.04	0.44 ± 0.03
8:2 in T411	0.12 ± 0.03	0.31 ± 0.03	0.37 ± 0.03	0.42 ± 0.03
10:2 in T405	0.13 ± 0.04	0.22 ± 0.04	0.34 ± 0.04	0.40 ± 0.04
10:2 in T411	no data	0.29 ± 0.04	0.35 ± 0.04	0.40 ± 0.03
12:2 in T405	0.17 ± 0.05	0.39 ± 0.04	0.46 ± 0.04	0.42 ± 0.04
14:2 in T405	0.21 ± 0.05	0.38 ± 0.04	0.40 ± 0.04	0.39 ± 0.04
16:2 in T405	0.17 ± 0.06	0.27 ± 0.06	0.26 ± 0.06	0.51 ± 0.04
16:2 in T411	0.21 ± 0.06	0.34 ± 0.05	0.41 ± 0.05	0.48 ± 0.04

Table 5.8: t_{max} calculated from Eq. (2.6) for π's.

5.6 Energy resolution for electrons

The pulse height distributions for electrons are shown in Fig. 5.2. Energy resolution is given by σ/E from a fit to a Gaussian ($f(x) = \exp(-(x-\mathrm{E})^2/2\sigma^2)$). Energy resolution $\sigma/\sqrt{\mathrm{E}}$ for electrons in each calorimeter configuration is shown in Figs. 5.19 and 5.20.

In Eq. (2.1), $\sigma_{constant}$ and σ_{noise} are negligible, because the $\sigma_{stocastic}$ is larger for such a low incident energy. As shown in Fig. 5.19 and Table 5.9, $\sigma_{stocastic}$ is dominant in the energy resolution for electrons. The average energy resolutions for electorns are

- $(15.2 \pm 0.5)\%/\sqrt{\mathrm{E}}$ (for T411 d = 4 mm)
- $(19.8 \pm 0.5)\%/\sqrt{\mathrm{E}}$ (for T405 d = 6 mm)
- $(19.7 \pm 0.5)\%/\sqrt{\mathrm{E}}$ (for T411 d = 6 mm)

configuration	$\sigma/\sqrt{\mathrm{E}}$ (%)				
Pb:scint. (in mm)	1 GeV	2 GeV	3 GeV	4 GeV	average
4:2 in T411	15.1 ± 1.0	15.5 ± 1.0	15.1 ± 1.0	15.2 ± 1.0	15.2 ± 0.5
6:2 in T405	19.2 ± 1.0	19.9 ± 1.0	21.1 ± 1.0	19.8 ± 1.0	19.8 ± 0.5
6:2 in T411	19.3 ± 1.0	21.5 ± 1.0	19.3 ± 1.0	19.7 ± 1.1	19.7 ± 0.5
8:2 in T405	22.9 ± 1.0	23.5 ± 1.0	23.5 ± 1.0	23.2 ± 1.1	23.3 ± 0.5
8:2 in T411	22.9 ± 1.0	22.8 ± 1.0	22.8 ± 1.0	22.5 ± 1.1	22.7 ± 0.5
10:2 in T405	25.3 ± 1.1	26.3 ± 1.1	26.4 ± 1.1	26.6 ± 1.1	26.1 ± 0.5
10:2 in T411	-	26.6 ± 1.1	26.8 ± 1.1	26.3 ± 1.1	26.5 ± 0.6
12:2 in T405	27.1 ± 1.1	29.6 ± 1.1	29.6 ± 1.1	29.6 ± 1.1	29.0 ± 0.5
14:2 in T405	31.0 ± 1.1	32.5 ± 1.1	32.5 ± 1.1	33.1 ± 1.1	32.3 ± 0.5
16:2 in T405	34.1 ± 1.1	35.4 ± 1.1	35.1 ± 1.1	33.7 ± 1.1	34.6 ± 0.6
16:2 in T411	33.2 ± 1.2	34.7 ± 1.1	34.6 ± 1.1	36.1 ± 1.2	34.7 ± 0.6

Table 5.9: The energy resolution for electrons, $\sigma/\sqrt{\mathrm{E}}$.

- $(23.3 \pm 0.5)\%/\sqrt{\mathrm{E}}$ (for T405 d = 8 mm)
- $(22.7 \pm 0.5)\%/\sqrt{\mathrm{E}}$ (for T411 d = 8 mm)
- $(26.1 \pm 0.5)\%/\sqrt{\mathrm{E}}$ (for T405 d = 10 mm)
- $(26.5 \pm 0.6)\%/\sqrt{\mathrm{E}}$ (for T411 d = 10 mm)
- $(29.0 \pm 0.5)\%/\sqrt{\mathrm{E}}$ (for T405 d = 12 mm)
- $(32.3 \pm 0.5)\%/\sqrt{\mathrm{E}}$ (for T405 d = 14 mm)
- $(34.6 \pm 0.6)\%/\sqrt{\mathrm{E}}$ (for T405 d = 16 mm)
- $(34.7 \pm 0.6)\%/\sqrt{\mathrm{E}}$ (for T411 d = 16 mm)

as shown in Table 5.9.

Energy resolution $\sigma/\sqrt{\mathrm{E}}$ for electron vs. Pb thickness par layer is shown in Fig. 5.20. As shown in Fig. 5.20, we fitted the plot of σ/E vs. Pb thickness to the following equation:

$$\sigma_{stocastic} = \sqrt{\sigma_{intrinsic}^2 + d \times (\sigma_{sample}^2 + \sigma_{photostat}^2)}, \tag{5.2}$$

where d is the thickness of Pb plate. The fitted result is $\sigma_{intrinsic} = 0.0^{+1.4}_{-0.0}\%$, and $\sqrt{\sigma_{sample}^2 + \sigma_{photostat}^2} = 8.2 \pm 0.1\%$, shown in Table 5.11. For EM shower, the $\sigma_{intrinsic}$ should be less than 1% and as expected. Average light yield of tile/fiber systems (in Chapter 3) is 1.67 pes/mip/tile. We estimate the $\sigma_{photostat} = 3.8 \pm 0.1\%$ from the average light yield which results in σ_{sample} of 7.5±0.1. Pb plate thickness should be less equal 4mm, for JLC EM calorimeter in order to acheve the requirments.

5.7 Energy resolution for pions

The pulse height distributions for π's are shown in Figs. 5.2. Energy resolution σ/E is obtained from a fit to a Gaussian as well as for electrons. $\sigma/\sqrt{\mathrm{E}}$ for π's for each calorimeter configurations is shown in Figs. 5.21 and 5.22.

In Eq. (2.1), $\sigma_{constant}$ and σ_{noise} are negligible because $\sigma_{stocastic}$ is larger for such a low incident energy. As shown in Fig. 5.21 and Table 5.7, $\sigma_{stocastic}$ is dominant in the energy resolution for π's, respectively. The average energy resolutions (2-4 GeV) for π's are

configuration	$\sigma/\sqrt{\mathrm{E}}$ (%)				
Pb:scint. (in mm)	1 GeV	2 GeV	3 GeV	4 GeV	average 2-4 GeV
4:2 in T411	30.5 ± 1.1	34.2 ± 1.1	33.1 ± 1.1	32.9 ± 1.1	33.4 ± 0.6
6:2 in T405	34.9 ± 1.2	38.5 ± 1.1	38.9 ± 1.1	39.3 ± 1.1	38.9 ± 0.7
6:2 in T411	32.6 ± 1.1	35.9 ± 1.1	36.3 ± 1.2	34.6 ± 1.3	35.6 ± 0.7
8:2 in T405	35.3 ± 1.1	39.5 ± 1.1	39.1 ± 1.1	41.2 ± 1.2	39.6 ± 0.6
8:2 in T411	34.8 ± 1.1	39.4 ± 1.2	41.4 ± 1.2	39.4 ± 1.2	39.7 ± 0.7
10:2 in T405	36.0 ± 1.1	42.4 ± 1.2	43.0 ± 1.2	42.9 ± 1.2	42.6 ± 0.7
10:2 in T411	-	43.0 ± 1.3	43.7 ± 1.3	43.5 ± 1.2	43.4 ± 0.7
12:2 in T405	39.6 ± 1.2	45.7 ± 1.2	46.4 ± 1.2	46.5 ± 1.2	46.2 ± 0.7
14:2 in T405	39.8 ± 1.2	46.2 ± 1.2	47.2 ± 1.2	49.0 ± 1.2	47.5 ± 0.7
16:2 in T405	43.5 ± 1.3	51.9 ± 1.3	51.5 ± 1.3	52.8 ± 1.3	51.7 ± 0.7
16:2 in T411	43.3 ± 1.4	48.7 ± 1.4	51.7 ± 1.3	52.0 ± 1.4	50.8 ± 0.8

Table 5.10: The energy resolution $\sigma/\sqrt{\mathrm{E}}$ for π's.

- $(33.4 \pm 0.6)\%/\sqrt{\mathrm{E}}$ (for T411 d = 4 mm)
- $(38.9 \pm 0.7)\%/\sqrt{\mathrm{E}}$ (for T405 d = 6 mm)
- $(35.6 \pm 0.7)\%/\sqrt{\mathrm{E}}$ (for T411 d = 6 mm)
- $(39.6 \pm 0.6)\%/\sqrt{\mathrm{E}}$ (for T405 d = 8 mm)
- $(39.7 \pm 0.7)\%/\sqrt{\mathrm{E}}$ (for T411 d = 8 mm)
- $(42.6 \pm 0.7)\%/\sqrt{\mathrm{E}}$ (for T405 d = 10 mm)
- $(43.4 \pm 0.7)\%/\sqrt{\mathrm{E}}$ (for T411 d = 10 mm)
- $(46.2 \pm 0.7)\%/\sqrt{\mathrm{E}}$ (for T405 d = 12 mm)
- $(47.5 \pm 0.7)\%/\sqrt{\mathrm{E}}$ (for T405 d = 14 mm)
- $(51.7 \pm 0.7)\%/\sqrt{\mathrm{E}}$ (for T405 d = 16 mm)

	$\sigma_{intrinsic}$	σ_{sample}
for electrons	$0.00^{+1.4}_{-0.00}\%$	$7.5 \pm 0.1\%\ \mathrm{mm}^{-1/2}$
for π's 2-4 GeV	$25.1 \pm 0.9\%$	$10.3 \pm 0.2\%\ \mathrm{mm}^{-1/2}$
for π's 1 GeV	$25.6 \pm 1.3\%$	$7.6 \pm 0.4\%\ \mathrm{mm}^{-1/2}$

Table 5.11: Over all fit results of the energy resolution to Eq. (5.2)

- $(50.8 \pm 0.8)\%/\sqrt{\mathrm{E}}$ (for T411 d = 16 mm)

as shown in Table 5.7.

In order to acheive the requirment for the JLC hadron calorimeter in energy resolution, thickness of Pb plate should be less than 8 mm for 2 mm plastic scintilletor.

Energy resolution $\sigma/\sqrt{\mathrm{E}}$ for π's vs. Pb thickness par layer is shown in Fig. 5.22. As shown in Fig. 5.22, we fitted plots of $\sigma/\sqrt{\mathrm{E}}$ vs. Pb thickness to Eq. (5.2) except for 1 GeV and 1 GeV. The fitted results are $\sigma_{intrinsic}$ = 25.1$\pm$ 0.9% and $\sqrt{\sigma^2_{sample} + \sigma^2_{photostat}}$ = 11.1 $\pm$ 0.2% except for 1 GeV, and $\sigma_{intrinsic}$ = 25.6 $\pm$ 1.3%, and $\sqrt{\sigma^2_{sample} + \sigma^2_{photostat}}$ = 8.5 $\pm$ 0.4%, for 1 GeV, as listed in Table 5.11 and Fig. 5.22. For the hadron shower, $\sigma_{intrinsic}$ is expected to be about 20% $\sim$ 30% for Pb absorber and consistent with the data. As $\sigma_{photostat}$ is estimated to be 3.8 $\pm$0.1% in the last section, σ_{sample} except for 1 GeV and 1 GeV are 10.3 $\pm$ 0.2% and 7.6 $\pm$ 0.4%.

5.8 Compensation ratio e/π

The mean of thepulse height distribution is obtained by fitting it to a gaussian. Figures 5.23, 5.24, 5.25, and 5.26 show the mean pulse height for the each calorimeter

calorimeter configuration	for electrons	for π's
Pb:scint. = 4 mm:2 mm in T411	$1.2 \pm 0.4\%$	$0.9 \pm 0.3\%$
Pb:scint. = 6 mm:2 mm in T405	$1.1 \pm 0.4\%$	$1.8 \pm 0.6\%$
Pb:scint. = 6 mm:2 mm in T411	$1.1 \pm 0.4\%$	$1.1 \pm 0.4\%$
Pb:scint. = 8 mm:2 mm in T405	$2.2 \pm 0.7\%$	$1.3 \pm 0.5\%$
Pb:scint. = 8 mm:2 mm in T411	$2.7 \pm 1.0\%$	$1.0 \pm 0.3\%$
Pb:scint. = 10 mm:2 mm in T405	$2.7 \pm 1.0\%$	$1.0 \pm 0.4\%$
Pb:scint. = 10 mm:2 mm in T411	$1.1 \pm 0.5\%$	$1.1 \pm 0.5\%$
Pb:scint. = 12 mm:2 mm in T405	$2.8 \pm 1.0\%$	$2.3 \pm 0.8\%$
Pb:scint. = 14 mm:2 mm in T405	$2.8 \pm 1.0\%$	$2.8 \pm 1.0\%$
Pb:scint. = 16 mm:2 mm in T405	$3.3 \pm 1.2\%$	$3.7 \pm 1.3\%$
Pb:scint. = 16 mm:2 mm in T405	$1.6 \pm 0.6\%$	$3.5 \pm 1.3\%$

Table 5.12: The non-linearity estimated from pulse height.

configurations and energies for electrons and π's.

The pulse height/energy is plotted against Pb thickness in Figs. 5.23 and 5.24. The pulse height/energy is plotted against the energy in Fig. 5.25 and 5.26. It is independent of energy, that is, the pulse height mean is a linear function of the energy as shown in Figs. 5.25 and 5.26. The pulse height has a $1/d$ dependence as shown in Figs. 5.23 and 5.24. Non-linearity is defined by the rms variation of the pulse height/energy for each configuration and shown in Fig. 5.27 and listed in Table. 5.12. Non-linearities for electorns and π's in all the calorimeter configurations are less than 4%. It is consistent with the result using f (in Table 5.5), as shown in Fig. 5.28.

e/π is plotted against the beam energy and the absorber thickness in Figs. 5.29 and 5.30, respectively. As shown in Fig. 5.30, e/π decreases with the absorber thickness d and is one around $d = 8{\sim}10$ mm. The compensation was found to be acheived with the ratio of the scintillator thickness to the Pb thickness of 4$\sim$5 as expected.

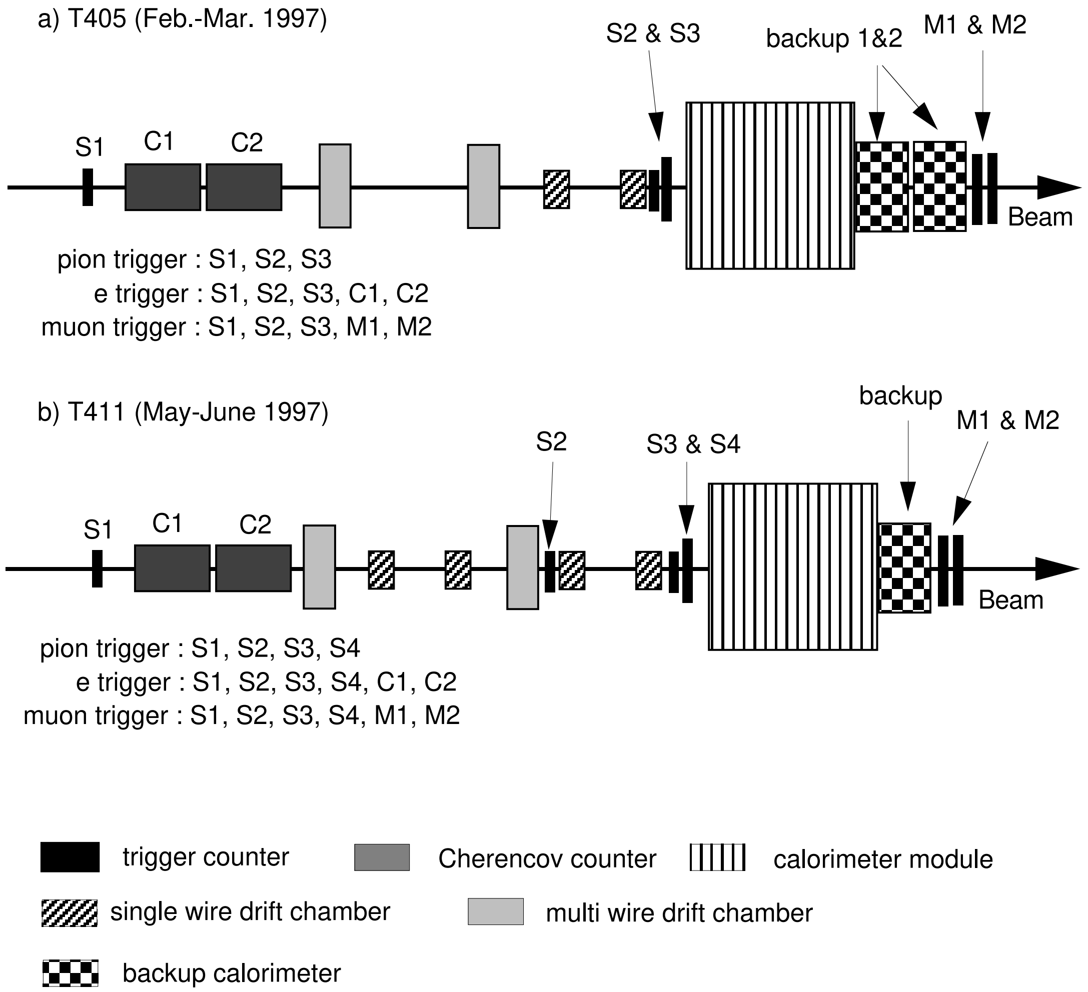

Figure 5.1: Schiematic views of the setups of the beam test. a) and b) are T405 and T411 respectively.

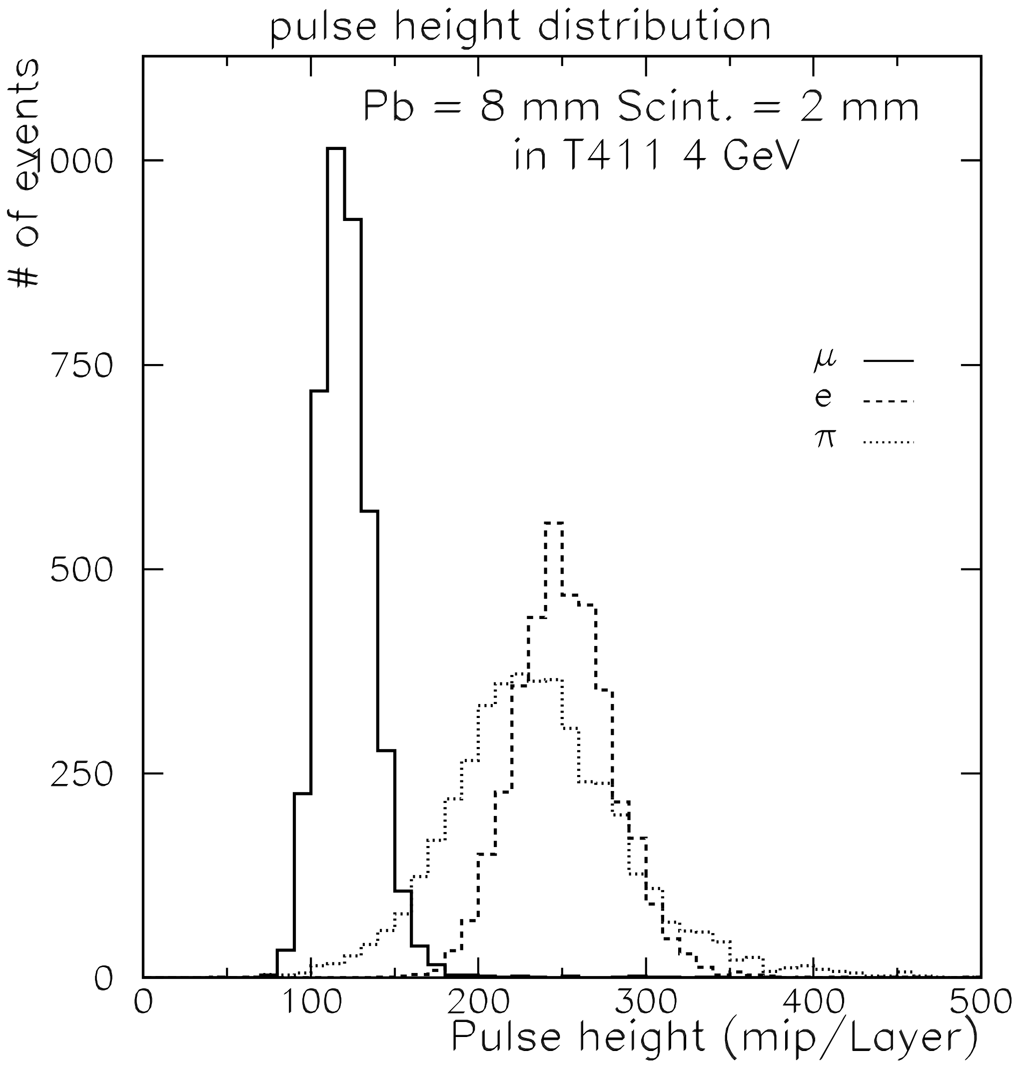

Figure 5.2: Typical pulse hight distribution of the configuration Pb= 8 mm Scint.= 2 mm for 4 GeV electrons, μ's, and π's.

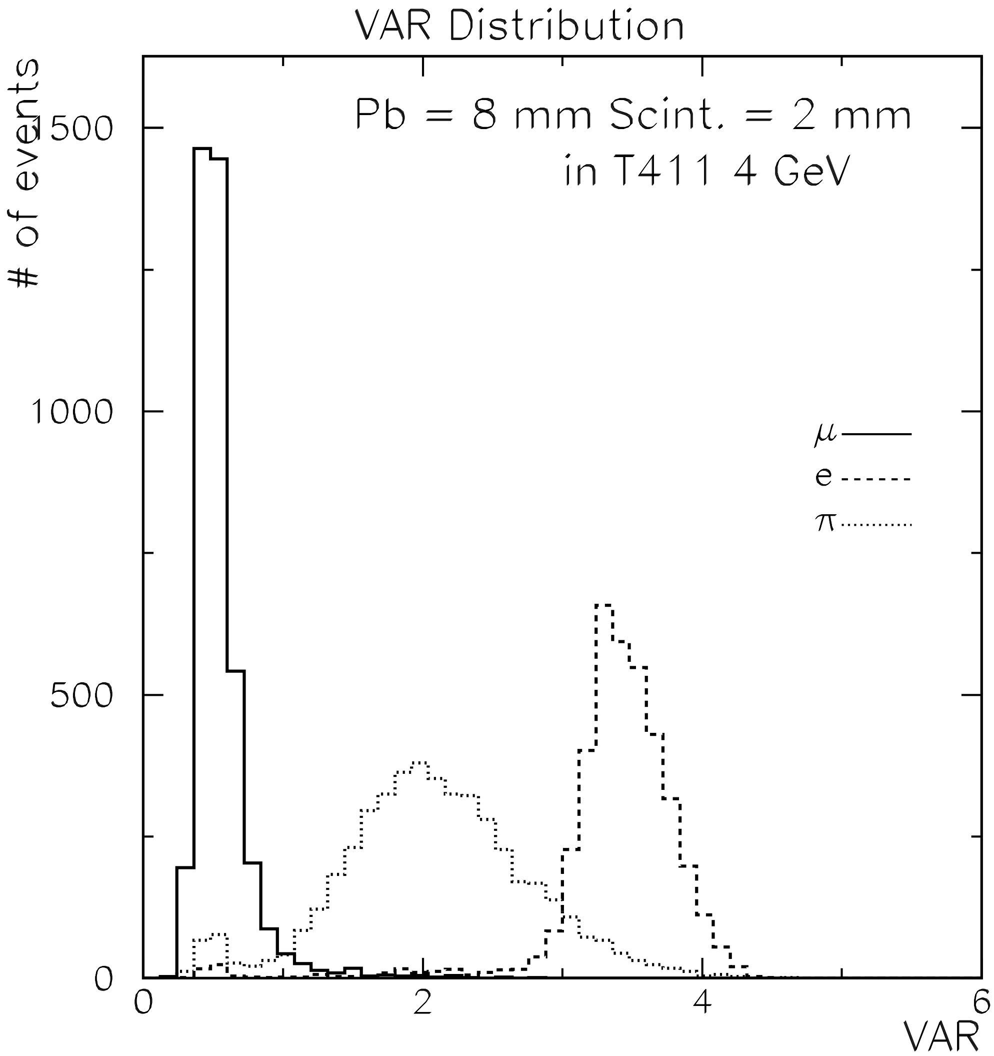

Figure 5.3: Typical the quantity VAR distribution of the configuration Pb = 8 mm Scint. = 2 mm for 4 GeV electrons, μ's, and π's.

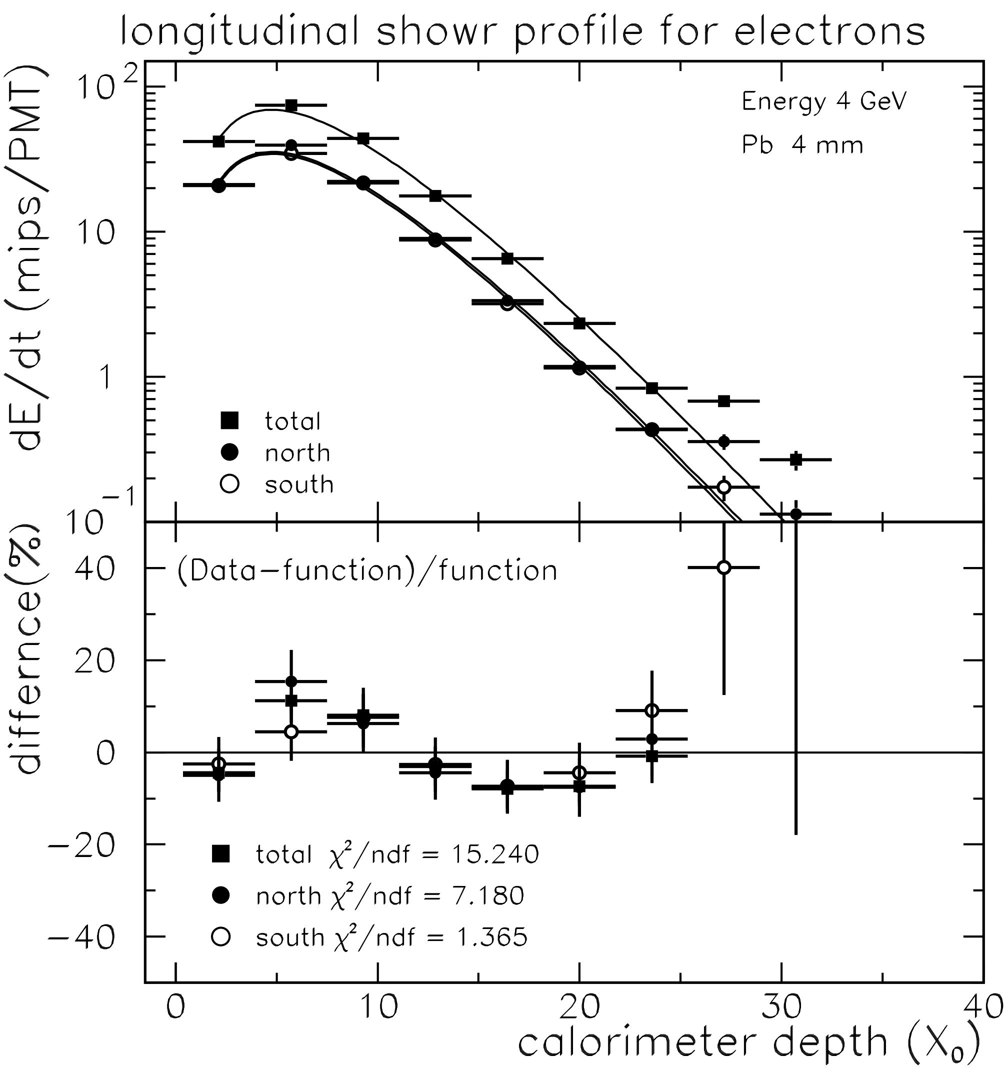

Figure 5.4: The electron longitudinal shower profile for the configration Pb : 4 mm Scintillator : 2 mm. The lines in the figure are fitting results.

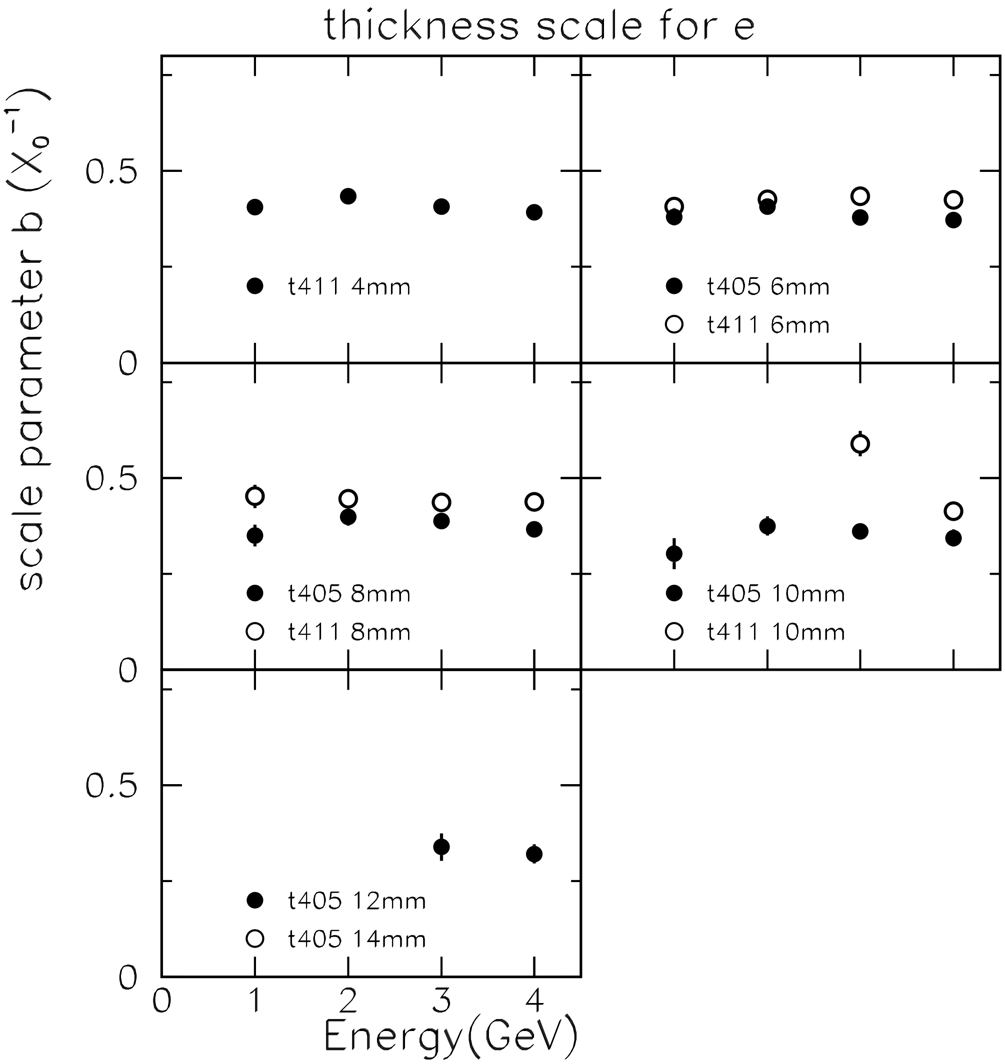

Figure 5.5: Fitted parameter b vs. energy for electrons.

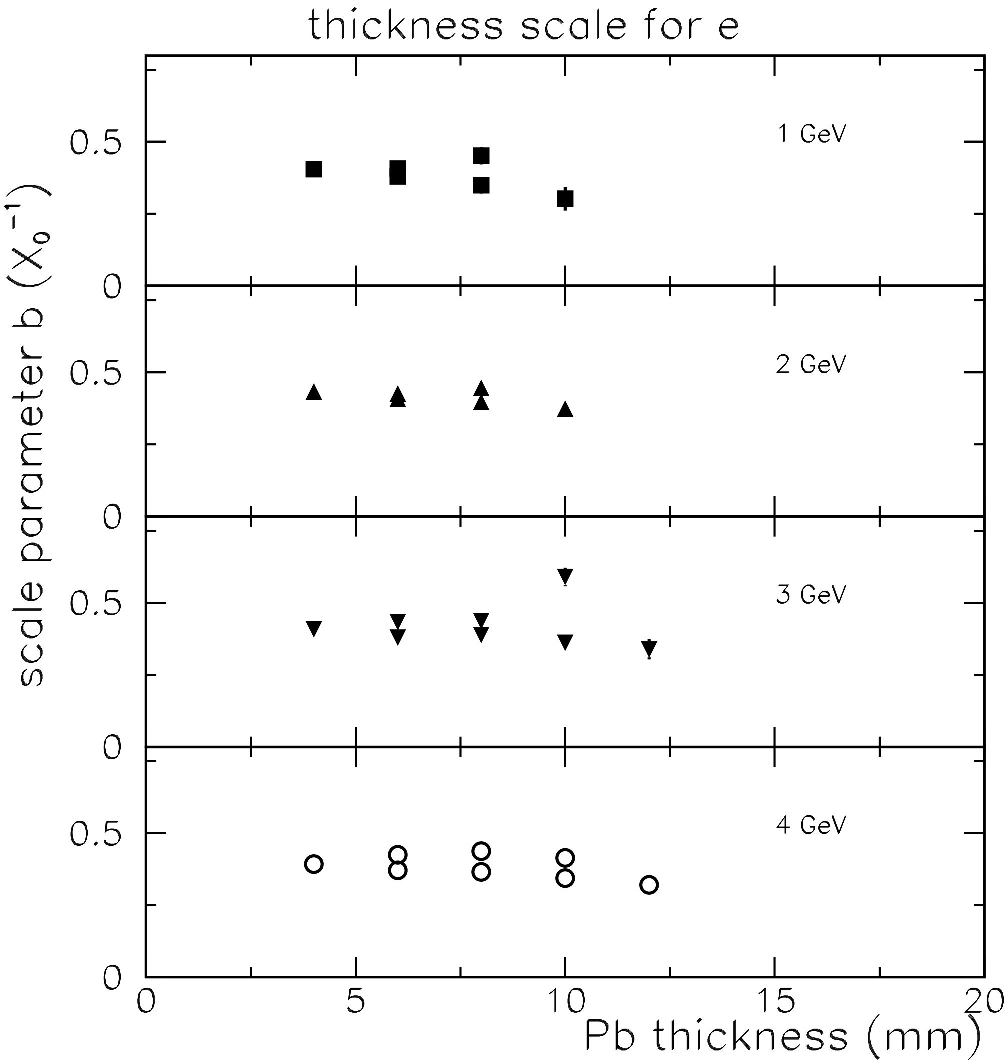

Figure 5.6: Fitted parameter b vs. Pb thickness for electrons.

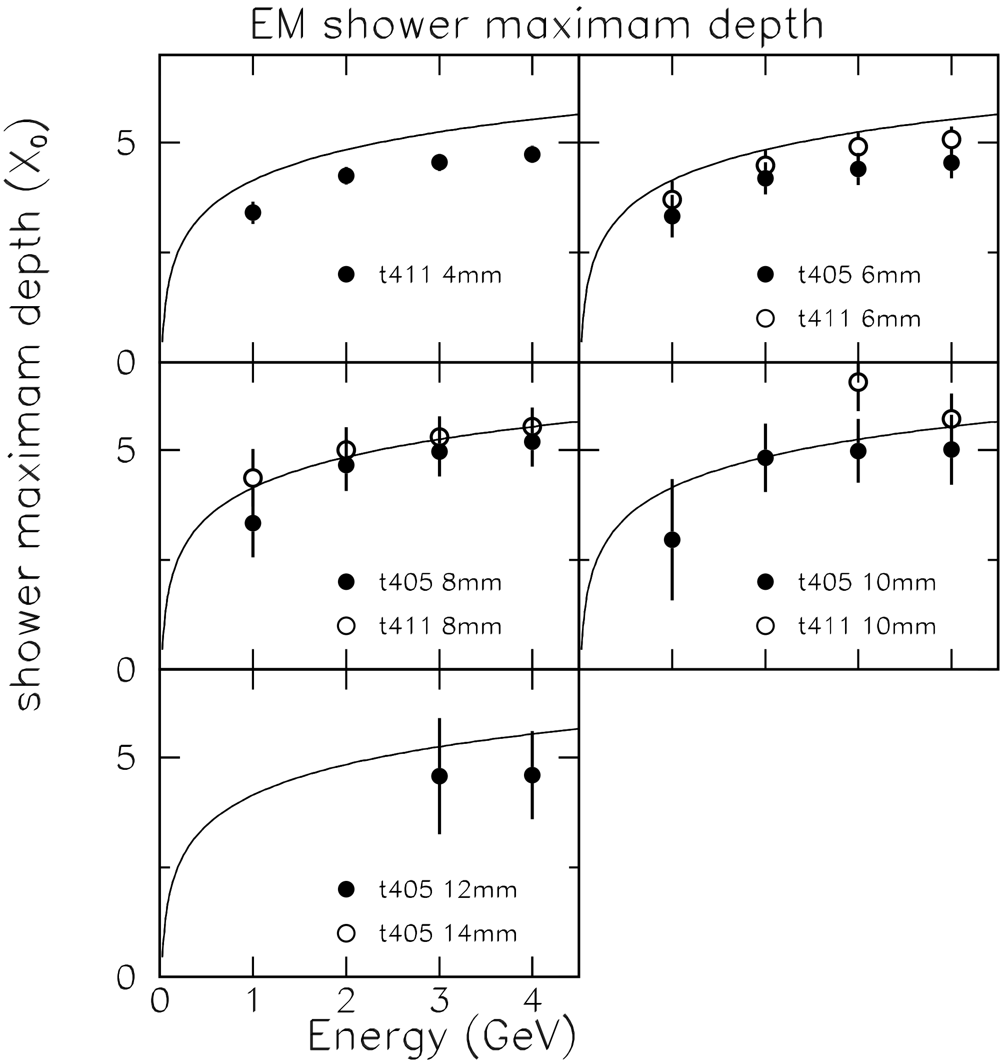

Figure 5.7: The depth of shower maximam vs. energy for electrons. Solid curves are the calculation from Eq. (2.7).

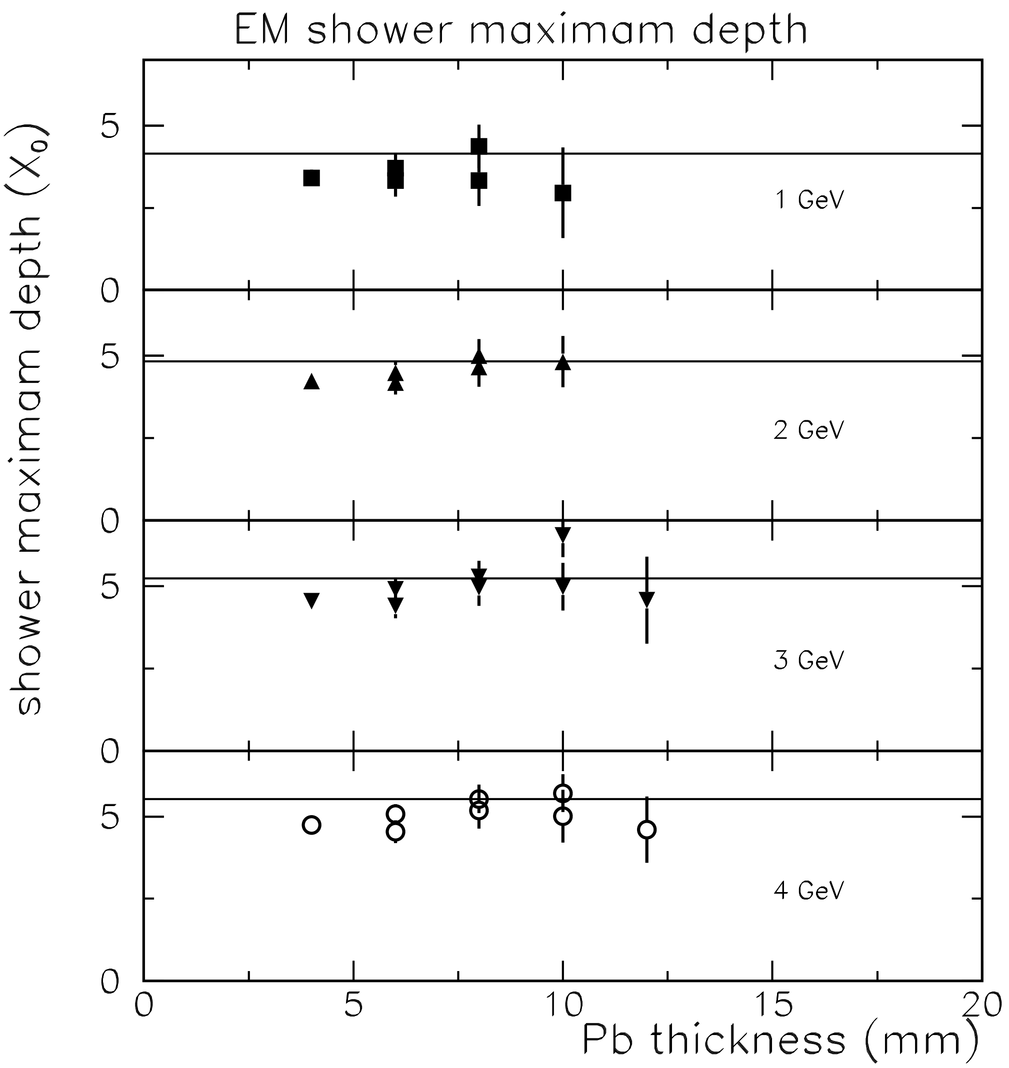

Figure 5.8: The depth of shower maxmam vs. Pb thickness for electrons. Lines shown in the figures are the calcuration from Eq. (2.7).

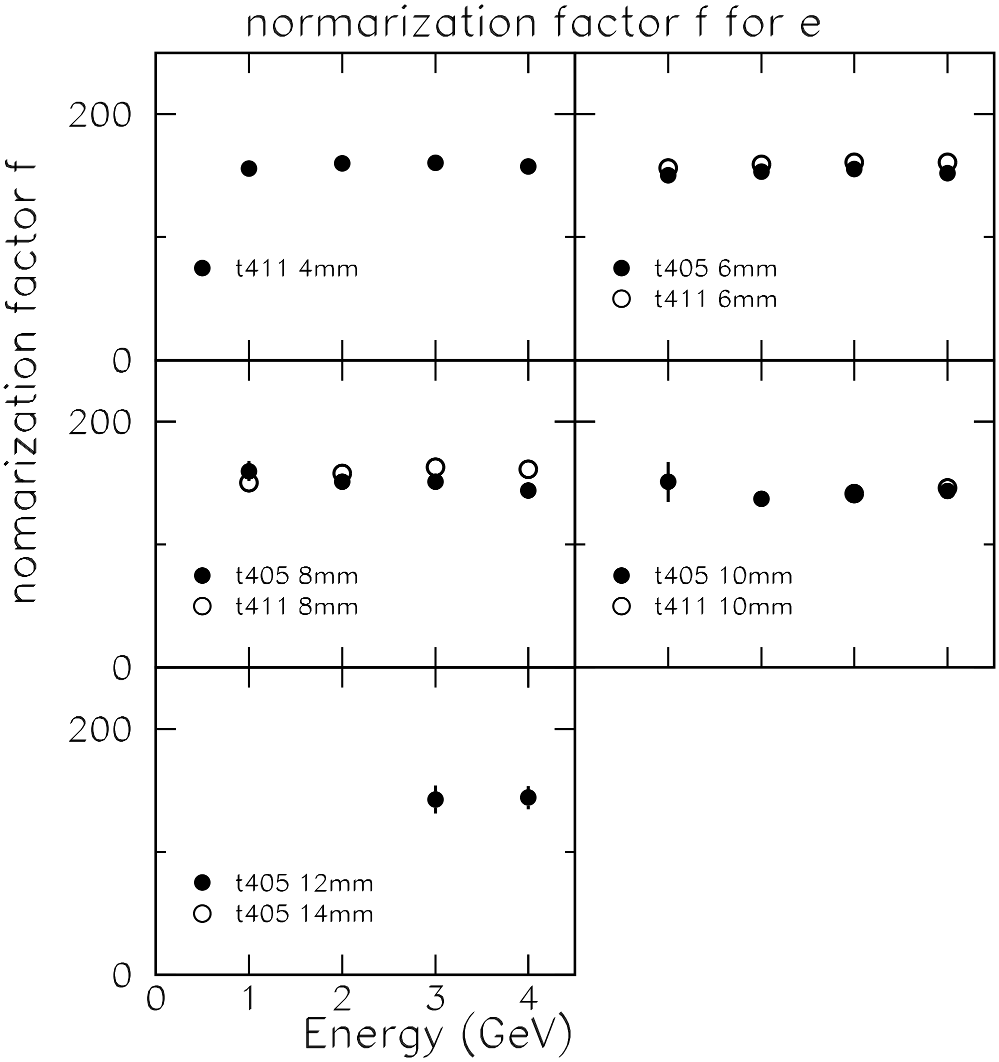

Figure 5.9: The normarization factor f vs. energy for electrons.

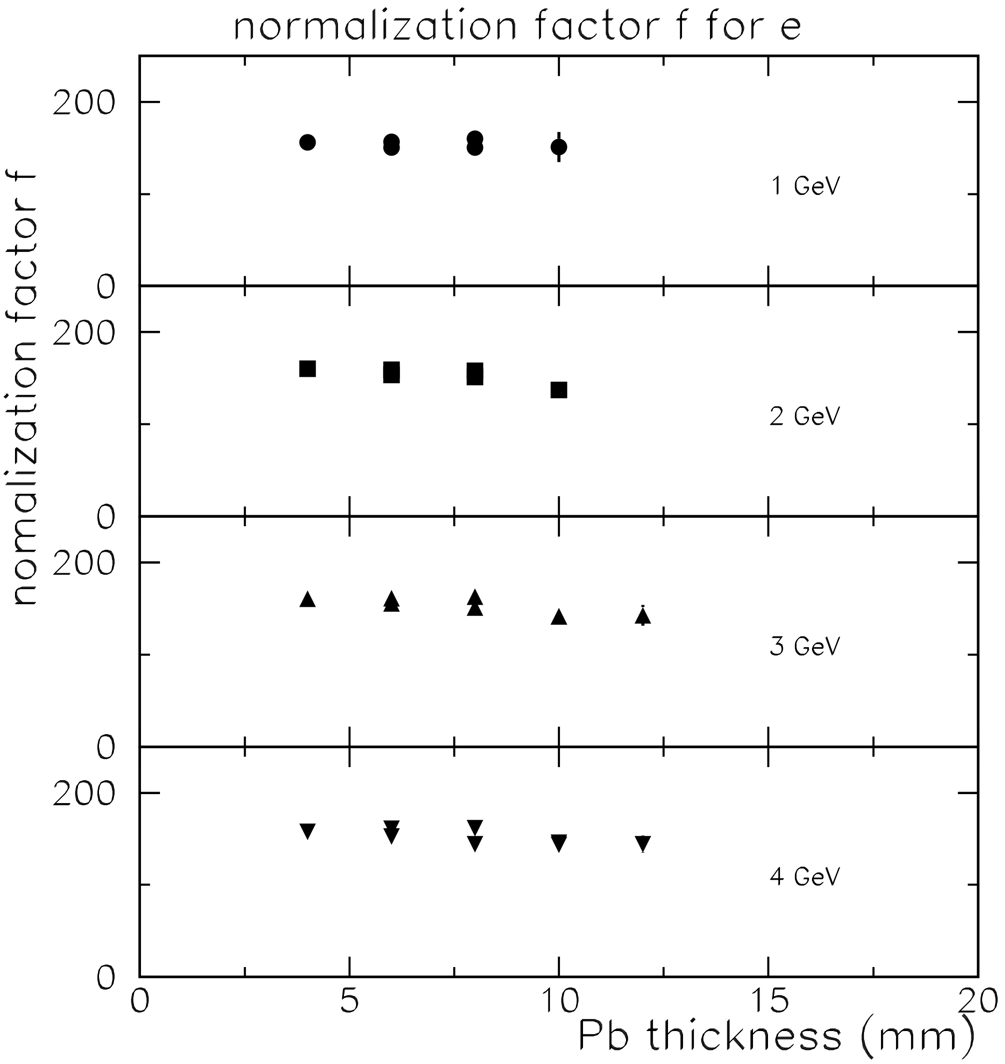

Figure 5.10: The normarization factor f vs. Pb thickness for electrons.

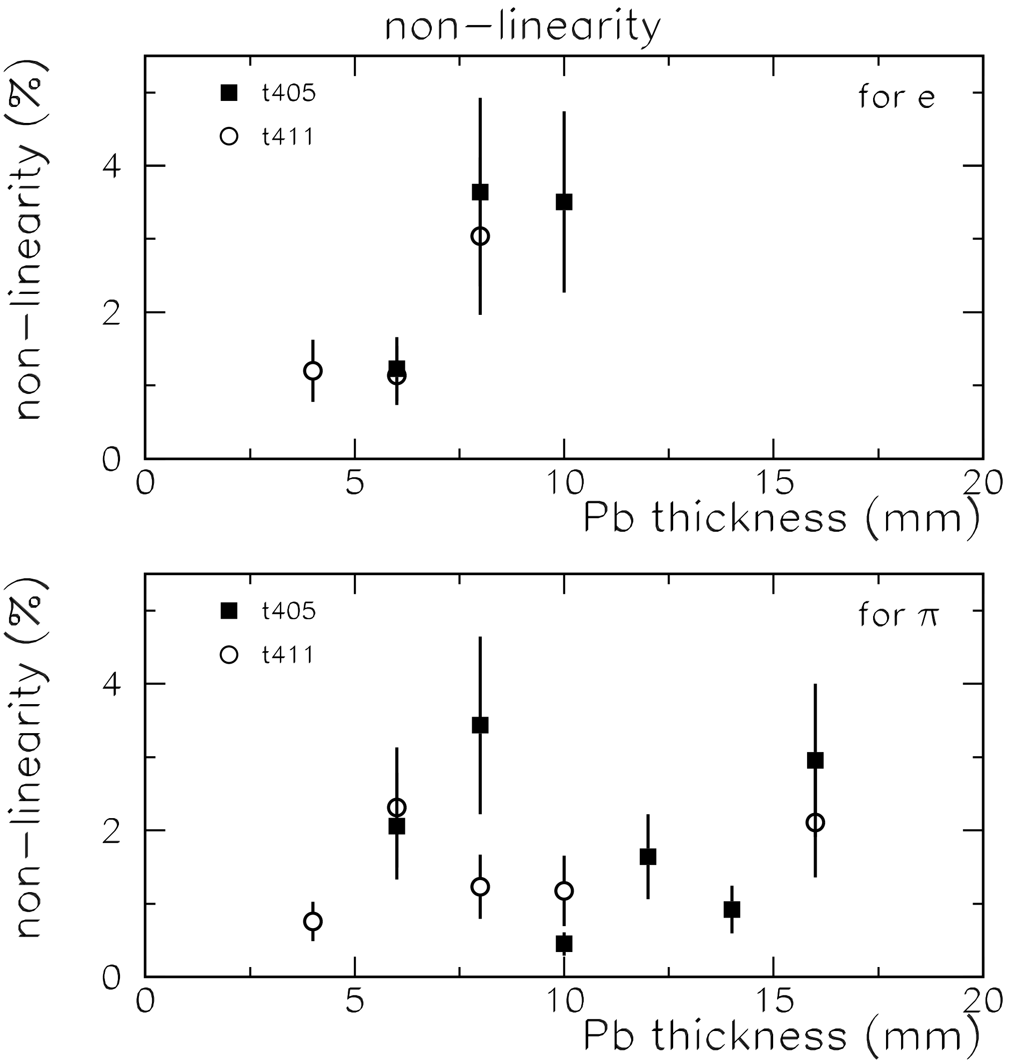

Figure 5.11: The non-linearity estimated from f.

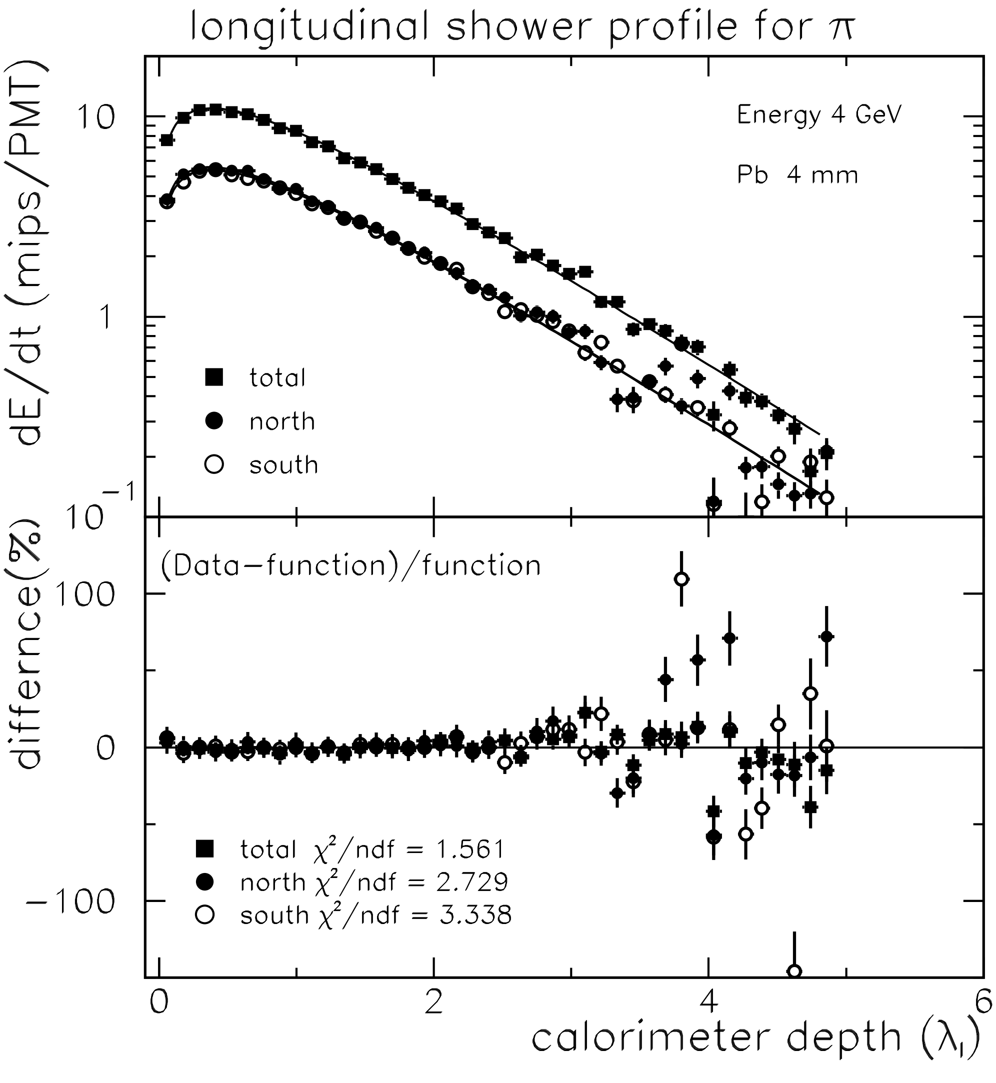

Figure 5.12: The pion longitudinal shower profile for the configration Pb : 4 mm Scintillator : 2 mm. The lines in the figure are fitting results.

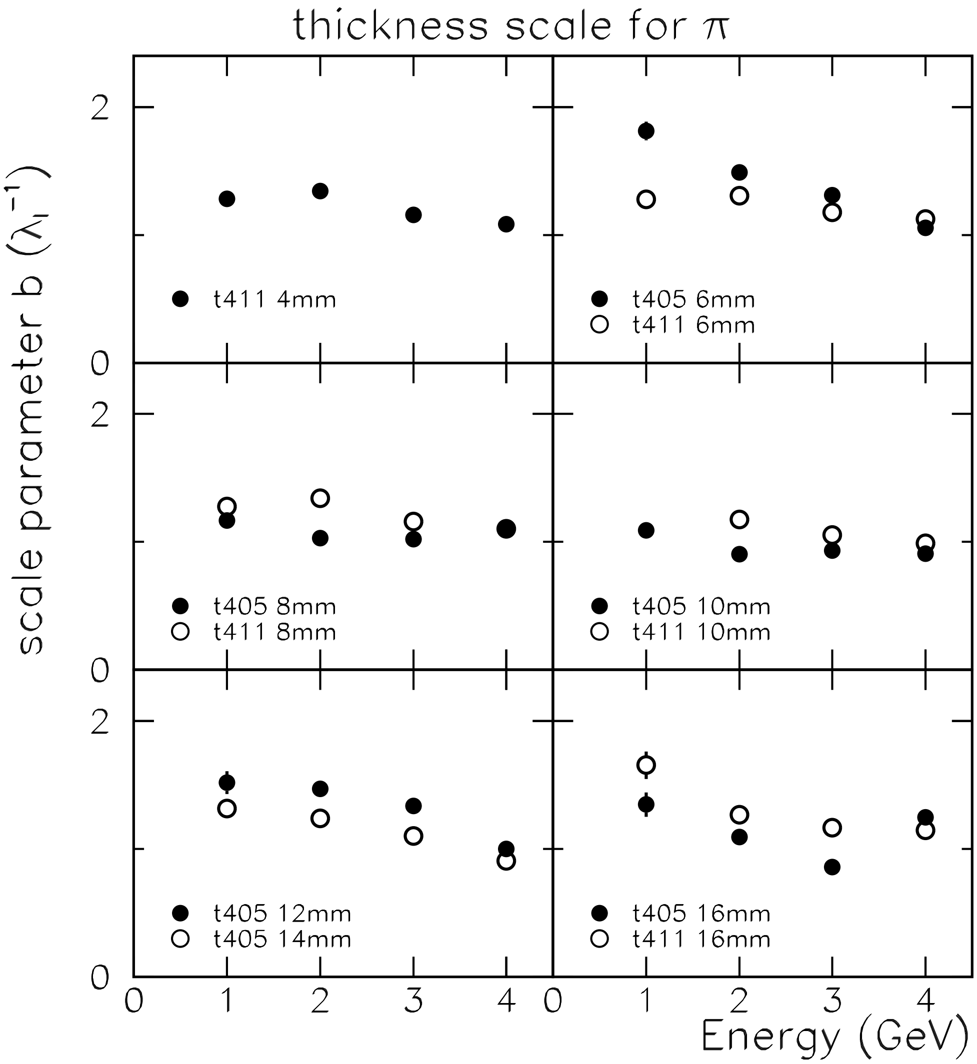

Figure 5.13: Fitted parameter b vs. energy for π.

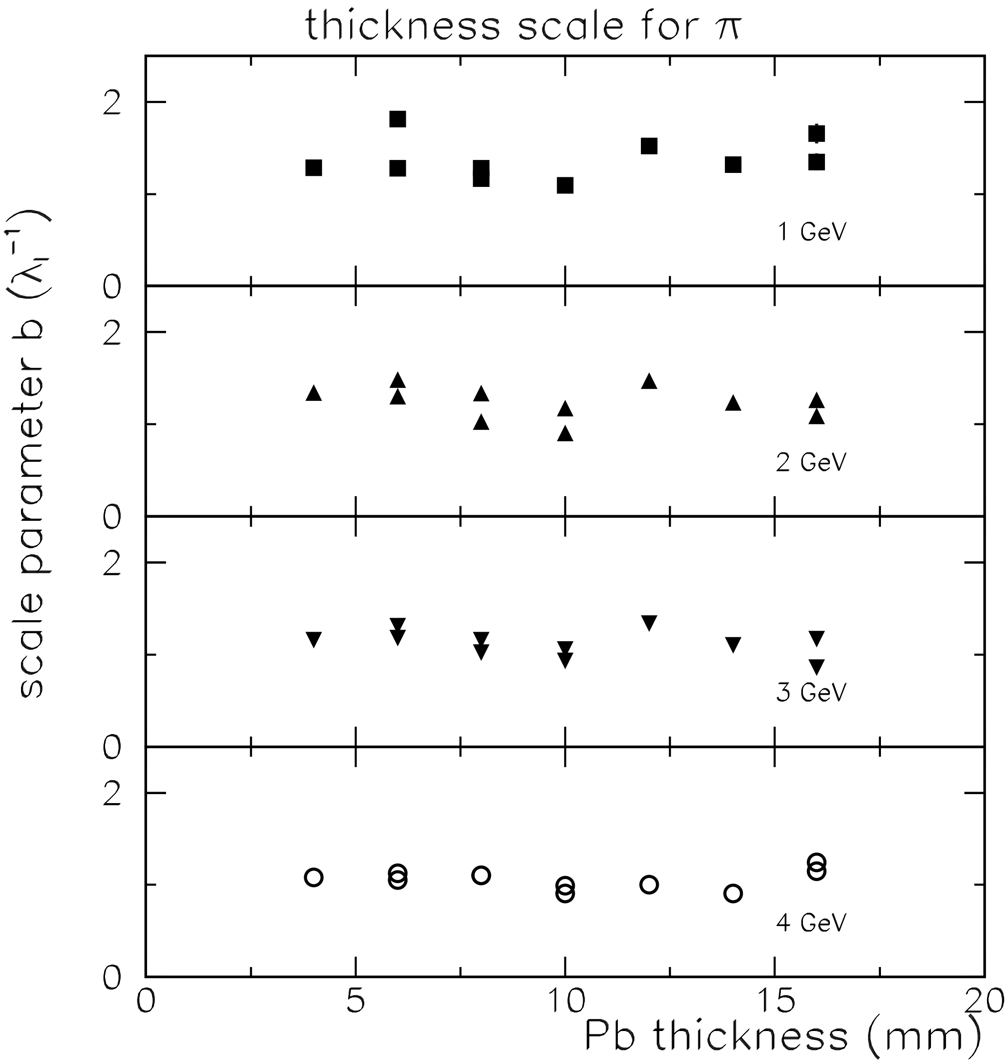

Figure 5.14: Fitted parameter b vs. Pb thickness for π.

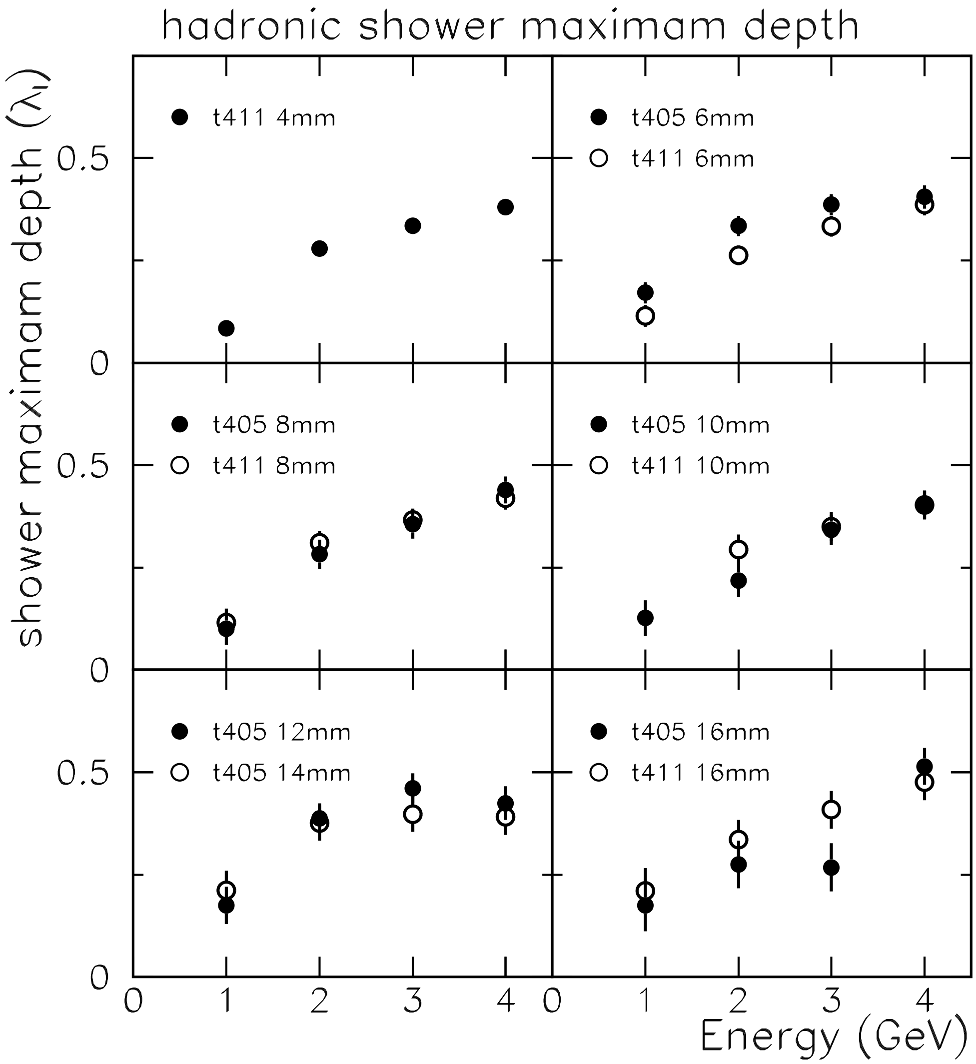

Figure 5.15: The depth of shower maximam vs. energy for π's.

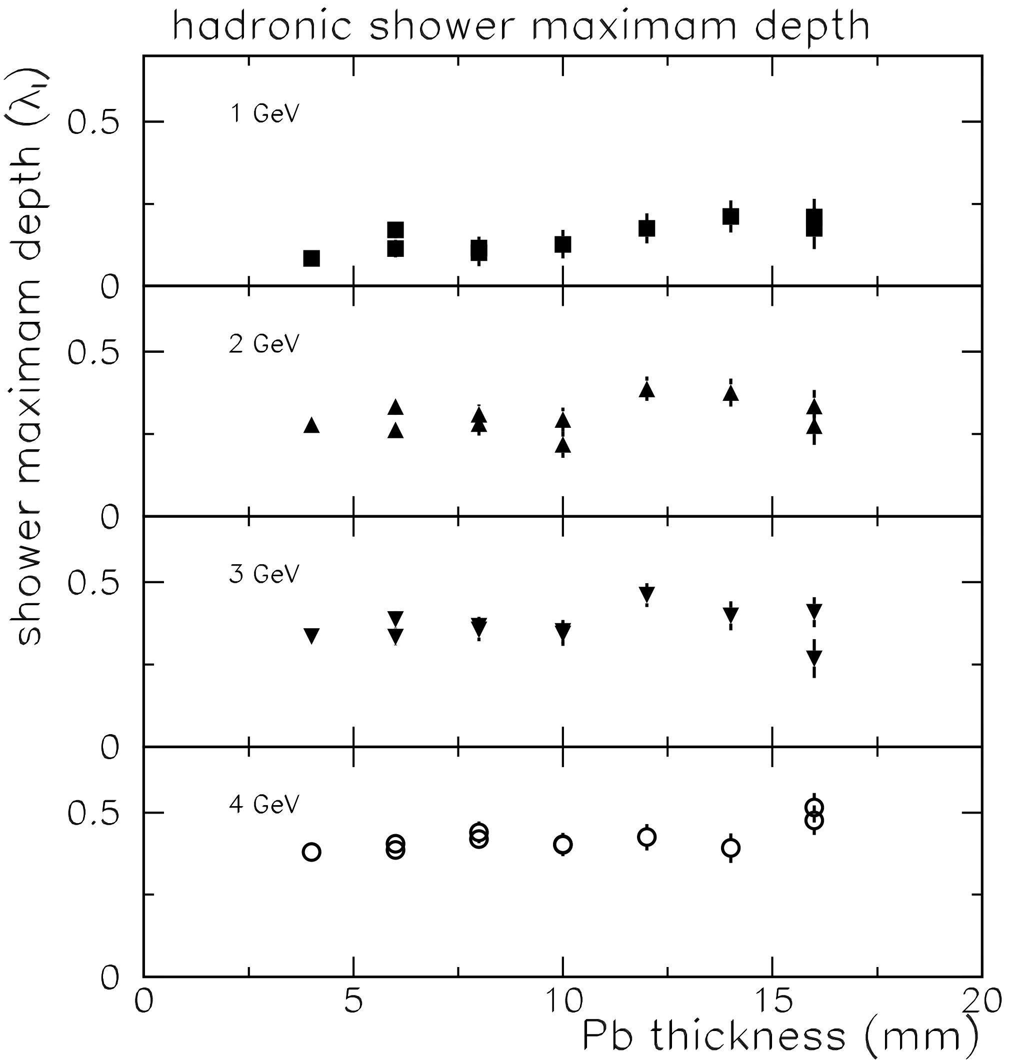

Figure 5.16: The depth of shower maximam vs. Pb thickness for π.

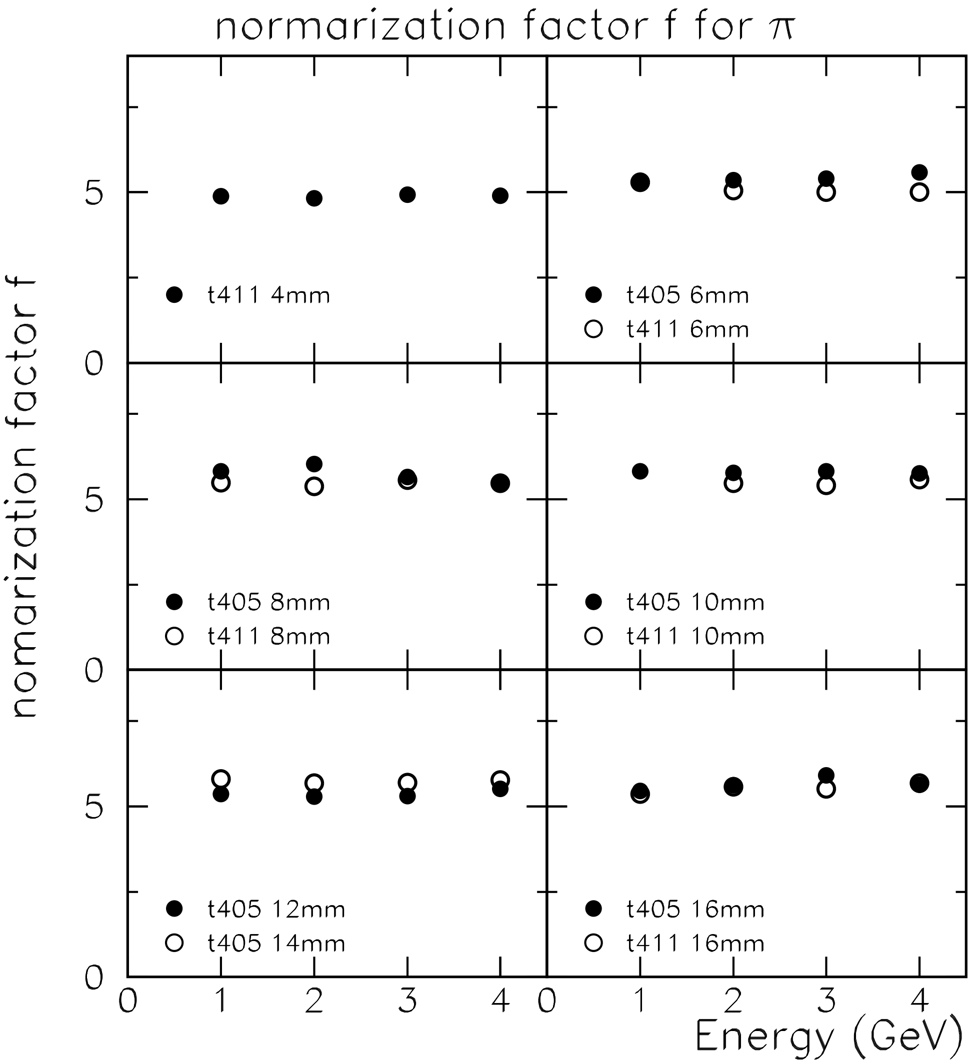

Figure 5.17: The normarization factor f vs. energy for π.

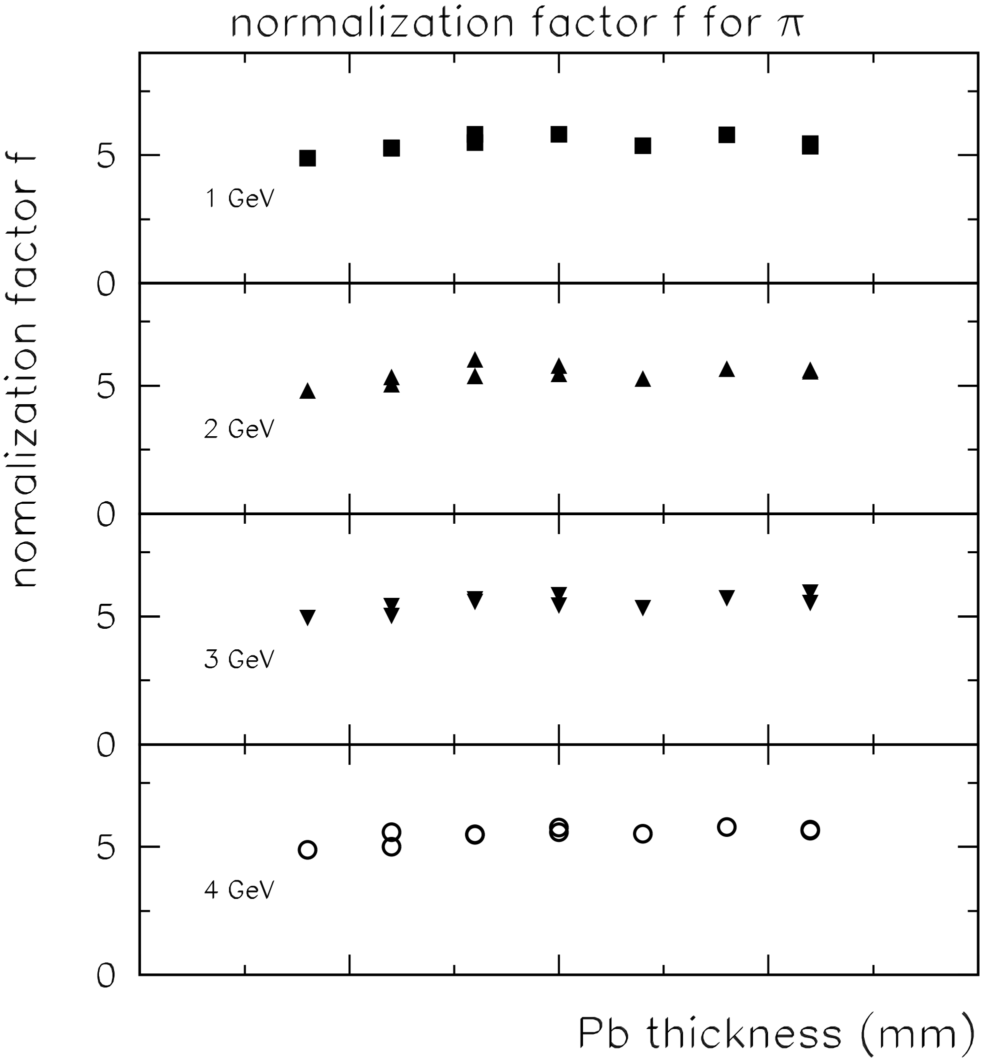

Figure 5.18: The normarization factor f vs. Pb thickness for π.

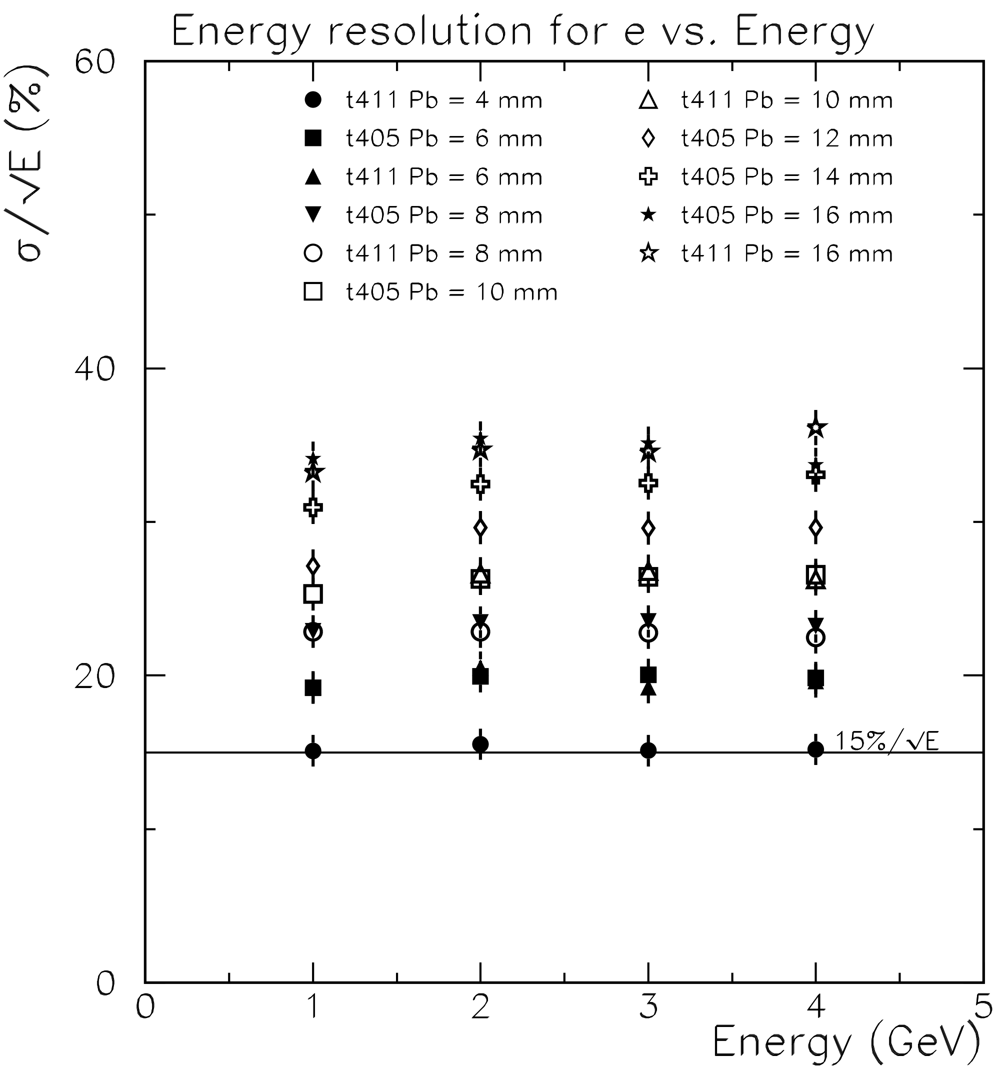

Figure 5.19: Energy resolution vs. energy for electrons. Solid line in the figure is the requirement of the energy resolution for the JLC EM calorimeter.

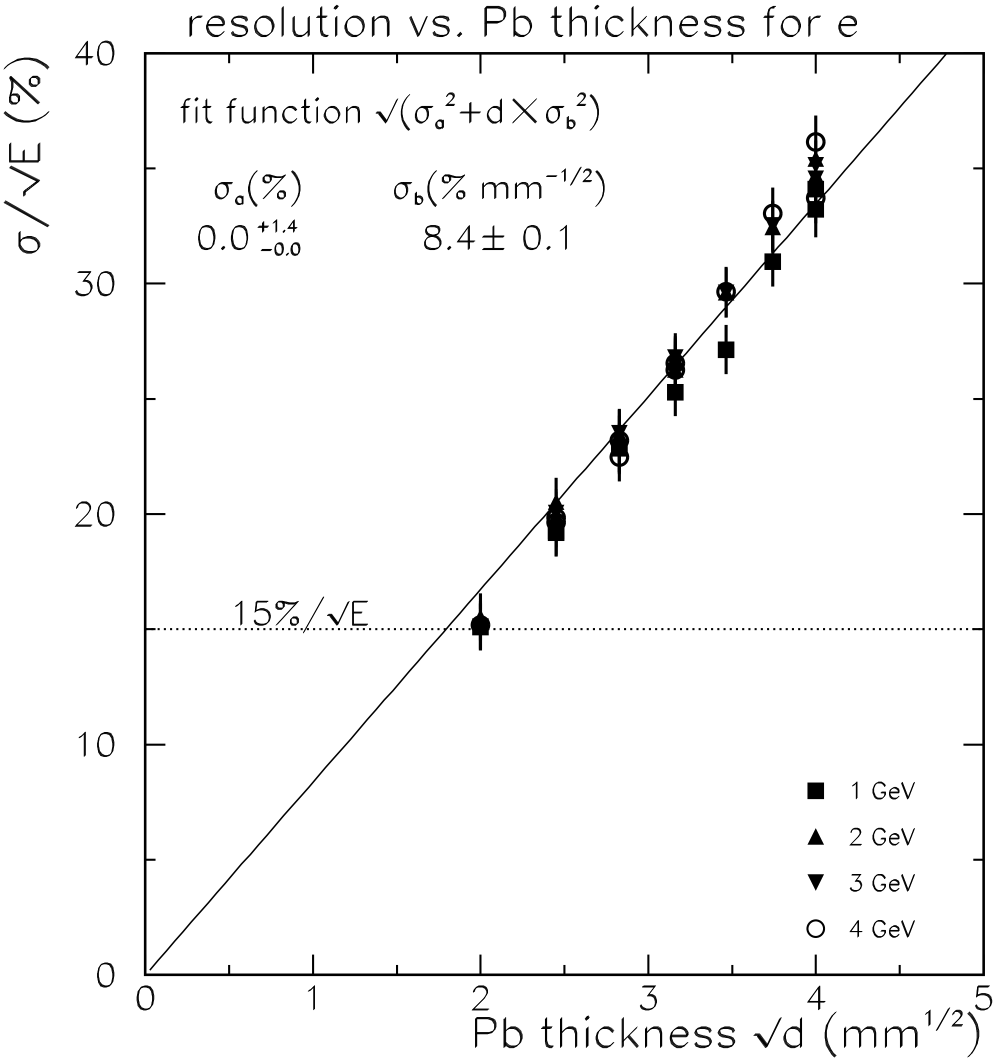

Figure 5.20: Energy resolution vs. Pb thickness for electrons. Solid curve shown in the figure is fitting results to Eq. (5.2). Dotted line in the figure is the requirement of the energy resolution for the JLC EM calorimeter.

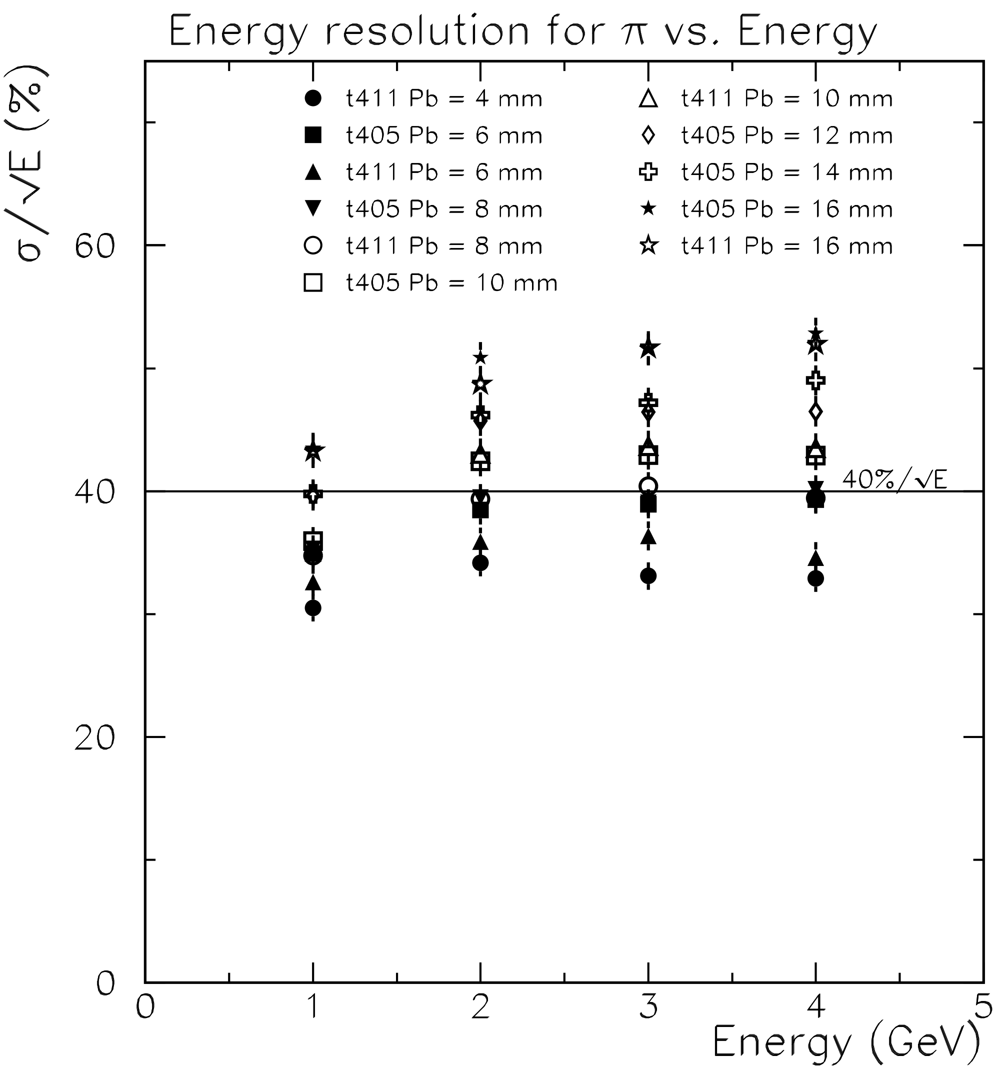

Figure 5.21: Energy resolution vs. energy for π's. Solid line in the figure is the requirement of the energy resolution for the JLC hadron calorimeter.

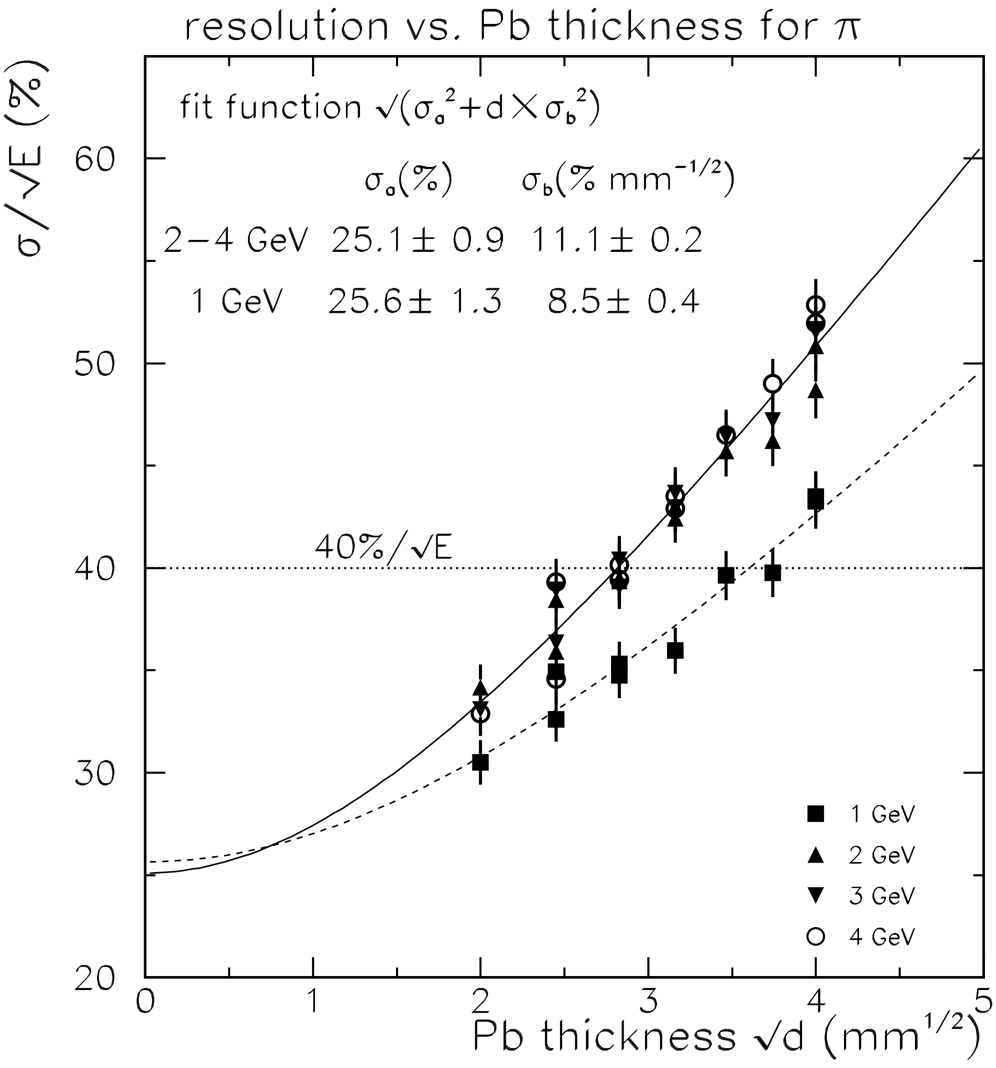

Figure 5.22: Energy resolution vs. Pb thickness for π's Solid and dashed curves shown in the figure are fitting results to Eq. (5.2) except for 1 GeV and 1 GeV. Dotted line in the figure is the requirement of the energy resolution for the JLC hadron calorimeter.

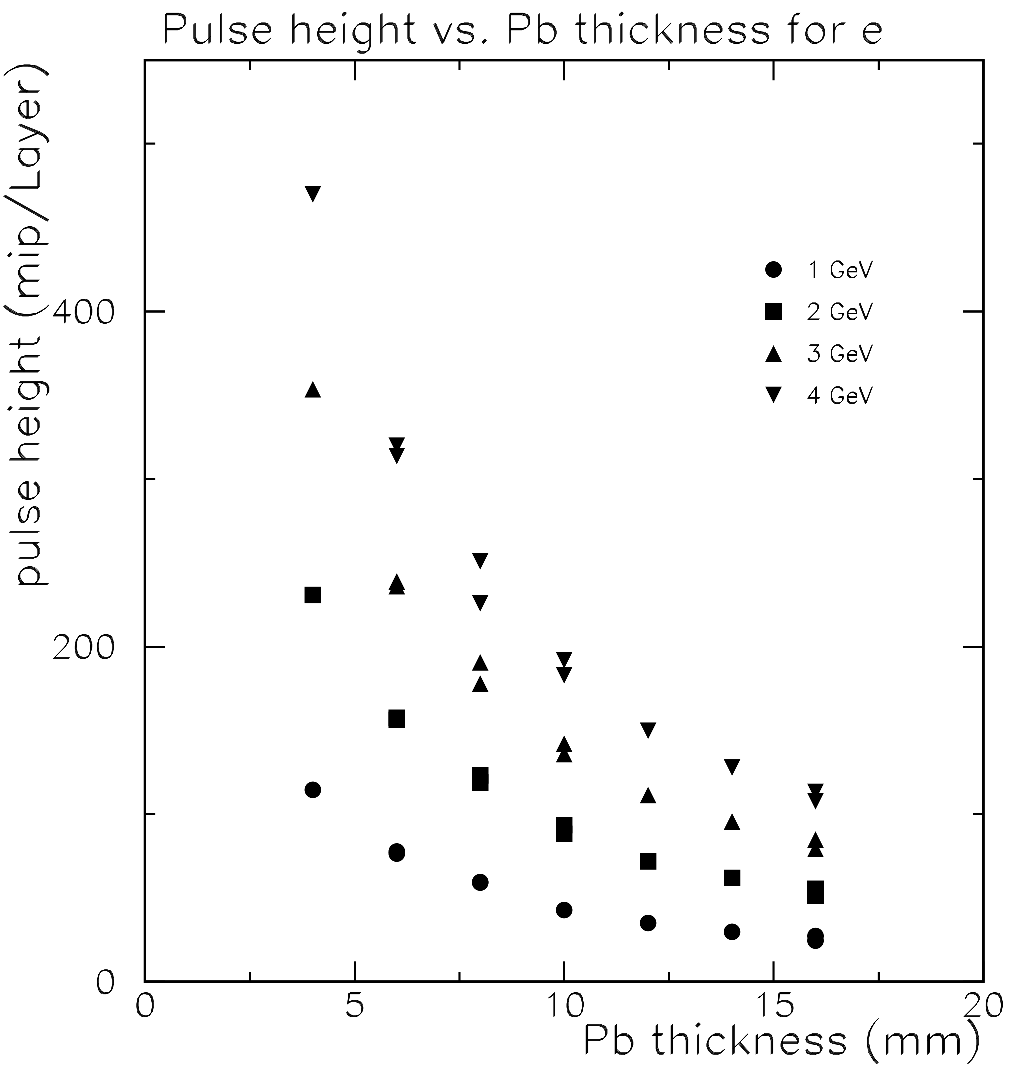

Figure 5.23: Pulse height vs. Pb thickness for electrons.

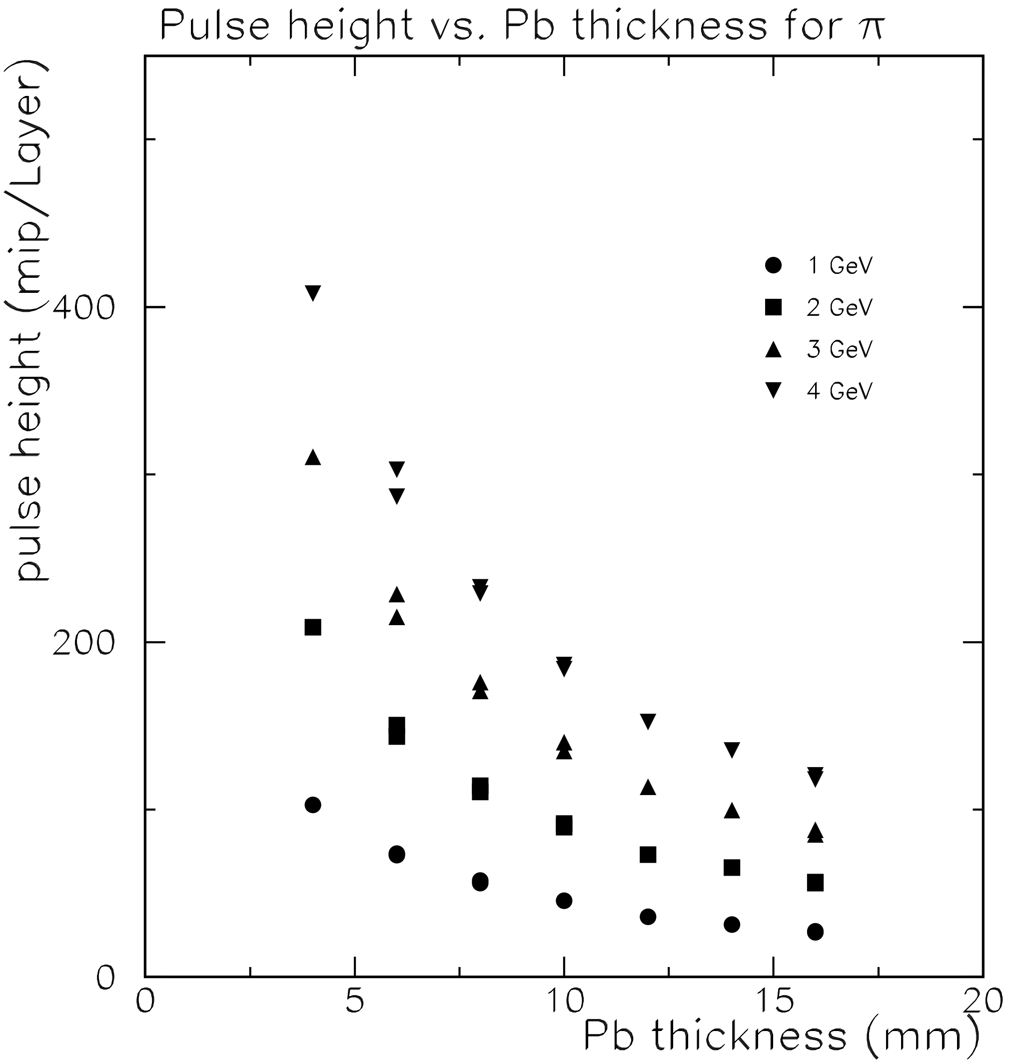

Figure 5.24: Pulse height vs. Pb thickness for π's

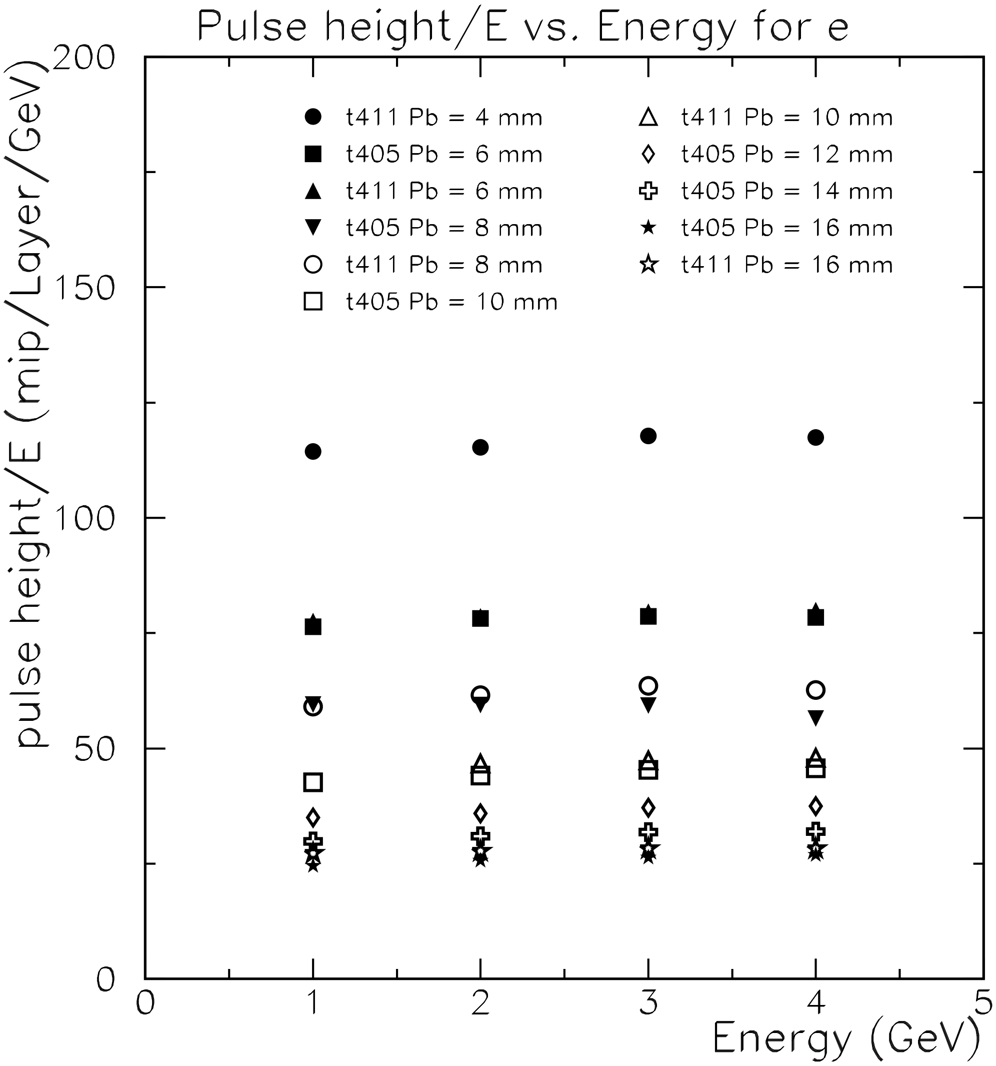

Figure 5.25: Pulse height vs. energy for electrons.

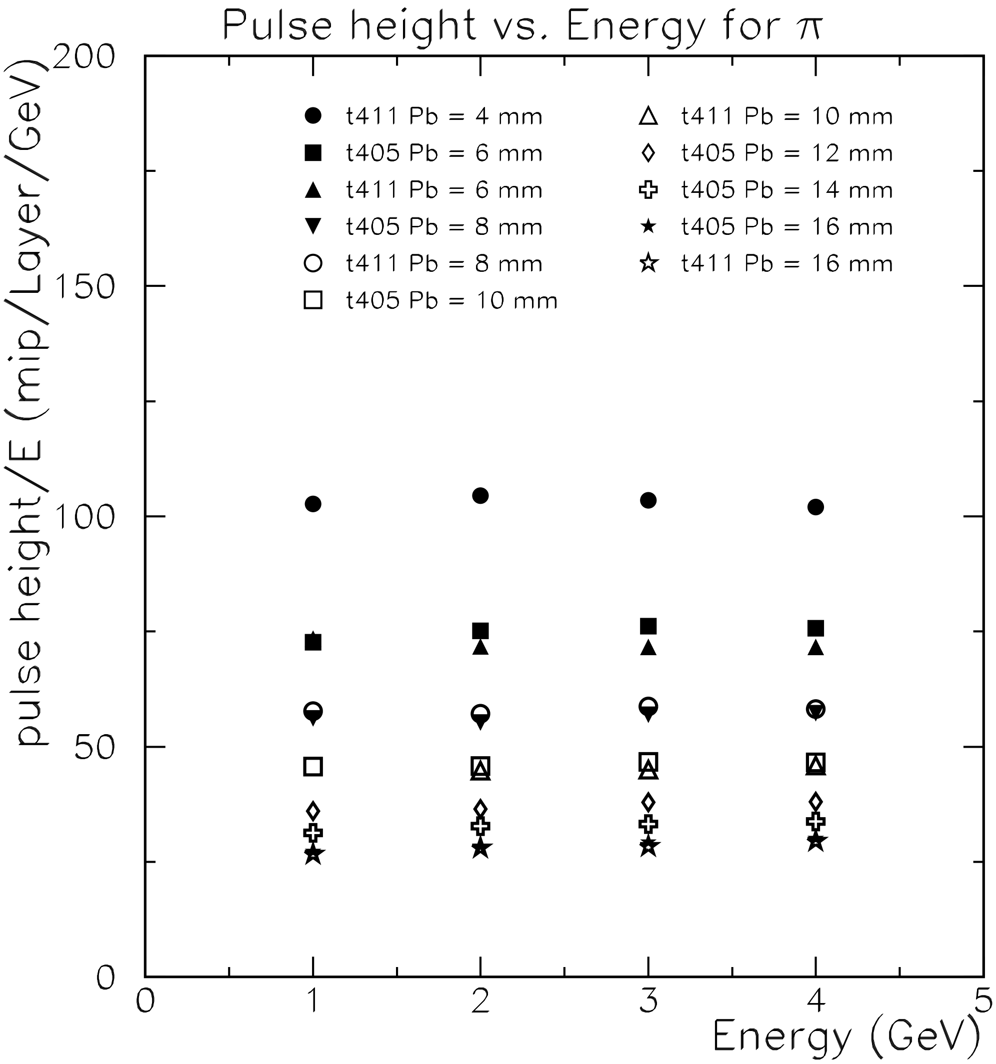

Figure 5.26: Pulse height vs. energy for π's.

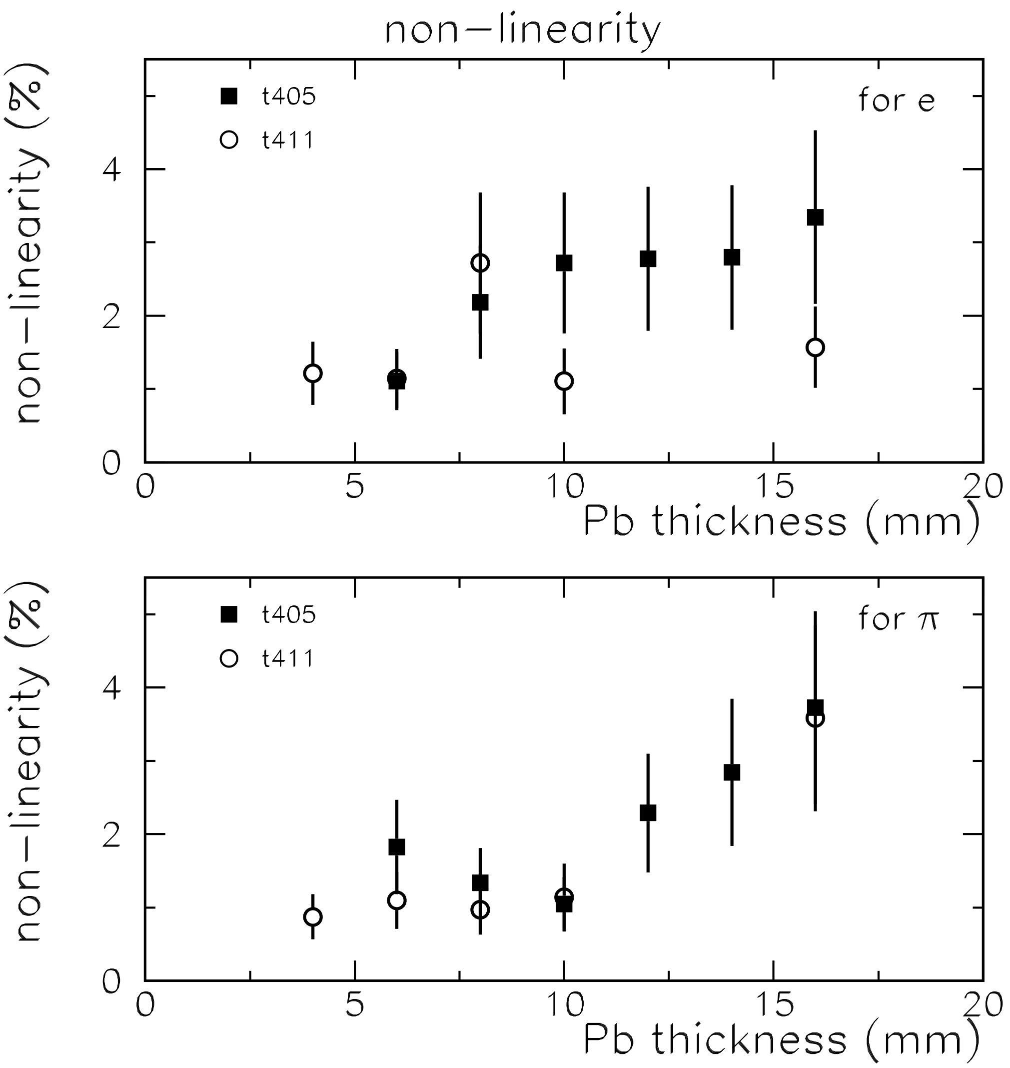

Figure 5.27: Non-linearity vs. calorimeter configurations for electrons(top) and for π's(above).

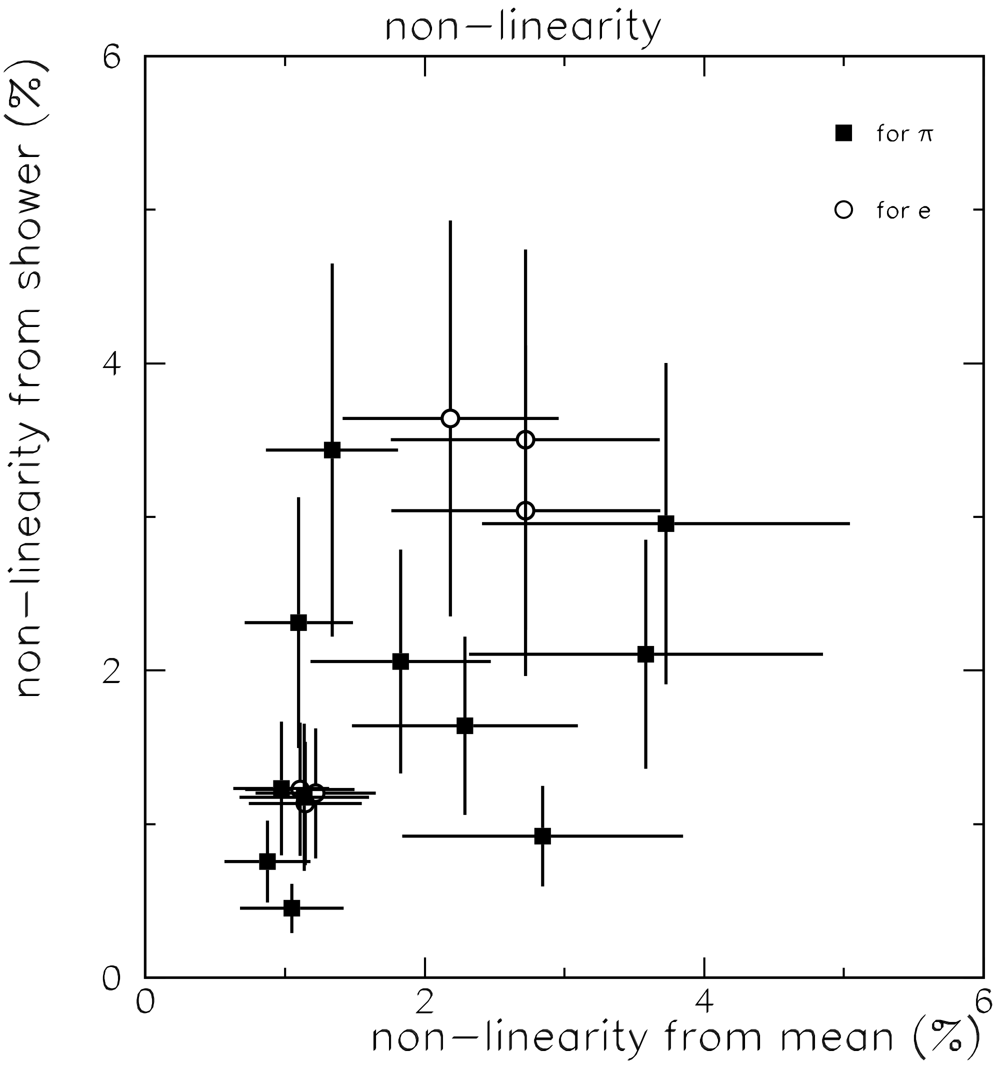

Figure 5.28: The non-linearity estimated from f vs. the non-linearity estimated from pulse height.

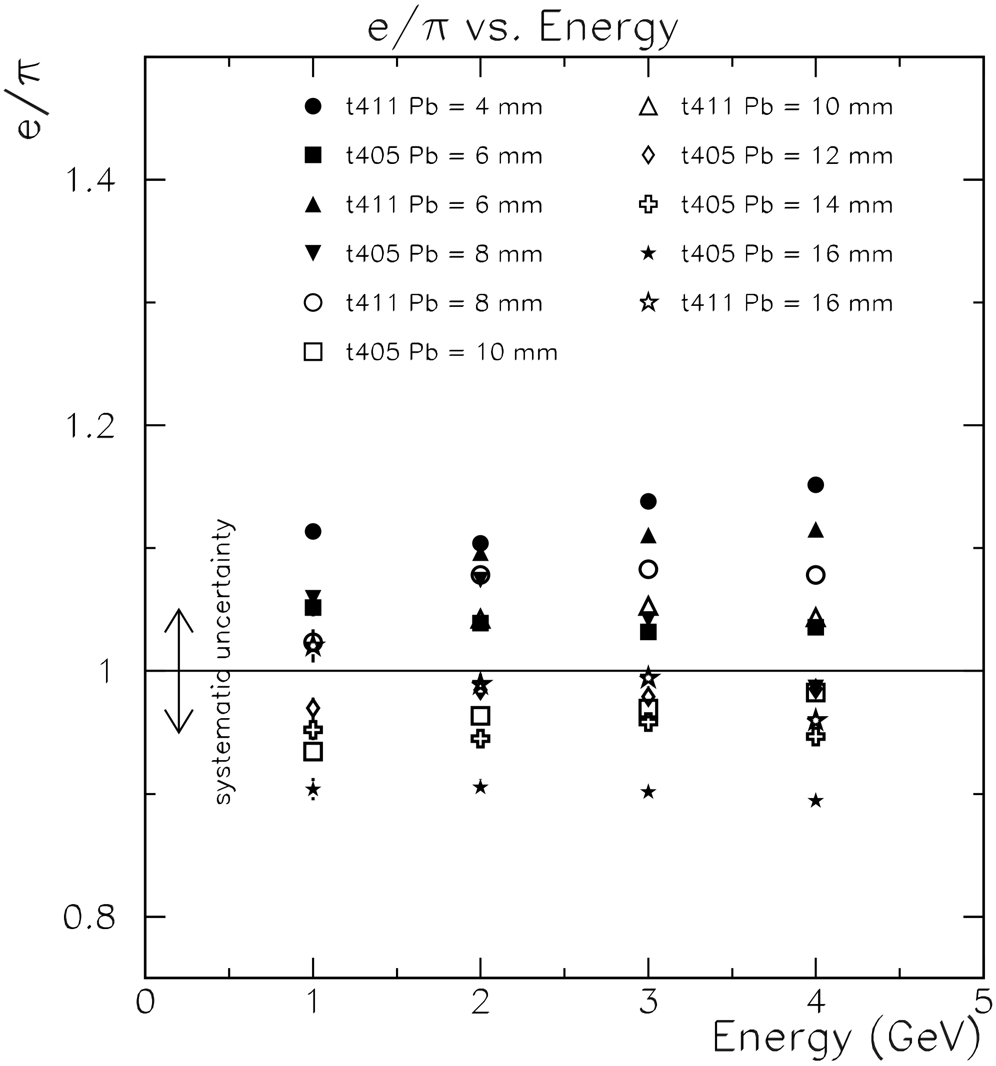

Figure 5.29: e/π vs. Pb thickness for each configurations.

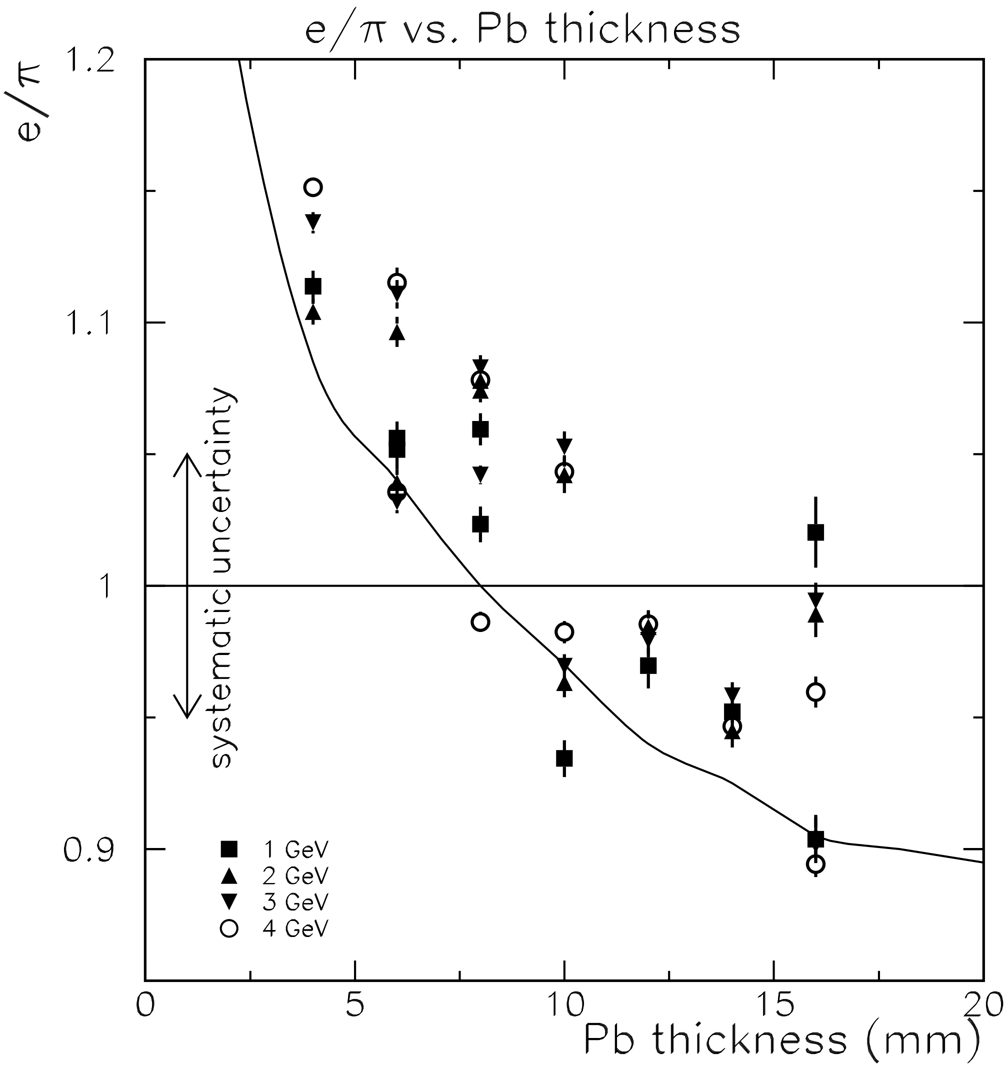

Figure 5.30: The e/π ratio vs. Pb thickness for each configurations. Solid curve in the figure is the e/h ratio as a function of the volume ratio [2].

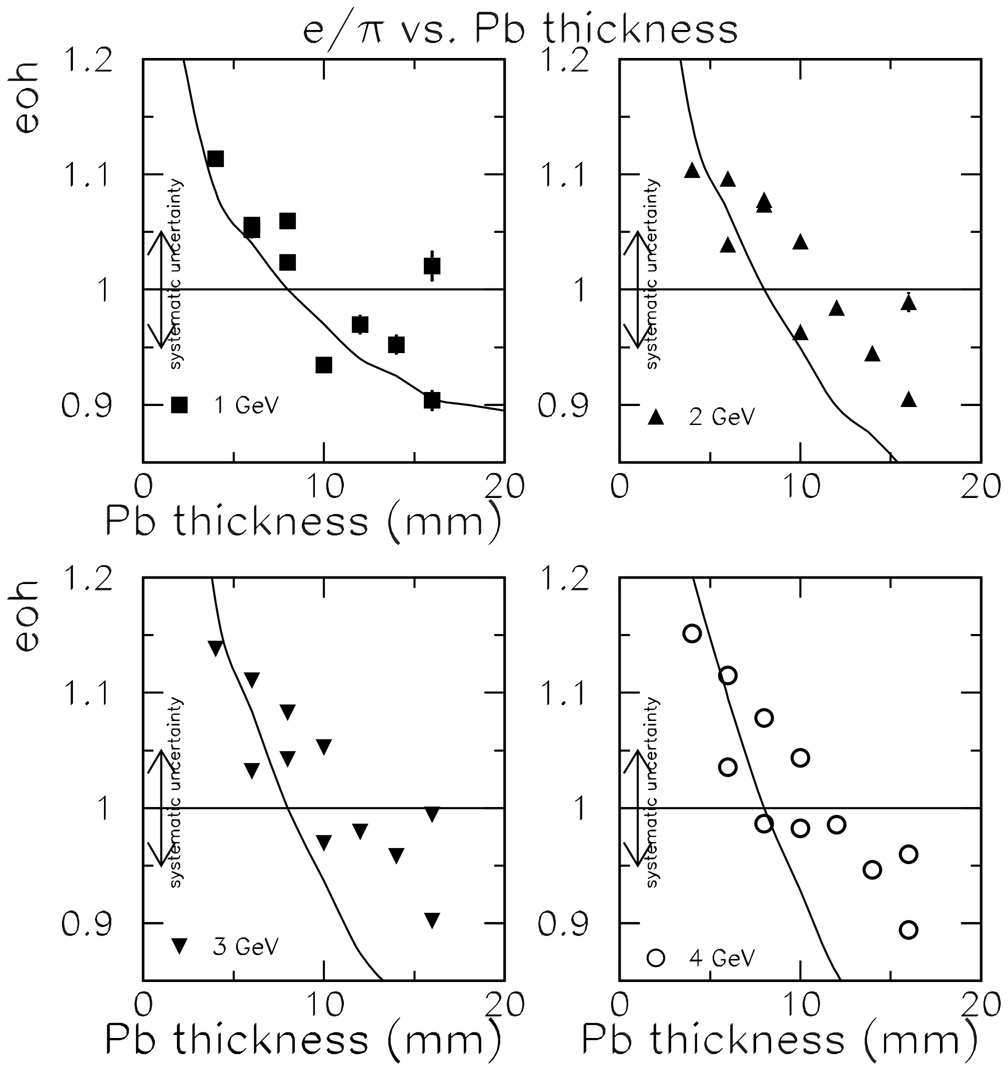

Figure 5.31: The e/π ratio vs. Pb thickness for each configurations. Solid curve in the figure is the e/π ratio as a function of the volume ratio calculated with Eq. (2.10) [2].

Chapter 6

Summary

We have measured the optical properties of the tile/fiber systems and constructed a calorimeter prototype using the tile/fiber systems as active volume layers. We estimated the energy resolution and the e/π ratio of the our calorimeter prototype with the configuration that the thickness of the lead plate is 8 mm using a GEANT simulation and the measured properties of the tile/fiber systems.

The average light yield and its rms variation in a tile (except the points near the fibers) are 1.67 $\pm$ 0.24 photoelectrons/mip and 6 $\pm$ 2% in the direction across the fibers. The rms variation in the direction parallel to the fibers is 3%. The energy resolution of the calorimeter prototype is estimated to energy degrade by 6 $\pm$ 3% for 4 GeV electrons and 6 $\pm$ 5% for 4 GeV pions with this finite non-uniformity. The total systematic uncertainty for e/π due to lateral non-uniformity and longitudinal(layer-by-layer : 15%) non-uniformity is 5 $\pm$ 2%.

We performed the beam tests of the calorimeter prototype and measured the energy resolution and the e/π ratio. The energy resolutions for electrons in the lead-plastic scintilletor calorimeter is measured as a function of lead plate thickness d (mm),

$$\frac{\sigma}{\mathrm{E}} = \sqrt{\frac{(0.0^{+1.4}_{-0.0}\%)^2 + (7.5 \pm 0.1\%)^2 \times d}{\mathrm{E}}},$$

where E is the beam energy. To achieve the required energy resolution for the JLC EM calorimeter, Pb thickness should be less equal 4 mm.

The energy resolution for π's in the lead-plastic scintillator calorimeter is measured as a function of lead plate thickness d. The function is

$$\frac{\sigma}{\mathrm{E}} = \sqrt{\frac{(25.1 \pm 0.9\%)^2 + (10.3 \pm 0.2\%)^2 \times d}{\mathrm{E}}} \quad \text{excluding 1 GeV},$$

and it is

$$\frac{\sigma}{\mathrm{E}} = \sqrt{\frac{(25.6 \pm 1.3\%)^2 + (7.6 \pm 0.4\%)^2 \times d}{\mathrm{E}}} \quad \text{for 1 GeV}.$$

To achieve the required energy resolution for the JLC hadron calorimeter, Pb absorber thickness should be less equal 8 mm.

The e/π ratio decreases with the absorber thickness d and is one around $d = 8\sim10$ mm. The compensation was found to be acheived with the ratio of the scintillator thickness to the Pb thickness of $4\sim5$ as expected.

Bibliography

[1] JLC Group, KEK Report **92-16**, (1992).

[2] R. Wigmans, CERN-PPE **91-205**, (1991).

[3] C. W. Fabjan and R. Wigmans, Rep. Prog. Phys. **52**, (1989).

[4] E. Bernardi *et al.*, Nucl. Instrum. Methods Phys. Res., Sect. **A 262**, 229 (1987).

[5] T. Akesson *et al.*, Nucl. Instrum. Methods Phys. Res., Sect. **A 262**, 243 (1987).

[6] D. Acosta *et al.*, Nucl. Instrum. Methods Phys. Res., Sect. **A 308**, 481 (1991).

[7] K. Ishii, I. Nakamura *et.al.*, Nucl. Instrum. Methods Phys. Res., Sect. **A 385**, 215 (1997).

[8] ZEUS Collab., The ZEUS Detector, Status Report, DESY (1993).

[9] The CDF II Collaboration, The CDF II Detector Technical Design Report FELMILAB-Pub-**96/390-E** (1996).

[10] ATLAS Collaboration, Technical Proposal CERN/LHCC **94-43**, (1991).

[11] CMS Collaboration, Technical Proposal CERN/LHCC **94-38**, (1994).

[12] T. Asakawa *et al.*, Nucl. Instrum. Methods Phys. Res., Sect. **A 340**, 458 (1994). S. Aota *et al.*, Nucl. Instrum. Methods Phys. Res., Sect. **A 352**, 557 (1995).

[13] S. Kim (CDF Collaboration), Nucl. Instrum. Methods Phys. Res., Sect. **A 360**, 206 (1995).

[14] S. Aota *et al.*, Nucl. Instrum. Methods Phys. Res., Sect. **A 357**, 71 (1995).

[15] K. Hara *et al.*, Nucl. Instrum. Methods Phys. Res., Sect. **A 348**, 139 (1994).

[16] Y. Fujii, Proceedings of the Third Workshop on Japan Linear Collider (JLC), KEK Proseedings **92-13**, 355 (1992).

[17] Y. Fujii, Proceedings of the Fourth Workshop on Japan Linear Collider (JLC), KEK Proseedings **94-1**, 55 (1993).

[18] Y. Fujii, Proceedings of the fifth Workshop on Japan Linear Collider (JLC), KEK Proseedings **95-11**, 123 (1995).

[19] T. Suzuki, Proceedings of the sixth Workshop on Japan Linear Collider (JLC), KEK Proseedings **97-2**, 143 (1997).

[20] Particle Data Group, Phys. Rev. **D54** 132 (1996).

[21] Particle Data Group, Phys. Rev. **D54** 132 (1996).

[22] Particle Data Group, Phys. Rev. **D54** 142 (1996).

[23] R. Brun *et al.*, “GEANT3” CERN DD/EE/84-1.